Journal of Computational Physics 518 (2024) 113322

Contents lists available at ScienceDirect

Journal of Computational Physics

journal homepage: www.elsevier.com/locate/jcp

A first-order hyperbolic Arbitrary Lagrangian Eulerian conservation formulation for nonlinear solid dynamics in irreversible processes

Thomas B.J. Di Giusto [a,d], Chun Hean Lee [b,*], Antonio J. Gil [a,*], Javier Bonet [c,d,**], Clare Wood [a], Matteo Giacomini [c,e]

[a] *Zienkiewicz Institute for Modelling, Data and AI, Faculty of Science and Engineering, Swansea University, Bay Campus, SA1 8EN, United Kingdom*
[b] *Glasgow Computational Engineering Centre (GCEC), James Watt School of Engineering, University of Glasgow, United Kingdom*
[c] *Centre Internacional de Mètodes Numèrics en Enginyeria (CIMNE), Barcelona, Spain*
[d] *Departament de Enginyeria Civil i Ambiental (DECA), Universitat Politècnica de Catalunya, Barcelona, Spain*
[e] *Laboratori de Càlcul Numèric (LaCàN), ETS de Ingeniería de Caminos, Canales y Puertos, Universitat Politècnica de Catalunya, Barcelona, Spain*

ARTICLE INFO

Keywords:
Solid dynamics
Conservation laws
Arbitrary Lagrangian Eulerian
Ballistic
Large strain
Godunov-type finite volume method

ABSTRACT

The paper introduces a computational framework that makes use of a novel Arbitrary Lagrangian Eulerian (ALE) conservation law formulation for nonlinear solid dynamics. In addition to the standard mass conservation law and the linear momentum conservation law, the framework extends its application to consider more general irreversible processes such as thermo-elasticity and thermo-visco-plasticity. This requires the incorporation of the first law of thermodynamics, expressed in terms of the entropy density, as an additional conservation law. To disassociate material particles from mesh positions, the framework introduces an additional reference configuration, extending beyond conventional material and spatial descriptions. The determination of the mesh motion involves the solution of a conservation-type momentum equation, ensuring optimal mesh movement and contributing to maintaining a high-quality mesh and improving solution accuracy, particularly in regions undergoing large plastic flows. To maintain equal convergence orders for all variables (strains/stresses, velocities/displacements and temperature/entropy), the standard deformation gradient tensor (measured from material to spatial configuration) is evaluated through a multiplicative decomposition into two auxiliary deformation gradient tensors. Both are obtained through additional first-order conservation laws. The exploitation of the hyperbolic nature of the underlying system, together with accurate wave speed bounds, ensures the stability of explicit time integrators. For spatial discretisation, a vertex-centred Godunov-type Finite Volume method is employed and suitably adapted to the formulation at hand. To guarantee stability from both the continuum and the semi-discretisation standpoints, a carefully designed numerical interface flux is presented. Lyapunov stability analysis is carried out by evaluating the time variation of the *Ballistic* energy of the system, aiming to ensure the positive production of numerical entropy. Finally, a variety of three dimensional benchmark problems are presented to illustrate the robustness and applicability of the framework.

---

* Corresponding authors.
** Corresponding author at: Centre Internacional de Mètodes Numèrics en Enginyeria (CIMNE), Barcelona, Spain.
E-mail addresses: chunhean.lee@glasgow.ac.uk (C.H. Lee), a.j.gil@swansea.ac.uk (A.J. Gil), jbonet@cimne.upc.edu (J. Bonet).

https://doi.org/10.1016/j.jcp.2024.113322
Received 16 March 2024; Received in revised form 21 June 2024; Accepted 27 July 2024

1. Introduction

The standard formulations in computational solid dynamics, such as purely Total or Updated Lagrangian descriptions, align the computational mesh (nodes) with the underlying material discretisation (particles) [1–5]. This concurrent motion simplifies the continuum formulation and the discrete solution of the algorithm, enabling direct tracking of evolving boundaries and interfaces. However, in scenarios involving large deformations, Lagrangian formulations may encounter mesh distortion, requiring the use of complex remeshing strategies [6] for accurate and reliable results. Motivated by these challenges, Arbitrary Lagrangian Eulerian (ALE) based techniques have emerged to combine the advantages of both Lagrangian and Eulerian approaches. The ALE formulation introduces a referential (fixed) domain for motion description, separate from the material and spatial domains [7–15]. The computational mesh neither attaches to the material (Lagrangian description) nor remains fixed in space (Eulerian description), but it partially follows the material points to reduce element distortion. The ALE formulation shows promise in addressing challenges in large strain solid dynamics, including hyper-velocity dynamic impact/contact [16] and crack propagation.

The ALE formulation for solid dynamics [17,18], initially designed for highly deformable hypoelastic-plastic and hyperelastic-plastic processes, involves different approaches for stress computation. In hypoelastic-plastic models [16,19], stresses are described in a rate form, linking an objective stress rate with the rate of deformation tensor. Conversely, hyperelastic–plastic models [20–22] compute stresses from the deformation gradient using a strain energy potential combined with a suitable plastic projection algorithm. Such procedure eliminates the need for stress rate equations. Regardless of the approach, a crucial aspect is the ALE convective term in the stress update equation, reflecting the relative motion between the computational mesh and material particles. To handle the convective term, one possible option is to split the ALE solution process into material and convection stages (remap stage [23–25]). The material stage neglects convection, making it identical to the standard Lagrangian updating process. Subsequently, stresses and plastic internal variables are convected in the remap stage to account for relative mesh motion. On a different note, Yamada et al. [22] proposed an ALE finite element method for hyperelastic model that circumvents the need to consider convective terms. This is achieved by establishing suitable mappings between the referential, material and spatial domains. The deformation gradient tensor, describing the fibre map between material and spatial domains (and thus, stresses), can be computed from the referential domain using the chain rule. However, even in this case, if large plastic strains are considered, the convection of internal plastic variables describing the plastic response is still needed [21].

Recently, a computational framework [26], formulated in terms of ALE first-order conservation laws, was introduced for hyperelasticity. Specifically, both the mass conservation equation and linear momentum conservation equation were re-formulated and solved within the fixed referential domain. To ensure equal order of convergence for velocities/displacements and strains/stresses, the update of the physical deformation gradient tensor (measured from material to spatial domains) was achieved through its multiplicative decomposition into two auxiliary deformation gradient tensors. These two deformations were computed using additional geometric conservation laws. A notable feature of this ALE formulation lies in its capability to degenerate into three different mixed-based sets of conservation equations: Total Lagrangian formulation [27–30], Eulerian formulation [31] and Updated Reference Lagrangian formulation [32]. To illustrate the proof-of-concept of the formulation, numerical examples were carried out by utilising a hyperelastic model with prescribed mesh motion for the sake of simplicity.

To assess the potential benefits of the developed ALE formulation, the current paper broadens its range of application to consider more general irreversible processes, such as thermal effects [33] and rate- and/or path-dependent constitutive models [34–37]. A simple mesh motion strategy inspired by the work of [21] will be explored. This will be achieved by solving a conservation-type momentum equation for the mesh motion. In this work, the proposed ALE formulation will be exclusively examined for a single material. However, when dealing with high-speed multi-material flows, it becomes crucial to develop more complex adaptive algorithms that can dynamically move the mesh to adapt to the evolving interface shape. One possible option is to relax constraints on mesh topology and allow reconnection, typically known as “ReALE - a reconnection-based ALE method” [12,23]. This would be the next step of our work.

A critical aspect requiring special attention is the stability of the proposed ALE formulation, from both the continuum and numerical standpoints. Concerning the former, the use of an internal energy potential satisfying rank-one convexity guarantees the existence of plane travelling waves within the solid and the propagation of strong discontinuities at physical shock speeds. Regarding spatial discretisation, a Godunov-type upwinding approach is pursued where appropriate numerical stabilisation is introduced, ensuring local production of numerical entropy. The latter is demonstrated by monitoring the time variation of the *Ballistic* of the coupled system, also known as Lyapunov stability analysis.

The paper is structured as follows. Section 2 provides a review of the fundamental kinematic relationships utilised in an Arbitrary Lagrangian Eulerian description. In Section 3, we begin by summarising the ALE conservation laws necessary for isothermal process, as previously presented in Reference [26]. We then extend this discussion to incorporate the ALE-type first law of thermodynamics expressed in terms of entropy density, accounting for thermal influences. Section 4 addresses finite strain plasticity, incorporating the nonlinear strain-rate and thermal-dependent Johnson-Cook hardening law. The ALE evolution equations for the plastic state variables are presented. Section 5 details the mesh smoothing procedure used in this work to address excessive mesh distortions, particularly in regions of large plastic flows. In Section 6, we explore the time variation of the *Ballistic* energy of the system, used as a preamble to formulate non-negative entropy-producing numerical dissipation. Section 7 discusses the vertex-based finite volume spatial discretisation procedure. Special attention is paid to deriving entropy-stable conservative and consistent numerical fluxes. Additionally, we discuss the explicit time integrator used to advance the semi-discrete equations in time. For implementation purposes, Section 8 summarises the algorithmic flowchart of the resulting computational framework. Section 9 presents a series of numerical examples to illustrate the capabilities of the proposed ALE numerical framework. Finally, Section 10 provides a summary of key

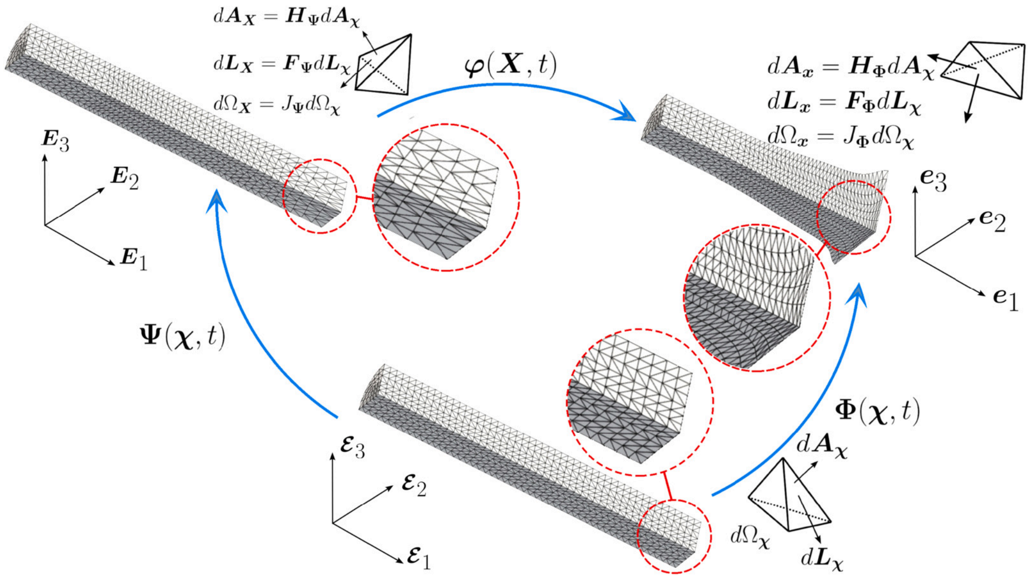

Fig. 1. ALE kinematic description.

conclusions and outlines lines of prospective research. Appendix A summarises the transformation of conservation laws from the Total Lagrangian to the ALE description, providing details on integral form, local differential equations and jump conditions.

2. ALE kinematical description

Consider the motion of a continuum initially defined by a domain $\Omega_{\boldsymbol{X}} \subset \mathbb{R}^3$ in its material configuration. This configuration is enclosed by a boundary, denoted as $\partial\Omega_{\boldsymbol{X}}$, with a corresponding unit outward normal vector $\boldsymbol{N}_{\boldsymbol{X}} = \sum_{I=1}^{3} N_{\boldsymbol{X}}^{I} \boldsymbol{E}_I$. As the continuum undergoes motion, it deforms into a spatial configuration defined by a domain $\Omega_{\boldsymbol{x}} \subset \mathbb{R}^3$ with a boundary $\partial\Omega_{\boldsymbol{x}}$ and a unit outward normal vector $\boldsymbol{n}_{\boldsymbol{x}} = \sum_{i=1}^{3} n_{\boldsymbol{x}}^{i} \boldsymbol{e}_i$.

In an Arbitrary Lagrangian Eulerian (ALE) description, in addition to the usual material and spatial configurations described above, a third “referential” configuration is introduced. This configuration is occupied by the domain $\Omega_{\chi} \subset \mathbb{R}^3$ with a boundary $\partial\Omega_{\chi}$ and an outward unit normal $\boldsymbol{N}_{\chi} = \sum_{I=1}^{3} N_{\chi}^{I} \boldsymbol{\mathcal{E}}_I$. Consequently, two new mappings are introduced, linking the referential coordinate $\chi \in \Omega_{\chi}$ to: (1) the material configuration $\boldsymbol{X} \in \Omega_{\boldsymbol{X}}$ via $\boldsymbol{X} = \boldsymbol{\Psi}(\chi, t)$ and (2) the spatial configuration $\boldsymbol{x} \in \Omega_{\boldsymbol{x}}$ via $\boldsymbol{x} = \boldsymbol{\Phi}(\chi, t)$. Fig. 1 illustrates these domains and the one-to-one transformation relating the three configurations. We refer to $\boldsymbol{\Phi}(\chi, t)$ as the spatial motion (the mapping from the referential domain to the spatial domain) and to $\boldsymbol{\Psi}(\chi, t)$ as the material motion (the mapping from the referential domain to the material domain). With these definitions, the *physical* motion $\boldsymbol{\varphi}(\boldsymbol{X}, t)$ at a fixed time is parametrised as $\boldsymbol{\varphi} = \boldsymbol{\Phi} \circ \boldsymbol{\Psi}^{-1}$, emphasising that the three mappings $\{\boldsymbol{\varphi}, \boldsymbol{\Psi}, \boldsymbol{\Phi}\}$ are not independent. Utilising the relation $\boldsymbol{\varphi}(\boldsymbol{X}, t) = \boldsymbol{\Phi}(\boldsymbol{\Psi}^{-1}(\chi, t), t)$, the multiplicative decomposition of the *physical* deformation gradient tensor is expressed as

$$\boldsymbol{F} = \boldsymbol{F}_{\boldsymbol{\Phi}} \boldsymbol{F}_{\boldsymbol{\Psi}}^{-1}, \tag{1}$$

with the respective deformation gradient tensors defined as

$$\boldsymbol{F}(\boldsymbol{X}, t) = \frac{\partial \boldsymbol{\varphi}(\boldsymbol{X}, t)}{\partial \boldsymbol{X}}; \qquad \boldsymbol{F}_{\boldsymbol{\Psi}}(\chi, t) = \frac{\partial \boldsymbol{\Psi}(\chi, t)}{\partial \chi}; \qquad \boldsymbol{F}_{\boldsymbol{\Phi}}(\chi, t) = \frac{\partial \boldsymbol{\Phi}(\chi, t)}{\partial \chi}. \tag{2}$$

It is possible to introduce the corresponding cofactors and Jacobians as follows

$$\boldsymbol{H} = \frac{1}{2} \boldsymbol{F} \times \boldsymbol{F}; \qquad \boldsymbol{H}_{\boldsymbol{\Psi}} = \frac{1}{2} \boldsymbol{F}_{\boldsymbol{\Psi}} \times \boldsymbol{F}_{\boldsymbol{\Psi}}; \qquad \boldsymbol{H}_{\boldsymbol{\Phi}} = \frac{1}{2} \boldsymbol{F}_{\boldsymbol{\Phi}} \times \boldsymbol{F}_{\boldsymbol{\Phi}}, \tag{3}$$

and

$$J = \frac{1}{3} \boldsymbol{H} : \boldsymbol{F}; \qquad J_{\boldsymbol{\Psi}} = \frac{1}{3} \boldsymbol{H}_{\boldsymbol{\Psi}} : \boldsymbol{F}_{\boldsymbol{\Psi}}; \qquad J_{\boldsymbol{\Phi}} = \frac{1}{3} \boldsymbol{H}_{\boldsymbol{\Phi}} : \boldsymbol{F}_{\boldsymbol{\Phi}}. \tag{4}$$

Here, $\times$ denotes the tensor-cross-product between second order tensor as discussed in References [38,39]. Equations (2), (3) and (4) establish line, area and volume mappings between differential elements of the different configurations as follows

$$d\boldsymbol{L}_{\boldsymbol{X}} = \boldsymbol{F}_{\boldsymbol{\Psi}} d\boldsymbol{L}_{\chi}; \qquad d\boldsymbol{l}_{\boldsymbol{x}} = \boldsymbol{F}_{\boldsymbol{\Phi}} d\boldsymbol{L}_{\chi}; \qquad d\boldsymbol{l}_{\boldsymbol{x}} = \boldsymbol{F} d\boldsymbol{L}_{\boldsymbol{X}}; \tag{5a}$$

$$d\boldsymbol{A}_{\boldsymbol{X}} = \boldsymbol{H}_{\boldsymbol{\Psi}} d\boldsymbol{A}_{\chi}; \qquad d\boldsymbol{a}_{\boldsymbol{x}} = \boldsymbol{H}_{\boldsymbol{\Phi}} d\boldsymbol{A}_{\chi}; \qquad d\boldsymbol{a}_{\boldsymbol{x}} = \boldsymbol{H} d\boldsymbol{A}_{\boldsymbol{X}}; \tag{5b}$$

$$d\Omega_X = J_{\boldsymbol{\Psi}} d\Omega_\chi; \qquad d\Omega_x = J_{\boldsymbol{\Phi}} d\Omega_\chi; \qquad d\Omega_x = J\, d\Omega_X. \tag{5c}$$

Next, let us consider the time rates of the above mappings $\{\boldsymbol{\varphi}, \boldsymbol{\Psi}, \boldsymbol{\Phi}\}$ depicted in Fig. 1. For instance, the (*physical*) velocity $\boldsymbol{v}$ of a particle $\boldsymbol{X}$, the (spatial) velocity $\hat{\boldsymbol{v}}$ associated with the spatial map, and the (material) velocity $\boldsymbol{W}$ associated with the material map are given by

$$\boldsymbol{v} = \frac{\partial \boldsymbol{\varphi}(\boldsymbol{X}, t)}{\partial t} = \left.\frac{\partial}{\partial t}\right|_{\boldsymbol{X}} \boldsymbol{\varphi}; \qquad \hat{\boldsymbol{v}} = \frac{\partial \boldsymbol{\Phi}(\chi, t)}{\partial t} = \left.\frac{\partial}{\partial t}\right|_{\chi} \boldsymbol{\Phi}; \qquad \boldsymbol{W} = \frac{\partial \boldsymbol{\Psi}(\chi, t)}{\partial t} = \left.\frac{\partial}{\partial t}\right|_{\chi} \boldsymbol{\Psi}, \tag{6}$$

with $\Big|_{\square}$ meaning "holding the coordinate $\square$ fixed". Recalling $\boldsymbol{F}$ (2) together with the definitions of the various velocities (6), the relation between $\boldsymbol{v}$, $\hat{\boldsymbol{v}}$ and $\boldsymbol{W}$ now follows as

$$\hat{\boldsymbol{v}} = \frac{\partial \boldsymbol{\Phi}(\chi, t)}{\partial t} = \frac{\partial \boldsymbol{\varphi}(\boldsymbol{\Psi}(\chi, t), t)}{\partial t} = \frac{\partial \boldsymbol{\varphi}(\boldsymbol{X}, t)}{\partial t} + \frac{\partial \boldsymbol{\varphi}(\boldsymbol{X}, t)}{\partial \boldsymbol{X}} \frac{\partial \boldsymbol{\Psi}(\chi, t)}{\partial t} = \boldsymbol{v} + \boldsymbol{F}\boldsymbol{W}. \tag{7}$$

3. ALE first-order conservation laws for solids

3.1. First-order conservation laws for non-thermal processes

In the preceding work by the authors [26], the motion of a deformable solid for non-thermal processes is described by a system of first-order conservation laws formulated within an ALE framework as follows

$$\left.\frac{\partial}{\partial t}\right|_{\chi} \boldsymbol{p}_\chi - \mathrm{DIV}_\chi \left[\left(\boldsymbol{P} + \boldsymbol{p}_X \otimes \boldsymbol{W} \right) \boldsymbol{H}_{\boldsymbol{\Psi}} \right] = \boldsymbol{f}_\chi; \tag{8a}$$

$$\left.\frac{\partial}{\partial t}\right|_{\chi} \boldsymbol{F}_{\boldsymbol{\Phi}} - \mathrm{DIV}_\chi \left(\hat{\boldsymbol{v}} \otimes \boldsymbol{I} \right) = \boldsymbol{0}; \tag{8b}$$

$$\left.\frac{\partial}{\partial t}\right|_{\chi} \boldsymbol{F}_{\boldsymbol{\Psi}} - \mathrm{DIV}_\chi \left(\boldsymbol{W} \otimes \boldsymbol{I} \right) = \boldsymbol{0}; \tag{8c}$$

$$\left.\frac{\partial}{\partial t}\right|_{\chi} J_{\boldsymbol{\Psi}} - \mathrm{DIV}_\chi \left(\boldsymbol{H}_{\boldsymbol{\Psi}}^T \boldsymbol{W} \right) = 0. \tag{8d}$$

Here, $\boldsymbol{p}_\chi = \rho_\chi \boldsymbol{v}$ is the linear momentum per unit of reference volume, $\boldsymbol{p}_X = \rho_R \boldsymbol{v}$ is the linear momentum per unit of material volume, $\rho_\chi = J_{\boldsymbol{\Psi}} \rho_R$ is the density of the reference configuration, ρ_R is the material density, $\boldsymbol{f}_\chi$ is the body force per unit of reference volume and $\boldsymbol{P}$ is the first Piola Kirchhoff stress tensor. The operator DIV_χ represents the divergence operator carried out at the reference configuration.

Expressions (8a) and (8d) represent the fundamental physical conservation equations formulated in the ALE framework. The former corresponds to the standard linear momentum conservation equation, while the latter denotes the mass continuity equation with the assumption of uniform material density. Furthermore, expressions (8b) and (8c) constitute an additional set of geometric conservation equations, aiming to accurately monitor the deformation of a fibre from the reference configuration to both spatial and material configurations, respectively. An advantage of solving these additional geometric conservation equations lies in the fact that the evaluation of the fibre mappings $\{\boldsymbol{F}_{\boldsymbol{\Phi}}, \boldsymbol{F}_{\boldsymbol{\Psi}}\}$ is no longer dependent on both the spatial and material geometries. This aspect has demonstrated its benefits in both Total Lagrangian [40] and Updated Lagrangian approaches [32,41], especially when dealing with scenarios involving large deformations.

As the system of conservation laws presented above contains more equations than necessary, compatibility relationships, also known as involutions [42], become essential. Specifically,

$$\mathrm{CURL}_\chi \boldsymbol{F}_{\boldsymbol{\Phi}} = \boldsymbol{0}; \qquad \mathrm{CURL}_\chi \boldsymbol{F}_{\boldsymbol{\Psi}} = \boldsymbol{0}. \tag{9}$$

In the presence of shocks or discontinuities across a surface, it is worth noticing that the evaluation of the divergence operator DIV_χ (8) becomes unfeasible. Consequently, the applicability of the system (8) in its differential form is no longer valid. In such instances, we must then resort to the utilisation of appropriate Rankine-Hugoniot jump conditions across a discontinuous surface. This surface is defined by a reference unit normal vector $\boldsymbol{N}_\chi$ and propagates with a speed U_χ in the reference space [26]. These conditions can be expressed as

$$U_\chi [\![\boldsymbol{p}_\chi]\!] = -[\![\left(\boldsymbol{P} + \boldsymbol{p}_X \otimes \boldsymbol{W} \right) \boldsymbol{H}_{\boldsymbol{\Psi}}]\!] \boldsymbol{N}_\chi; \tag{10a}$$

$$U_\chi [\![\boldsymbol{F}_{\boldsymbol{\Phi}}]\!] = -[\![\hat{\boldsymbol{v}}]\!] \otimes \boldsymbol{N}_\chi; \tag{10b}$$

$$U_\chi [\![\boldsymbol{F}_{\boldsymbol{\Psi}}]\!] = -[\![\boldsymbol{W}]\!] \otimes \boldsymbol{N}_\chi; \tag{10c}$$

$$U_\chi [\![J_{\boldsymbol{\Psi}}]\!] = -[\![\boldsymbol{H}_{\boldsymbol{\Psi}}^T \boldsymbol{W}]\!] \cdot \boldsymbol{N}_\chi. \tag{10d}$$

Here, $[\![\bullet]\!] = [\bullet]^+ - [\bullet]^-$ denotes the difference between the right state $(+)$ and left state $(-)$ of a discontinuous surface.

3.2. Extension to consider thermal influence

The above system (8) extends to more general constitutive models incorporating thermal effects, such as thermo-elasticity [30] and thermo-visco-plasticity [37]. These irreversible processes require an additional conservation law and variable to describe the total balance of energy in the system (known as the first law of thermodynamics). Referring to Reference [30,37] and employing the ALE transformation rule (A.2), the first law of thermodynamics in terms of entropy density η_χ per unit referential volume can be expressed as

$$\left.\frac{\partial}{\partial t}\right|_{\chi} \eta_\chi - \mathrm{DIV}_\chi \left(\eta_{\boldsymbol{X}} \boldsymbol{H}_{\boldsymbol{\Psi}}^T \boldsymbol{W} - \frac{\boldsymbol{Q}_\chi}{\theta} \right) = \frac{J_{\boldsymbol{\Psi}}}{\theta} \left(s_{\boldsymbol{X}} + \dot{D}_{\mathrm{Phy}} \right) - \frac{1}{\theta^2} \left(\boldsymbol{\nabla}_\chi \theta \right) \cdot \boldsymbol{Q}_\chi, \tag{11}$$

where $\eta_\chi = J_{\boldsymbol{\Psi}} \eta_{\boldsymbol{X}}$ and $\eta_{\boldsymbol{X}}$ is the entropy density per unit of material volume. Note that the expression (11) for entropy assumes smooth solutions and remains a representation of the first law. In this equation (11), $\theta > 0$ denotes the absolute temperature, $\boldsymbol{Q}_\chi$ represents the heat flux defined in the reference domain, $s_{\boldsymbol{X}}$ is the heat source term in the material configuration and the term $\eta_{\boldsymbol{X}} \boldsymbol{H}_{\boldsymbol{\Psi}}^T \boldsymbol{W}$ arises due to ALE convective effects. The right-hand side terms comprise the entropy sources per unit reference volume, with $\dot{D}_{\mathrm{Phy}}$ representing the material time rate of physical dissipation introduced by constitutive models, such as plasticity. This is mathematically defined as

$$\dot{D}_{\mathrm{Phy}} = - \frac{\partial \mathcal{E}(\boldsymbol{F}, \eta_{\boldsymbol{X}}, \boldsymbol{\alpha})}{\partial \boldsymbol{\alpha}} : \left.\frac{\partial}{\partial t}\right|_{\boldsymbol{X}} \boldsymbol{\alpha}. \tag{12}$$

This term is zero in the case of a reversible elastic model [26]. Here, $\mathcal{E}(\boldsymbol{F}, \eta_{\boldsymbol{X}}, \boldsymbol{\alpha})$ is the internal energy per unit material volume and $\boldsymbol{\alpha}$ represents a set of internal state variables measured with respect to the material configuration. The shorthand notation $[\dot{\bullet}]$ denotes holding the material coordinate $\boldsymbol{X}$ fixed, that is $[\dot{\bullet}] = \left.\frac{\partial}{\partial t}\right|_{\boldsymbol{X}} [\bullet]$. This notation will be used throughout the entire manuscript.

Concerning the heat flux vector $\boldsymbol{Q}_\chi$, we adopt Fourier's law for isotropic materials in a reference configuration

$$\boldsymbol{Q}_\chi = -\boldsymbol{K}_{\boldsymbol{\Phi}} \boldsymbol{\nabla}_\chi \theta; \qquad \boldsymbol{K}_{\boldsymbol{\Phi}} = h J_{\boldsymbol{\Phi}}^{-1} \boldsymbol{H}_{\boldsymbol{\Phi}}^T \boldsymbol{H}_{\boldsymbol{\Phi}}, \tag{13}$$

where h represents the non-negative thermal conductivity coefficient calibrated in the spatial configuration.

Remark 1 Utilising the Calorimetry relationships relating internal energy density $\mathcal{E}$, entropy density $\eta_{\boldsymbol{X}}$ and temperature θ, and taking into account the relation $\theta = \frac{\partial \mathcal{E}}{\partial \eta_{\boldsymbol{X}}}$, we obtain a simple expression linking temperature and entropy [43]

$$\Theta(\boldsymbol{F}, \eta_{\boldsymbol{X}}) = \theta_R \exp\left(\frac{\eta_{\boldsymbol{X}} - \tilde{\eta}_{\boldsymbol{X}}(J)}{c_v} \right) = \theta(\boldsymbol{X}, t), \tag{14}$$

where θ_R denotes the reference temperature, $\tilde{\eta}_{\boldsymbol{X}}(J)$ represents an entropy function as a function of the Jacobian and evaluated at the reference temperature θ_R, and $c_v = \rho_{\boldsymbol{X}} C_V$, with C_V and c_v denoting the specific heat per unit mass and per unit material volume, respectively, which have been assumed to be constant. The notation Θ and θ are used interchangeably to denote the same temperature with different functional dependencies.

3.3. Combined system of first-order conservation laws for solid dynamics

By combining the physical conservation equations, including the conservation of linear momentum (8a), conservation of mass (8d) and conservation of total energy (11), together with the supplementary geometric conservation equations, namely (8b) and (8c), a set of first-order conservation equations can be succinctly expressed as an ALE hyperbolic system (with respect to the referential domain) as

$$\left.\frac{\partial}{\partial t}\right|_{\chi} \boldsymbol{\mathcal{U}}_\chi + \sum_{I=1}^{3} \frac{\partial \boldsymbol{\mathcal{F}}_\chi^I}{\partial \chi_I} = \boldsymbol{\mathcal{S}}_\chi, \tag{15}$$

with vector of conserved variables $\boldsymbol{\mathcal{U}}_\chi$, flux vector $\boldsymbol{\mathcal{F}}_\chi^I$ and source term $\boldsymbol{\mathcal{S}}_\chi$ described by

$$\boldsymbol{\mathcal{U}}_\chi = \begin{bmatrix} \boldsymbol{p}_\chi \\ \boldsymbol{F}_{\boldsymbol{\Phi}} \\ \boldsymbol{F}_{\boldsymbol{\Psi}} \\ J_{\boldsymbol{\Psi}} \\ \eta_\chi \end{bmatrix}; \quad \boldsymbol{\mathcal{F}}_\chi^I = - \begin{bmatrix} \boldsymbol{P}_\chi \boldsymbol{\mathcal{E}}_I \\ \hat{\boldsymbol{v}} \otimes \boldsymbol{\mathcal{E}}_I \\ \boldsymbol{W} \otimes \boldsymbol{\mathcal{E}}_I \\ \boldsymbol{H}_{\boldsymbol{\Psi}} : \left(\boldsymbol{W} \otimes \boldsymbol{\mathcal{E}}_I \right) \\ \left(\eta_{\boldsymbol{X}} \boldsymbol{H}_{\boldsymbol{\Psi}}^T \boldsymbol{W} - \frac{\boldsymbol{Q}_\chi}{\theta} \right) \cdot \boldsymbol{\mathcal{E}}_I \end{bmatrix}; \quad \boldsymbol{\mathcal{S}}_\chi = \begin{bmatrix} \boldsymbol{f}_\chi \\ \boldsymbol{0} \\ \boldsymbol{0} \\ 0 \\ \frac{J_{\boldsymbol{\Psi}}}{\theta} \left(s_{\boldsymbol{X}} + \dot{D}_{\mathrm{Phy}} \right) - \frac{1}{\theta^2} \boldsymbol{Q}_\chi \cdot \left(\boldsymbol{\nabla}_\chi \theta \right) \end{bmatrix}, \tag{16}$$

where, for the sake of compactness, we define

$$\boldsymbol{P}_\chi = \left(\boldsymbol{P} + \boldsymbol{p}_{\boldsymbol{X}} \otimes \boldsymbol{W} \right) \boldsymbol{H}_{\boldsymbol{\Psi}}. \tag{17}$$

Table 1
Physical variables associated with generic conservation variables, fluxes and source terms.

Total Lagrangian	Unknowns	Fluxes	Source terms
Mass	ρ_X	0	0
Linear momentum	$\boldsymbol{p}_X$	$-\boldsymbol{P}$	$\boldsymbol{f}_X$
Deformation gradient	$\boldsymbol{F}$	$-\boldsymbol{v}\otimes\boldsymbol{I}$	$\boldsymbol{0}$
Entropy	η_X	$\frac{\boldsymbol{Q}_X}{\theta}$	$\frac{1}{\theta}s_X - \frac{1}{\theta^2}\boldsymbol{Q}_X\cdot\boldsymbol{\nabla}_X\theta$
Updated Reference Lagrangian			
Mass	$J_{\boldsymbol{\Psi}}\rho_X$	0	0
Linear momentum	$J_{\boldsymbol{\Psi}}\boldsymbol{p}_X$	$-\boldsymbol{P}\boldsymbol{H}_{\boldsymbol{\Psi}}$	$J_{\boldsymbol{\Psi}}\boldsymbol{f}_X$
Deformation gradient	$\boldsymbol{F}_{\boldsymbol{\Phi}}$	$-\boldsymbol{v}\otimes\boldsymbol{I}$	$\boldsymbol{0}$
Entropy	$J_{\boldsymbol{\Psi}}\eta_X$	$\frac{\boldsymbol{Q}_\chi}{\theta}$	$\frac{J_{\boldsymbol{\Psi}}}{\theta}s_X - \frac{1}{\theta^2}\boldsymbol{Q}_\chi\cdot\boldsymbol{\nabla}_\chi\theta$
Eulerian			
Mass	ρ_x	$\rho_x\boldsymbol{v}$	0
Linear momentum	$\boldsymbol{p}_x$	$-\left(\boldsymbol{\sigma}-\boldsymbol{p}_x\otimes\boldsymbol{v}\right)$	$J^{-1}\boldsymbol{f}_X$
Deformation gradient	$\boldsymbol{F}^{-1}$	$\left(\boldsymbol{F}^{-1}\boldsymbol{v}\right)\otimes\boldsymbol{I}$	$\boldsymbol{0}$
Entropy	η_x	$\frac{\boldsymbol{q}}{\theta}+\eta_x\boldsymbol{v}$	$\frac{J^{-1}}{\theta}s_X - \frac{1}{\theta^2}\boldsymbol{q}\cdot\boldsymbol{\nabla}_x\theta$

Notice that the variables per unit of spatial volume are $\rho_x = J^{-1}\rho_X$, $\boldsymbol{p}_x = J^{-1}\boldsymbol{p}_X$, $\eta_x = J^{-1}\eta_X$ and the Cauchy stress tensor $\boldsymbol{\sigma} = \boldsymbol{P}\boldsymbol{H}^{-1}$.

In addition to the initial and boundary (essential and natural) conditions necessary for the complete definition of the initial boundary value problem, the closure of the system (15) requires the incorporation of a suitable constitutive law that must satisfy various physical criteria, including thermodynamic consistency (as verified through the Coleman–Noll procedure [44,45]) and adherence to the principle of objectivity [4]. In the context of thermo-elasticity, achieving this involves introducing an appropriate internal energy potential, denoted as $\mathcal{E}(\boldsymbol{F},\eta_X)$. This potential ensures that stress $\boldsymbol{P}$, deformation gradient tensor $\boldsymbol{F}$ and entropy η_X are related through the expression $\boldsymbol{P} = \frac{\partial\mathcal{E}(\boldsymbol{F},\eta_X)}{\partial\boldsymbol{F}}$. Furthermore, to ensure stability, it is crucial that the internal energy potential $\mathcal{E}$ exhibits rank-one convexity (or ellipticity) in the sense of the Legendre-Hadamard condition [46,47]. Extension to consider path-dependent constitutive models will be explored in Section 4.

Interestingly, through the imposition of suitable kinematic conditions [26], the ALE system (15) can degenerate into three alternative systems of first-order conservation equations. As shown in Table 1, these formulations include the well-established Total Lagrangian formulation [27,29,30,37,41,48–60], the Eulerian formulation and the recently proposed Updated Reference Lagrangian formulation [32,37], which incorporates the concept of incremental kinematics. Thus, the ALE system (15) emerges as an elegant generalisation of various existing continuum conservation laws descriptions.

Remark 2 The assessment of the hyperbolicity of the underlying system (15) is crucial to ensure the existence of real wave speeds for the entire range of deformation states. As detailed in References [26,30], the requirement of (rank-one) convex internal energy functional is sufficient to ensure hyperbolicity for a given material mesh motion, resulting in (1) the existence of plane travelling waves within the solid (through the use of flux derivatives) and (2) the propagation of strong discontinuities at physical shock speeds (through the use of the jump in fluxes). The relationship between the referential wave speed U_χ and the material wave speed U_X is summarised below for completeness

$$U_\chi = \frac{\Lambda_{\boldsymbol{H}_{\boldsymbol{\Psi}}}}{J_{\boldsymbol{\Psi}}}\left(U_X - \boldsymbol{W}\cdot\boldsymbol{N}_X\right); \qquad \Lambda_{\boldsymbol{H}_{\boldsymbol{\Psi}}}\boldsymbol{N}_X = \boldsymbol{H}_{\boldsymbol{\Psi}}\boldsymbol{N}_\chi. \tag{18}$$

We refer the reader to Reference [26] for a detailed explanation.

---

4. Extension to finite strain plasticity

In various engineering applications, the presence of irreversible (or permanent) strain, coupled with thermal- and strain rate-dependent plastic deformation, is a common phenomenon. To describe this behaviour, we employ a von Mises plasticity model utilising the nonlinear Johnson-Cook hardening law [37], which is summarised in this section for completeness. In the context of large strains, it is customary to multiplicatively decompose the deformation gradient tensor $\boldsymbol{F}$ into an elastic component $\boldsymbol{F}_e$ and a permanent deformation component $\boldsymbol{F}_p$ as [4,61]

$$\boldsymbol{F} = \boldsymbol{F}_e\boldsymbol{F}_p. \tag{19}$$

This decomposition leads to the evaluation of the elastic left Cauchy-Green tensor $\boldsymbol{b}_e$, expressed in terms of the overall deformation gradient $\boldsymbol{F}$ and an inelastic right Cauchy-Green tensor $\boldsymbol{C}_p$, described by

$$\boldsymbol{b}_e = \boldsymbol{F}_e\boldsymbol{F}_e^T = \boldsymbol{F}\boldsymbol{C}_p^{-1}\boldsymbol{F}^T. \tag{20}$$

With this at hand, the state variable described in (12) corresponds to the inverse of the plastic right Cauchy-Green tensor, denoted as $\boldsymbol{\alpha} = \boldsymbol{C}_p^{-1}$.

To establish a physically meaningful flow rule, it is useful to apply the concept of work conjugacy. In the context of elasto-plasticity, the material time derivative of plastic dissipation $\dot{\mathcal{D}}_{\text{Phy}}$ (per unit material volume) is given in terms of Kirchhoff stress $\boldsymbol{\tau}$ and the plastic rate of deformation $\boldsymbol{l}_p$ as [4]

$$\dot{\mathcal{D}}_{\text{Phy}} = \boldsymbol{\tau} : \boldsymbol{l}_p; \qquad \boldsymbol{l}_p = -\frac{1}{2}\frac{d\boldsymbol{b}_e}{dt}\bigg|_{\boldsymbol{F}=\text{const}} \boldsymbol{b}_e^{-1} = -\frac{1}{2}\boldsymbol{F}\left(\frac{\partial}{\partial t}\bigg|_{\boldsymbol{X}} \boldsymbol{C}_p^{-1}\right)\boldsymbol{C}_p\boldsymbol{F}^{-1}, \tag{21}$$

where $\frac{d\boldsymbol{b}_e}{dt}\big|_{\boldsymbol{F}=\text{const}}$ describes the material time derivative of $\boldsymbol{b}_e$ assuming $\boldsymbol{F}$ constant. For an in-depth understanding, we recommend referring to Reference [4]. To adhere to the principle of maximum plastic dissipation, it is crucial to establish a correlation between the plastic rate of deformation and the flow rule, ensuring the material efficiently dissipates energy due to plastic deformation.

In this study, we employ the von Mises based Johnson-Cook hardening law, characterised by a yield function f dependent on the deviatoric Kirchhoff stress $\boldsymbol{\tau}'$ and a yield stress $\bar{\tau}_y$. The yield stress is a function of the equivalent plastic strain $\bar{\varepsilon}_p$, its plastic strain rate $\dot{\bar{\varepsilon}}_p$ (involving the material time derivative) and temperature θ, expressed as

$$f\left(\boldsymbol{\tau}', \bar{\varepsilon}_p, \dot{\bar{\varepsilon}}_p, \theta\right) = \underbrace{\sqrt{\frac{3}{2}(\boldsymbol{\tau}' : \boldsymbol{\tau}')}}_{\bar{\tau}} - \bar{\tau}_y\left(\bar{\varepsilon}_p, \dot{\bar{\varepsilon}}_p, \theta\right) \leq 0. \tag{22}$$

Here, $\bar{\tau}$ represents the generalised scalar von Mises equivalent stress. The Johnson-Cook hardening law is described by

$$\bar{\tau}_y\left(\bar{\varepsilon}_p, \dot{\bar{\varepsilon}}_p, \theta\right) = \left(\bar{\tau}_y^0 + H\bar{\varepsilon}_p^N\right)\left[1 + C\ln\left(\frac{\dot{\bar{\varepsilon}}_p}{\dot{\varepsilon}_0}\right)\right]\left[1 - (g(\theta))^M\right], \tag{23}$$

where $g(\theta)$ is defined as

$$g(\theta) = \begin{cases} 0 & \text{if } \theta < \theta_{\text{transition}} \\ \frac{\theta - \theta_{\text{transition}}}{\theta_{\text{melting}} - \theta_R} & \text{if } \theta_{\text{transition}} \leq \theta \leq \theta_{\text{melting}} \\ 1 & \theta > \theta_{\text{melting}}. \end{cases} \tag{24}$$

In the above expression, θ denotes the current temperature, θ_{melting} is the melting temperature of the material and $\theta_{\text{transition}}$ is the temperature at or below which there is temperature dependence of the yield stress. Additionally, $\bar{\tau}_y^0$ represents the initial yield stress and $\dot{\varepsilon}_0$ is the reference strain rate calibrated based on the material. The remaining material constants include the material hardening parameter H, hardening exponent N, strain-rate coefficient C and temperature exposure M. Notably, when $\theta > \theta_{\text{melting}}$, the material is assumed to melt and behave like a fluid, offering no shear resistance since $\bar{\tau}_y = 0$. Interestingly, the rate-independent linear hardening law can be simply recovered by imposing the values $N = 1$, $C = 0$ and $\theta_{\text{transition}} \approx \infty$ (which in turn implies $g(\theta) = 0$).

The associated flow rule, where the direction of the plastic strain rate coincides with the gradient of the yield function $f\left(\boldsymbol{\tau}', \bar{\varepsilon}_p, \dot{\bar{\varepsilon}}_p, \theta\right)$, can be defined as follows

$$\boldsymbol{l}_p = -\frac{1}{2}\frac{d\boldsymbol{b}_e}{dt}\bigg|_{\boldsymbol{F}=\text{const}} \boldsymbol{b}_e^{-1} = \dot{\gamma}\frac{\partial f\left(\boldsymbol{\tau}', \bar{\varepsilon}_p, \dot{\bar{\varepsilon}}_p, \theta\right)}{\partial \boldsymbol{\tau}}, \tag{25}$$

where $\dot{\gamma}$, a proportionality factor, is referred to as the consistency parameter (or plastic multiplier). It is expressed as a rate to maintain dimensional consistency with the plastic rate of deformation $\boldsymbol{l}_p$. By comparing and rearranging expressions (21) and (25), the material time derivative of the inelastic right Cauchy-Green tensor after some simple algebra can be obtained

$$\frac{\partial}{\partial t}\bigg|_{\boldsymbol{X}} \boldsymbol{C}_p^{-1} = -2\dot{\gamma}\boldsymbol{F}^{-1}\left(\frac{\partial f\left(\boldsymbol{\tau}', \bar{\varepsilon}_p, \dot{\bar{\varepsilon}}_p, \theta\right)}{\partial \boldsymbol{\tau}}\boldsymbol{b}_e\right)\boldsymbol{F}^{-T}. \tag{26}$$

The next step involves establishing the relationship between the consistency parameter $\dot{\gamma}$ and the evolution of the internal hardening variable $\bar{\varepsilon}_p$. This can be achieved through a traditional work-hardening approach. By recalling the von-Mises equivalent stress $\bar{\tau}$ from (22), the material time rate of $\bar{\varepsilon}_p$ is defined to be the work conjugate to $\bar{\tau}$

$$\bar{\tau}\frac{\partial}{\partial t}\bigg|_{\boldsymbol{X}} \bar{\varepsilon}_p = \dot{\mathcal{D}}_{\text{Phy}} = \boldsymbol{\tau} : \left(\dot{\gamma}\frac{\partial f(\boldsymbol{\tau}', \bar{\varepsilon}_p, \dot{\bar{\varepsilon}}_p, \theta)}{\partial \boldsymbol{\tau}}\right) = \boldsymbol{\tau} : \dot{\gamma}\frac{\boldsymbol{\tau}'}{\sqrt{\frac{2}{3}(\boldsymbol{\tau}' : \boldsymbol{\tau}')}} = \bar{\tau}\dot{\gamma}. \tag{27}$$

Comparing the first term and the last term yields

$$\frac{\partial}{\partial t}\bigg|_{\boldsymbol{X}} \bar{\varepsilon}_p = \dot{\gamma}. \tag{28}$$

Finally, using the local transformation rule described in (A.4), the ALE evolution equations for $\boldsymbol{C}_p^{-1}$ and $\bar{\varepsilon}_p$ are given by

$$J_{\boldsymbol{\Psi}} \left.\frac{\partial}{\partial t}\right|_{\chi} \boldsymbol{C}_p^{-1} - \left(\boldsymbol{\nabla}_{\chi} \boldsymbol{C}_p^{-1}\right)\left(\boldsymbol{H}_{\boldsymbol{\Psi}}^T \boldsymbol{W}\right) = -2 J_{\boldsymbol{\Psi}} \dot{\gamma} \boldsymbol{F}^{-1} \left(\frac{\partial f\left(\boldsymbol{\tau}', \bar{\varepsilon}_p, \dot{\bar{\varepsilon}}_p, \theta\right)}{\partial \boldsymbol{\tau}} \boldsymbol{b}_e\right) \boldsymbol{F}^{-T}; \tag{29a}$$

$$J_{\boldsymbol{\Psi}} \left.\frac{\partial}{\partial t}\right|_{\chi} \bar{\varepsilon}_p - \left(\boldsymbol{\nabla}_{\chi} \bar{\varepsilon}_p\right) \cdot \left(\boldsymbol{H}_{\boldsymbol{\Psi}}^T \boldsymbol{W}\right) = J_{\boldsymbol{\Psi}} \dot{\gamma}, \tag{29b}$$

respectively.

Remark 3 It is possible to derive the appropriate conjugate variable for the material time rate of the inverse of the inelastic right Cauchy-Green tensor. To begin, recall the relation

$$\dot{\mathcal{D}}_{\text{Phy}} = -\frac{\partial \mathcal{E}}{\partial \boldsymbol{C}_p^{-1}} : \left.\frac{\partial}{\partial t}\right|_{\boldsymbol{X}} \boldsymbol{C}_p^{-1} = \boldsymbol{\tau} : \boldsymbol{l}_p. \tag{30}$$

Utilising the expression $\boldsymbol{\tau} = \boldsymbol{P}\boldsymbol{F}^T$ and the plastic rate of deformation as described in (21), the last term in (30) can be alternatively expressed as

$$\boldsymbol{\tau} : \boldsymbol{l}_p = -\left[\frac{1}{2} \boldsymbol{F}^T \boldsymbol{P} \boldsymbol{C}_p\right] : \left.\frac{\partial}{\partial t}\right|_{\boldsymbol{X}} \boldsymbol{C}_p^{-1}. \tag{31}$$

Substituting (31) into (30) and comparing them leads to

$$\frac{\partial \mathcal{E}}{\partial \boldsymbol{C}_p^{-1}} = \frac{1}{2} \boldsymbol{F}^T \boldsymbol{P} \boldsymbol{C}_p. \tag{32}$$

5. Mesh smoothing procedure

In general, the purpose of the ALE formulation is to serve as an adaptive mesh movement technique, aiming to minimise spatial mesh distortion for improved solution accuracy at potentially lower computational costs. Building on the work of Armero and Love [21], the material-based linear momentum $\boldsymbol{p}_W$ (per unit reference volume) is determined through a conservation-type of law, with the corresponding jump condition, resulting in

$$\left.\frac{\partial}{\partial t}\right|_{\chi} \boldsymbol{p}_{\boldsymbol{W}} - \text{DIV}_{\chi} \boldsymbol{P}_{\boldsymbol{W}} = \boldsymbol{0}; \qquad U_{\chi} \llbracket \boldsymbol{p}_{\boldsymbol{W}} \rrbracket = -\llbracket \boldsymbol{P}_{\boldsymbol{W}} \rrbracket \boldsymbol{N}_{\chi}. \tag{33}$$

Here, $\boldsymbol{p}_{\boldsymbol{W}} = \rho_R \boldsymbol{W}$ and $\boldsymbol{P}_{\boldsymbol{W}}$ represents the first Piola Kirchhoff stress associated with the material motion. This conservation equation tracks the material velocity $\boldsymbol{W}$ from the referential domain to the material domain.

The remaining unknown in the above expression is the definition of the stress tensor, a measure of material force per unit area acting on a surface in the reference configuration. This is achieved by introducing the scalar potential function Π through a convex combination between the potential function based on $\boldsymbol{F}_{\boldsymbol{\Psi}}$ and $\bar{\boldsymbol{F}}_{\boldsymbol{\Phi}}$, defined as

$$\Pi(\boldsymbol{F}_{\boldsymbol{\Psi}}, \boldsymbol{F}_{\boldsymbol{\Phi}}) = (1-\alpha)\hat{\Psi}(\boldsymbol{F}_{\boldsymbol{\Psi}}) + \alpha \hat{\Psi}(\bar{\boldsymbol{F}}_{\boldsymbol{\Phi}}), \tag{34}$$

where the distortion of the spatial mesh relative to the reference mesh is characterised by $\bar{\boldsymbol{F}}_{\boldsymbol{\Phi}} = \bar{\boldsymbol{F}}(\boldsymbol{F})\boldsymbol{F}_{\boldsymbol{\Psi}}$. Here, the function $\bar{\boldsymbol{F}}(\boldsymbol{F})$ is designed to selectively incorporate certain aspects of deformation pertinent to the specific problem being addressed. We refer to the numerical examples presented in Section 9 that demonstrate this concept. In the equation above, the terms on the right-hand side depend on the deviatoric component of a constitutive model $\hat{\Psi}$. The non-dimensional parameter α ranges from 0 to 1.

Differentiating expression (34) in time for a given deformation gradient $\boldsymbol{F}$ provides

$$\begin{aligned} \boldsymbol{P}_{\boldsymbol{W}} : \left.\frac{\partial}{\partial t}\right|_{\chi} \boldsymbol{F}_{\boldsymbol{\Psi}} &= \left.\frac{\partial}{\partial t}\right|_{\chi} \Pi(\boldsymbol{F}_{\boldsymbol{\Psi}}, \bar{\boldsymbol{F}}_{\boldsymbol{\Phi}}) \\ &= \left[(1-\alpha)\frac{\partial \hat{\Psi}(\boldsymbol{F}_{\boldsymbol{\Psi}})}{\partial \boldsymbol{F}_{\boldsymbol{\Psi}}}\right] : \left.\frac{\partial}{\partial t}\right|_{\chi} \boldsymbol{F}_{\boldsymbol{\Psi}} + \alpha \frac{\partial \hat{\Psi}(\bar{\boldsymbol{F}}_{\boldsymbol{\Phi}})}{\partial \bar{\boldsymbol{F}}_{\boldsymbol{\Phi}}} : \left(\bar{\boldsymbol{F}} \left.\frac{\partial}{\partial t}\right|_{\chi} \boldsymbol{F}_{\boldsymbol{\Psi}}\right) \\ &= \left[(1-\alpha)\frac{\partial \hat{\Psi}(\boldsymbol{F}_{\boldsymbol{\Psi}})}{\partial \boldsymbol{F}_{\boldsymbol{\Psi}}} + \alpha \bar{\boldsymbol{F}}^T \frac{\partial \hat{\Psi}(\bar{\boldsymbol{F}}_{\boldsymbol{\Phi}})}{\partial \bar{\boldsymbol{F}}_{\boldsymbol{\Phi}}}\right] : \left.\frac{\partial}{\partial t}\right|_{\chi} \boldsymbol{F}_{\boldsymbol{\Psi}}, \end{aligned} \tag{35}$$

from which gives

$$\boldsymbol{P}_{\boldsymbol{W}} = (1-\alpha)\frac{\partial \hat{\Psi}(\boldsymbol{F}_{\boldsymbol{\Psi}})}{\partial \boldsymbol{F}_{\boldsymbol{\Psi}}} + \alpha \bar{\boldsymbol{F}}^T \frac{\partial \hat{\Psi}(\bar{\boldsymbol{F}}_{\boldsymbol{\Phi}})}{\partial \bar{\boldsymbol{F}}_{\boldsymbol{\Phi}}}. \tag{36}$$

Remark 4 To suppress unwanted oscillations resulting from the mesh motion, a simple technique is to incorporate Rayleigh type of damping. This damping force can be integrated into the material-based linear momentum conservation equation (33), yielding

$$\left.\frac{\partial}{\partial t}\right|_{\chi} \boldsymbol{p}_{\boldsymbol{W}} - \mathrm{DIV}_{\chi} \boldsymbol{P}_{\boldsymbol{W}} = -\zeta \boldsymbol{p}_{\boldsymbol{W}}. \tag{37}$$

Here, the coefficient ζ (per second) controls the amount of numerical artificial viscosity introduced to the material mesh motion.

6. Ballistic energy and second law of thermodynamics

To provide a meaningful physical interpretation to the conjugate fields of the underlying system (15), consider the *Ballistic* energy $\mathcal{B}_{\chi}$ per unit of referential volume defined by

$$\mathcal{B}_{\chi}(\chi,t) = \hat{\mathcal{B}}_{\chi}(\boldsymbol{p}_{\chi}, \boldsymbol{F}_{\boldsymbol{\Phi}}, \boldsymbol{F}_{\boldsymbol{\Psi}}, J_{\boldsymbol{\Psi}}, \eta_{\chi}, \boldsymbol{C}_p^{-1}) = \frac{1}{2\rho_{\chi}} \boldsymbol{p}_{\chi} \cdot \boldsymbol{p}_{\chi} + J_{\boldsymbol{\Psi}} \mathcal{E}\left(\boldsymbol{F}\left(\boldsymbol{F}_{\boldsymbol{\Phi}}, \boldsymbol{F}_{\boldsymbol{\Psi}}\right), J_{\boldsymbol{\Psi}}^{-1} \eta_{\chi}, \boldsymbol{C}_p^{-1}\right) - \theta_R \eta_{\chi}, \tag{38}$$

with $\rho_{\chi} = J_{\boldsymbol{\Psi}} \rho_R$ and $\mathcal{B}_{\chi}(\chi,t)$ and $\hat{\mathcal{B}}_{\chi}(\boldsymbol{p}_{\chi}, \boldsymbol{F}_{\boldsymbol{\Phi}}, \boldsymbol{F}_{\boldsymbol{\Psi}}, J_{\boldsymbol{\Psi}}, \eta_{\chi}, \boldsymbol{C}_p^{-1})$ represent alternative functional representations of the same magnitude. In this equation, the first term of the right-hand side denotes kinetic energy, the second term represents internal energy and the third term represents thermal energy.

With appropriate energy conjugate fields for the two deformation measures $\{\boldsymbol{F}_{\boldsymbol{\Phi}}, \boldsymbol{F}_{\boldsymbol{\Psi}}\}$ defined as

$$\boldsymbol{P}_{\boldsymbol{\Phi}} = J_{\boldsymbol{\Psi}} \frac{\partial \mathcal{E}(\boldsymbol{F}(\boldsymbol{F}_{\boldsymbol{\Phi}}, \boldsymbol{F}_{\boldsymbol{\Psi}}), J_{\boldsymbol{\Psi}}^{-1} \eta_{\chi}, \boldsymbol{C}_p^{-1})}{\partial \boldsymbol{F}_{\boldsymbol{\Phi}}}; \qquad \boldsymbol{P}_{\boldsymbol{\Psi}} = J_{\boldsymbol{\Psi}} \frac{\partial \mathcal{E}(\boldsymbol{F}(\boldsymbol{F}_{\boldsymbol{\Phi}}, \boldsymbol{F}_{\boldsymbol{\Psi}}), J_{\boldsymbol{\Psi}}^{-1} \eta_{\chi}, \boldsymbol{C}_p^{-1})}{\partial \boldsymbol{F}_{\boldsymbol{\Psi}}}, \tag{39}$$

along with the energy conjugate to the entropy density η_{χ}

$$\theta = J_{\boldsymbol{\Psi}} \frac{\partial \mathcal{E}(\boldsymbol{F}(\boldsymbol{F}_{\boldsymbol{\Phi}}, \boldsymbol{F}_{\boldsymbol{\Psi}}), J_{\boldsymbol{\Psi}}^{-1} \eta_{\chi}, \boldsymbol{C}_p^{-1})}{\partial \eta_{\chi}}, \tag{40}$$

the associated work conjugates $\boldsymbol{\mathcal{V}}_{\chi}$ become

$$\boldsymbol{\mathcal{V}}_{\chi} = \begin{bmatrix} \dfrac{\partial \hat{\mathcal{B}}_{\chi}}{\partial \boldsymbol{p}_{\chi}} \\[2ex] \dfrac{\partial \hat{\mathcal{B}}_{\chi}}{\partial \boldsymbol{F}_{\boldsymbol{\Phi}}} \\[2ex] \dfrac{\partial \hat{\mathcal{B}}_{\chi}}{\partial \boldsymbol{F}_{\boldsymbol{\Psi}}} \\[2ex] \dfrac{\partial \hat{\mathcal{B}}_{\chi}}{\partial J_{\boldsymbol{\Psi}}} \\[2ex] \dfrac{\partial \hat{\mathcal{B}}_{\chi}}{\partial \eta_{\chi}} \\[2ex] \dfrac{\partial \hat{\mathcal{B}}_{\chi}}{\partial \boldsymbol{C}_p^{-1}} \end{bmatrix} = \begin{bmatrix} \boldsymbol{v} \\ \boldsymbol{P}_{\boldsymbol{\Phi}} \\ \boldsymbol{P}_{\boldsymbol{\Psi}} \\ -\mathcal{L} \\ \vartheta \\ J_{\boldsymbol{\Psi}} \dfrac{\partial \mathcal{E}}{\partial \boldsymbol{C}_p^{-1}} \end{bmatrix} = \begin{bmatrix} \boldsymbol{v} \\ \boldsymbol{P}\boldsymbol{H}_{\boldsymbol{\Psi}} \\ -\boldsymbol{F}^T \boldsymbol{P}\boldsymbol{H}_{\boldsymbol{\Psi}} \\ -\mathcal{L} \\ \vartheta \\ \frac{1}{2} J_{\boldsymbol{\Psi}} \boldsymbol{F}^T \boldsymbol{P}\boldsymbol{C}_p \end{bmatrix}. \tag{41}$$

Use is made of (32). Here, $\vartheta = \theta - \theta_R$ represents the temperature difference and $\mathcal{L} = \mathcal{K} - \left(\mathcal{E}(\boldsymbol{F}, \eta_{\boldsymbol{\chi}}) - \theta \eta_{\boldsymbol{\chi}}\right)$ denotes the (thermal-mechanical based) Lagrangian function, defined as a combination of the kinetic energy $\mathcal{K} = \frac{1}{2}\rho_R(\boldsymbol{v} \cdot \boldsymbol{v})$ and the Helmholtz's free energy functional $\mathcal{E}(\boldsymbol{F}, \eta_{\boldsymbol{\chi}}) - \theta \eta_{\boldsymbol{\chi}}$.

It is instructive to revisit the global version of the second law of thermodynamics expressed in terms of the *Ballistic* energy density $\hat{\mathcal{B}}$. In this work, we examine the second law particularised to the case of a prescribed material mesh motion, that is, $\boldsymbol{p}_{\boldsymbol{W}}$ will be assumed to be known *ab initio* or prescribed. This implies that the corresponding conservation law (33) can be removed from the analysis presented below. By employing expression (41), we can obtain the time derivative of the *Ballistic* energy using the chain rule

$$\begin{aligned} \frac{d}{dt} \int_{\Omega_{\chi}} \mathcal{B}_{\chi} \, d\Omega_{\chi} &= \int_{\Omega_{\chi}} \left.\frac{\partial}{\partial t}\right|_{\chi} \hat{\mathcal{B}}_{\chi}(\boldsymbol{p}_{\chi}, \boldsymbol{F}_{\boldsymbol{\Phi}}, \boldsymbol{F}_{\boldsymbol{\Psi}}, J_{\boldsymbol{\Psi}}, \eta_{\chi}, \boldsymbol{C}_p^{-1}) \, d\Omega_{\chi} \\ &= \int_{\Omega_{\chi}} \left(\boldsymbol{v} \cdot \left.\frac{\partial}{\partial t}\right|_{\chi} \boldsymbol{p}_{\chi} + \boldsymbol{P}_{\boldsymbol{\Phi}} : \left.\frac{\partial}{\partial t}\right|_{\chi} \boldsymbol{F}_{\boldsymbol{\Phi}} + \boldsymbol{P}_{\boldsymbol{\Psi}} : \left.\frac{\partial}{\partial t}\right|_{\chi} \boldsymbol{F}_{\boldsymbol{\Psi}} - \mathcal{L} \left.\frac{\partial}{\partial t}\right|_{\chi} J_{\boldsymbol{\Psi}} \right) d\Omega_{\chi} \\ &\quad + \int_{\Omega_{\chi}} \left(\vartheta \left.\frac{\partial}{\partial t}\right|_{\chi} \eta_{\chi} + J_{\boldsymbol{\Psi}} \frac{\partial \mathcal{E}}{\partial \boldsymbol{C}_p^{-1}} : \left.\frac{\partial}{\partial t}\right|_{\chi} \boldsymbol{C}_p^{-1} \right) d\Omega_{\chi}. \end{aligned} \tag{42}$$

Further expanding this expression yields

$$\begin{aligned}\frac{d}{dt}\int\limits_{\Omega_\chi} \mathcal{B}_\chi \, d\Omega_\chi = &\int\limits_{\Omega_\chi} \left(\boldsymbol{v} \cdot \left.\frac{\partial}{\partial t}\right|_{\chi} \boldsymbol{p}_\chi + \left(\boldsymbol{P}\boldsymbol{H}_{\boldsymbol{\Psi}}\right) : \left.\frac{\partial}{\partial t}\right|_{\chi} \boldsymbol{F}_{\boldsymbol{\Phi}} + \left(\boldsymbol{\Sigma}\boldsymbol{H}_{\boldsymbol{\Psi}}\right) : \left.\frac{\partial}{\partial t}\right|_{\chi} \boldsymbol{F}_{\boldsymbol{\Psi}} \right) d\Omega_\chi \\ &+ \int\limits_{\Omega_\chi} \left(\vartheta \left.\frac{\partial}{\partial t}\right|_{\chi} \eta_\chi + J_{\boldsymbol{\Psi}} \frac{\partial \mathcal{E}}{\partial \boldsymbol{C}_p^{-1}} : \left.\frac{\partial}{\partial t}\right|_{\chi} \boldsymbol{C}_p^{-1} \right) d\Omega_\chi .\end{aligned} \tag{43}$$

Pairs such as $\left\{ \boldsymbol{v}, \left.\frac{\partial}{\partial t}\right|_{\chi} \boldsymbol{p}_\chi \right\}$, $\left\{ \boldsymbol{P}\boldsymbol{H}_{\boldsymbol{\Psi}}, \left.\frac{\partial}{\partial t}\right|_{\chi} \boldsymbol{F}_{\boldsymbol{\Phi}} \right\}$, $\left\{ \boldsymbol{\Sigma}\boldsymbol{H}_{\boldsymbol{\Psi}}, \left.\frac{\partial}{\partial t}\right|_{\chi} \boldsymbol{F}_{\boldsymbol{\Psi}} \right\}$ and $\left\{ \vartheta, \left.\frac{\partial}{\partial t}\right|_{\chi} \eta_\chi \right\}$ are said to be dual or work conjugate with respect to the referential volume, yielding work rate per unit of referential volume. For instance, the energy conjugate field to the time rate of the material-based deformation gradient is the classical (material-based) Eshelby stress tensor defined as $\boldsymbol{\Sigma} = -\left(\boldsymbol{F}^T \boldsymbol{P} + \mathcal{L}\boldsymbol{I}\right)$.

Note that the last term in the integrand in above equation (43), referred to as the rate of the plastic dissipation introduced by the plasticity model can be expressed in various alternative ways as

$$\left.\frac{\partial}{\partial t}\right|_{\chi} \mathcal{D}^{\chi}_{\text{Phy}} = -\frac{\partial \hat{\mathcal{B}}_\chi}{\partial \boldsymbol{C}_p^{-1}} : \left.\frac{\partial}{\partial t}\right|_{\chi} \boldsymbol{C}_p^{-1} = -J_{\boldsymbol{\Psi}} \frac{\partial \mathcal{E}}{\partial \boldsymbol{C}_p^{-1}} : \left.\frac{\partial}{\partial t}\right|_{\chi} \boldsymbol{C}_p^{-1}. \tag{44}$$

Consequently, by substituting the linear momentum equation (8a) and the geometric conservation equations (8b) and (8c) into expression (43), we arrive at

$$\begin{aligned}\frac{d}{dt}\int\limits_{\Omega_\chi} \mathcal{B}_\chi \, d\Omega_\chi = &\int\limits_{\Omega_\chi} \left[\text{DIV}_\chi \left(\left(\boldsymbol{P}\boldsymbol{H}_{\boldsymbol{\Psi}}\right)^T \boldsymbol{v} + 2\mathcal{K}\boldsymbol{H}_{\boldsymbol{\Psi}}^T \boldsymbol{W} \right) + \boldsymbol{v} \cdot \boldsymbol{f}_\chi - \boldsymbol{\nabla}_\chi \mathcal{K} \cdot \left(\boldsymbol{H}_{\boldsymbol{\Psi}}^T \boldsymbol{W}\right) \right] d\Omega_\chi \\ &+ \int\limits_{\Omega_\chi} \underbrace{\left[-\left(\boldsymbol{P}\boldsymbol{H}_{\boldsymbol{\Psi}}\right) : \boldsymbol{\nabla}_\chi \boldsymbol{v} + \left(\boldsymbol{P}\boldsymbol{H}_{\boldsymbol{\Psi}}\right) : \boldsymbol{\nabla}_\chi \hat{\boldsymbol{v}} + \left(\boldsymbol{\Sigma}\boldsymbol{H}_{\boldsymbol{\Psi}}\right) : \boldsymbol{\nabla}_\chi \boldsymbol{W} \right]}_{\left(\frac{\partial \mathcal{E}}{\partial \boldsymbol{F}} : \frac{\partial \boldsymbol{F}}{\partial \chi}\right) \cdot \left(\boldsymbol{H}_{\boldsymbol{\Psi}}^T \boldsymbol{W}\right) - \mathcal{L}\boldsymbol{H}_{\boldsymbol{\Psi}} : \boldsymbol{\nabla}_\chi \boldsymbol{W}} d\Omega_\chi \\ &+ \int\limits_{\Omega_\chi} \vartheta \left.\frac{\partial}{\partial t}\right|_{\chi} \eta_\chi d\Omega_\chi - \int\limits_{\Omega_\chi} \left.\frac{\partial}{\partial t}\right|_{\chi} \mathcal{D}^{\chi}_{\text{Phy}} \, d\Omega_\chi .\end{aligned} \tag{45}$$

Moreover, considering the referential gradient of the Lagrangian function represented by $\boldsymbol{\nabla}_\chi \mathcal{L} = \boldsymbol{\nabla}_\chi \mathcal{K} - \boldsymbol{\nabla}_\chi \left(\mathcal{E}\left(\boldsymbol{F}, \eta_{\boldsymbol{X}}, \boldsymbol{C}_p^{-1}\right) - \theta \eta_{\boldsymbol{X}} \right)$, and utilising the relationship $\mathcal{L}\boldsymbol{H}_{\boldsymbol{\Psi}} : \boldsymbol{\nabla}_\chi \boldsymbol{W} = \text{DIV}_\chi \left(\mathcal{L}\boldsymbol{H}_{\boldsymbol{\Psi}}^T \boldsymbol{W}\right) - \left(\boldsymbol{\nabla}_\chi \mathcal{L}\right) \cdot \left(\boldsymbol{H}_{\boldsymbol{\Psi}}^T \boldsymbol{W}\right)$, the above expression, after some careful algebraic manipulation, reduces to

$$\begin{aligned}\frac{d}{dt}\int\limits_{\Omega_\chi} \mathcal{B}_\chi \, d\Omega_\chi = &\int\limits_{\Omega_\chi} \left(\text{DIV}_\chi \left(\left(\boldsymbol{P}\boldsymbol{H}_{\boldsymbol{\Psi}}\right)^T \boldsymbol{v} + (2\mathcal{K} - \mathcal{L})\, \boldsymbol{H}_{\boldsymbol{\Psi}}^T \boldsymbol{W} \right) + \boldsymbol{v} \cdot \boldsymbol{f}_\chi + \boldsymbol{\nabla}_\chi \theta \cdot \left(\eta \boldsymbol{H}_{\boldsymbol{\Psi}}^T \boldsymbol{W}\right) \right) d\Omega_\chi \\ &+ \int\limits_{\Omega_\chi} \vartheta \left.\frac{\partial}{\partial t}\right|_{\chi} \eta_\chi d\Omega_\chi - \int\limits_{\Omega_\chi} J_{\boldsymbol{\Psi}} \underbrace{\left[-\frac{\partial \mathcal{E}}{\partial \boldsymbol{C}_p^{-1}} : \left.\frac{\partial}{\partial t}\right|_{\boldsymbol{X}} \boldsymbol{C}_p^{-1} \right]}_{\dot{\mathcal{D}}_{\text{Phy}}} d\Omega_\chi ,\end{aligned} \tag{46}$$

with the physical dissipation term $\dot{\mathcal{D}}_{\text{Phy}}$ featuring in the integrand of the last term of above equation. Furthermore, by substituting the entropy density equation (11) into (46), and noting that $\vartheta \text{DIV}_\chi \left(\eta \boldsymbol{H}_{\boldsymbol{\Psi}}^T \boldsymbol{W}\right) = \text{DIV}_\chi \left(\vartheta \eta \boldsymbol{H}_{\boldsymbol{\Psi}}^T \boldsymbol{W}\right) - \boldsymbol{\nabla}_\chi \theta \left(\eta \boldsymbol{H}_{\boldsymbol{\Psi}}^T \boldsymbol{W}\right)$, equation (46) becomes

$$\frac{d}{dt}\int\limits_{\Omega_\chi} \mathcal{B}_\chi \, d\Omega_\chi - \dot{\Pi}^{\text{ext}}_\chi - \mathcal{Q}^{\text{ext}}_\chi = \int\limits_{\Omega_\chi} \frac{\theta_R}{\theta^2} \boldsymbol{Q}_\chi \cdot \boldsymbol{\nabla}_\chi \theta \, d\Omega_\chi - \int\limits_{\Omega_\chi} \underbrace{\frac{\theta_R}{\theta} J_{\boldsymbol{\Psi}} \dot{\mathcal{D}}_{\text{Phy}}}_{\geq 0} d\Omega_\chi . \tag{47}$$

Observing that in the above expression, the material time rate of physical plastic dissipation is always non-negative (that is, $\dot{\mathcal{D}}_{\text{Phy}} \geq 0$). Here, $\dot{\Pi}^{\text{ext}}_\chi$ being the mechanical power associated with external forces as

$$\dot{\Pi}^{\text{ext}}_\chi = \int\limits_{\Omega_\chi} \boldsymbol{v} \cdot \boldsymbol{f}_\chi \, d\Omega_\chi + \int\limits_{\partial\Omega_\chi} \boldsymbol{v}_B \cdot \boldsymbol{t}_B \, dA_\chi ; \qquad \boldsymbol{t}_B = \boldsymbol{P}\boldsymbol{H}_{\boldsymbol{\Psi}} \boldsymbol{N}_\chi , \tag{48}$$

and $\mathcal{Q}^{\text{ext}}_\chi$ being the heat source and heat flux added (removed) to (from) the system as

$$\mathcal{Q}^{\text{ext}}_\chi = \int\limits_{\Omega_\chi} \frac{\vartheta}{\theta} r_\chi \, d\Omega_\chi - \int\limits_{\partial\Omega_\chi} \frac{\vartheta}{\theta} q_B \, dA_\chi . \tag{49}$$

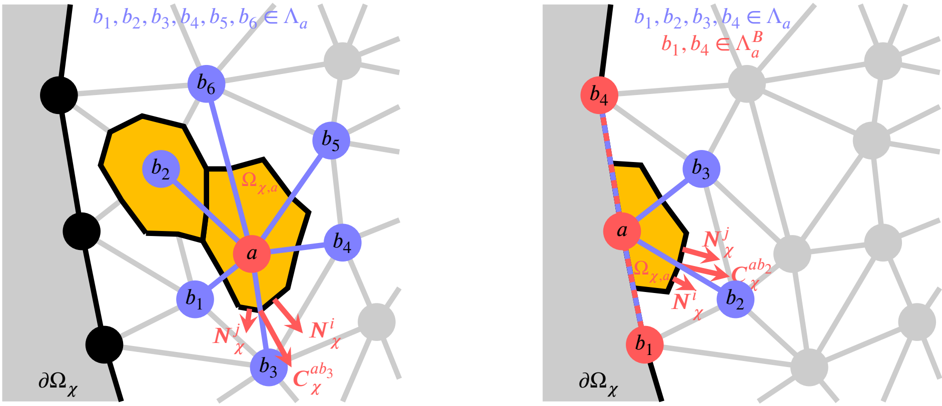

(a) Interior nodes.

(b) Boundary nodes.

Fig. 2. Control volumes for (a) an interior node and (b) a boundary node for a median dual tessellation visualised in 2D.

Recalling Fourier's law of heat conduction (13), the first term on the right-hand side of expression (47) is non-positive, as demonstrated below

$$\boldsymbol{Q}_\chi \cdot \boldsymbol{\nabla}_\chi\theta = -\left(\boldsymbol{K}_\chi\boldsymbol{\nabla}_\chi\theta\right)\cdot\boldsymbol{\nabla}_\chi\theta = -\boldsymbol{K}_\chi : \left(\boldsymbol{\nabla}_\chi\theta\otimes\boldsymbol{\nabla}_\chi\theta\right)\le 0. \tag{50}$$

With this at hand, equation (47) can finally be transformed into the following inequality

$$\frac{d}{dt}\int_{\Omega_\chi}\mathcal{B}_\chi\,d\Omega_\chi - \dot{\Pi}^{\text{ext}}_\chi - \mathcal{Q}^{\text{ext}}_\chi \le 0. \tag{51}$$

This inequality represents a valid expression for the second law of thermodynamics of a system. Satisfaction of inequality (51) is a necessary *ab initio* condition to ensure stability, commonly known as the classical Coleman–Noll procedure. This concept will be further exploited in Section 7.2 when introducing Godunov-type numerical dissipation to the finite volume spatial discretisation.

7. Numerical scheme

7.1. Vertex-centred finite volume spatial discretisation

The vertex centred finite volume spatial discretisation presented in this work requires the introduction of a median dual mesh [41,55,62,63] for defining control volumes (see Fig. 2). With this in mind and employing Gauss divergence theorem, expression (15) can be spatially discretised over a fixed referential control volume Ω^a_χ to give

$$\Omega^a_\chi \frac{d}{dt}\boldsymbol{\mathcal{U}}^a_\chi = -\int_{\partial\Omega^a_\chi}\boldsymbol{\mathcal{F}}_{\boldsymbol{N}_\chi}\,dA_\chi + \Omega^a_\chi\boldsymbol{\mathcal{S}}^a_\chi. \tag{52}$$

Here, $\boldsymbol{\mathcal{U}}^a_\chi$ and $\boldsymbol{\mathcal{S}}^a_\chi$ are the average values of both the conservation variables and source term vector within the fixed referential control volume, respectively. Moreover, the surface integral of (52) is approximated through a second-order central difference scheme, resulting in

$$\Omega^a_\chi \frac{d}{dt}\boldsymbol{\mathcal{U}}^a_\chi = -\left(\sum_{b\in\Lambda_a}\boldsymbol{\mathcal{F}}^I_{\boldsymbol{N}^{ab}_\chi}\|\boldsymbol{C}^{ab}_\chi\| + \sum_{\gamma\in\Lambda^B_a}\boldsymbol{\mathcal{F}}^B_{\chi,a}\boldsymbol{C}^\gamma_\chi\right) + \Omega^a_\chi\boldsymbol{\mathcal{S}}^a_\chi, \tag{53}$$

where $b\in\Lambda_a$ represents the set of neighbouring control volumes b associated with the control volume a and $\boldsymbol{C}^\gamma_\chi = \frac{A_\gamma}{3}\boldsymbol{N}_\gamma$ represents the (tributary) boundary area vector. For a given edge connecting nodes a and b, the mean referential area vector $\boldsymbol{C}^{ab}_\chi$ satisfies the reciprocal relation, for instance $\boldsymbol{C}^{ab}_\chi = -\boldsymbol{C}^{ba}_\chi$. The terms within the parenthesis in (53) correspond to the evaluation of both internal interface fluxes $\boldsymbol{\mathcal{F}}^I_{\boldsymbol{N}^{ab}_\chi}$ and boundary fluxes $\boldsymbol{\mathcal{F}}^B_{\chi,a}$. This evaluation comprises a summation over edges (first term in the parenthesis) and a summation over boundary faces (second term in the parenthesis). The internal flux $\boldsymbol{\mathcal{F}}^I_{\boldsymbol{N}^{ab}_\chi} = \frac{1}{2}\left[\boldsymbol{\mathcal{F}}_{\boldsymbol{N}_\chi}(\boldsymbol{\mathcal{U}}_a) + \boldsymbol{\mathcal{F}}_{\boldsymbol{N}_\chi}(\boldsymbol{\mathcal{U}}_b)\right]$ denotes the average states of the left and the right control volumes of a given edge ab. The boundary flux $\boldsymbol{\mathcal{F}}^B_a$ is enforced through either Dirichlet or Neumann boundaries.

Expression (53) is now particularised to the specific variables addressed in this paper, resulting in the following semi-discrete equations

$$\Omega^a_\chi \frac{d}{dt}\boldsymbol{p}^a_\chi = \boldsymbol{T}^a_\chi + \sum_{\gamma\in\Lambda^B_a} \boldsymbol{t}^B_a ||\boldsymbol{C}^\gamma_\chi|| + \Omega^a_\chi \boldsymbol{f}^a_\chi; \tag{54a}$$

$$\Omega^a_\chi \frac{d}{dt}\boldsymbol{F}^a_{\boldsymbol{\Phi}} = \sum_{b\in\Lambda_a} \frac{1}{2}\left(\hat{\boldsymbol{v}}_a + \hat{\boldsymbol{v}}_b\right) \otimes \boldsymbol{C}^{ab}_\chi + \sum_{\gamma\in\Lambda^B_a} \hat{\boldsymbol{v}}^B_a \otimes \boldsymbol{C}^\gamma_\chi; \tag{54b}$$

$$\Omega^a_\chi \frac{d}{dt}\boldsymbol{F}^a_{\boldsymbol{\Psi}} = \sum_{b\in\Lambda_a} \frac{1}{2}\left(\boldsymbol{W}_a + \boldsymbol{W}_b\right) \otimes \boldsymbol{C}^{ab}_\chi + \sum_{\gamma\in\Lambda^B_a} \boldsymbol{W}^B_a \otimes \boldsymbol{C}^\gamma_\chi; \tag{54c}$$

$$\Omega^a_\chi \frac{d}{dt}J^a_{\boldsymbol{\Psi}} = \sum_{b\in\Lambda_a} \frac{1}{2}\left[\left(\boldsymbol{H}^{a,T}_{\boldsymbol{\Psi}} \boldsymbol{W}_a\right) + \left(\boldsymbol{H}^{b,T}_{\boldsymbol{\Psi}} \boldsymbol{W}_b\right)\right] \cdot \boldsymbol{C}^{ab}_\chi + \sum_{\gamma\in\Lambda^B_a} \boldsymbol{W}^B_a \cdot \left(\boldsymbol{H}^a_{\boldsymbol{\Psi}} \boldsymbol{C}^\gamma_\chi\right); \tag{54d}$$

$$\begin{aligned}\Omega^a_\chi \frac{d}{dt}\eta^a_\chi = {} & \sum_{b\in\Lambda_a} \frac{1}{2}\left(\eta^a_{\boldsymbol{X}} \boldsymbol{H}^{a,T}_{\boldsymbol{\Psi}} \boldsymbol{W}_a + \eta^b_{\boldsymbol{X}} \boldsymbol{H}^{b,T}_{\boldsymbol{\Psi}} \boldsymbol{W}_b\right) \cdot \boldsymbol{C}^{ab}_\chi - \sum_{b\in\Lambda_a} \frac{1}{2}\left(\frac{\boldsymbol{Q}^a_\chi}{\theta_a} + \frac{\boldsymbol{Q}^b_\chi}{\theta_b}\right) \cdot \boldsymbol{C}^{ab}_\chi \\ & - \sum_{\gamma\in\Lambda^B_a} \frac{Q^a_B}{\theta^a_B} \|\boldsymbol{C}^\gamma_\chi\| - \frac{1}{\theta^2_a} \boldsymbol{Q}^a_\chi \cdot \left[\sum_{b\in\Lambda_a} \frac{1}{2}\left(\theta_a + \theta_b\right) \boldsymbol{C}^{ab}_\chi\right] + \Omega^a_\chi \frac{J^a_{\boldsymbol{\Psi}}}{\theta_a}\left(s^a_{\boldsymbol{X}} + \dot{\mathcal{D}}^a_{\text{Phy}}\right);\end{aligned} \tag{54e}$$

$$\Omega^a_\chi \frac{d}{dt}\boldsymbol{p}^a_{\boldsymbol{W}} = \boldsymbol{T}^a_{\boldsymbol{W}} + \sum_{\gamma\in\Lambda^B_a} \boldsymbol{t}^W_a ||\boldsymbol{C}^\gamma_\chi|| - \zeta \boldsymbol{p}^a_{\boldsymbol{W}}. \tag{54f}$$

In expression (54a), $\boldsymbol{T}^a_\chi$ represents the internal nodal force defined as $\boldsymbol{T}^a_\chi = \sum_{b\in\Lambda_a} \frac{1}{2}\left(\boldsymbol{P}^a_\chi + \boldsymbol{P}^b_\chi\right)\boldsymbol{C}^{ab}_\chi$. The boundary traction, denoted as $\boldsymbol{t}^B_a$, is described by the expression $\boldsymbol{t}^B_a = \boldsymbol{P}^a_\chi \boldsymbol{N}^a_\chi$. Likewise, the term $\boldsymbol{T}^a_{\boldsymbol{W}}$ in (54f) represents the node-based material force and is defined as $\boldsymbol{T}^a_{\boldsymbol{W}} = \sum_{b\in\Lambda_a} \frac{1}{2}\left(\boldsymbol{P}^a_{\boldsymbol{W}} + \boldsymbol{P}^b_{\boldsymbol{W}}\right)\boldsymbol{C}^{ab}_\chi$.

Equations (54a), (54d) and (54e) correspond to the conservation of linear momentum, mass and total energy, respectively. Complementing these physical principles, Equations (54b) and (54c) introduce an additional set of geometric conservation equations. Lastly, equation (54f) characterises the ALE material mesh motion, providing a full representation of the physical and geometric aspects within the system.

For the case of thermo-elasticity, the motion of solids is sufficiently described by the expressions from (54a) to (54f), along with the condition $\dot{\mathcal{D}}^a_{\text{Phy}} = 0$. However, exploring plasticity within the framework of first-order system requires further incorporation of evolution expressions for the associated plastic state variables, expressed in (29a) and (29b). The corresponding semi-discrete equations are

$$J^a_{\boldsymbol{\Psi}} \left.\frac{\partial}{\partial t}\right|_\chi \boldsymbol{C}^{-1,a}_p = \frac{1}{\Omega^a_\chi} \sum_{b\in\Lambda_a} \left[\frac{1}{2}\left(\boldsymbol{C}^{-1,a}_p + \boldsymbol{C}^{-1,b}_p\right) \otimes \boldsymbol{C}^{ab}_\chi\right]\left(\boldsymbol{H}^{a,T}_{\boldsymbol{\Psi}} \boldsymbol{W}_a\right) - 2J^a_{\boldsymbol{\Psi}} \dot{\gamma}_a \boldsymbol{F}^{-1}_a \left.\frac{\partial f}{\partial \boldsymbol{\tau}}\right|_a \boldsymbol{b}^a_e \boldsymbol{F}^{-T}_a; \tag{55a}$$

$$J^a_{\boldsymbol{\Psi}} \left.\frac{\partial}{\partial t}\right|_\chi \bar{\varepsilon}^a_p = \frac{1}{\Omega^a_\chi} \sum_{b\in\Lambda_a} \left[\frac{1}{2}\left(\bar{\varepsilon}^a_p + \bar{\varepsilon}^b_p\right) \boldsymbol{C}^{ab}_\chi\right] \cdot \left(\boldsymbol{H}^{a,T}_{\boldsymbol{\Psi}} \boldsymbol{W}_a\right) + J^a_{\boldsymbol{\Psi}} \dot{\gamma}_a, \tag{55b}$$

respectively.

Additionally, monitoring both spatial and material geometries is useful to assess the effectiveness of the material mesh movement. With that in mind, it is convenient to integrate both the spatial velocity $\hat{\boldsymbol{v}}$ and the material velocity $\boldsymbol{W}$ over time by noticing that

$$\frac{d}{dt}\boldsymbol{\Phi}_a = \hat{\boldsymbol{v}}_a; \qquad \frac{d}{dt}\boldsymbol{\Psi}_a = \boldsymbol{W}_a. \tag{56a}$$

As it is well known, the above mixed-based system (54) is prone to exhibit non-physical numerical instabilities [10,34,35,64–68] when attempting to model large strain solid dynamics problems [1,69,70]. To address this issue, a Godunov-type stabilisation term must be suitably introduced to both the internal nodal force $\boldsymbol{T}^a_\chi$ and the material force $\boldsymbol{T}^a_{\boldsymbol{W}}$, as presented below

$$\boldsymbol{T}^a_\chi = \sum_{b\in\Lambda_a} \frac{1}{2}\left(\boldsymbol{P}^a_\chi + \boldsymbol{P}^b_\chi\right)\boldsymbol{C}^{ab}_\chi + \sum_{b\in\Lambda_a} \boldsymbol{\mathcal{D}}^{ab}_{p_\chi} \quad \text{and} \quad \boldsymbol{T}^a_{\boldsymbol{W}} = \sum_{b\in\Lambda_a} \frac{1}{2}\left(\boldsymbol{P}^a_{\boldsymbol{W}} + \boldsymbol{P}^b_{\boldsymbol{W}}\right)\boldsymbol{C}^{ab}_\chi + \sum_{b\in\Lambda_a} \boldsymbol{\mathcal{D}}^{ab}_{p_{\boldsymbol{W}}}. \tag{57}$$

These stabilisation terms, namely $\{\boldsymbol{\mathcal{D}}^{ab}_{p_\chi}, \boldsymbol{\mathcal{D}}^{ab}_{p_{\boldsymbol{W}}}\}$, will be obtained through the semi-discrete version of the classical Coleman–Noll procedure [71], which will be discussed in the following section.

7.2. Numerical entropy production

Based upon the second law of thermodynamics presented in Section 6, we now turn our attention to the semi-discrete form of inequality (51) under the assumption that $\boldsymbol{p}_{\boldsymbol{W}}$ is known or has been prescribed. This stability analysis is demonstrated below.

$$\begin{aligned}\sum_a \Omega_\chi^a \frac{d}{dt}\mathcal{B}_\chi^a &= \sum_a \Omega_\chi^a \left[\boldsymbol{v}_a \cdot \frac{d}{dt}\boldsymbol{p}_\chi^a + \boldsymbol{P}_{\boldsymbol{\Phi}}^a : \frac{d}{dt}\boldsymbol{F}_{\boldsymbol{\Phi}}^a + \boldsymbol{P}_{\boldsymbol{\Psi}}^a : \frac{d}{dt}\boldsymbol{F}_{\boldsymbol{\Psi}}^a - \mathcal{L}_a \frac{d}{dt}J_{\boldsymbol{\Psi}}^a + \vartheta_a \frac{d}{dt}\eta_\chi^a - \frac{d}{dt}\mathcal{D}_{\text{Phy}}^a\right] \\ &= \sum_a \Omega_\chi^a \left[\boldsymbol{v}_a \cdot \frac{d}{dt}\boldsymbol{p}_\chi^a + \left(\boldsymbol{P}_a \boldsymbol{H}_{\boldsymbol{\Psi}}^a\right) : \frac{d}{dt}\boldsymbol{F}_{\boldsymbol{\Phi}}^a - \left(\boldsymbol{F}_a^T \boldsymbol{P}_a \boldsymbol{H}_{\boldsymbol{\Psi}}^a\right) : \frac{d}{dt}\boldsymbol{F}_{\boldsymbol{\Psi}}^a - \mathcal{L}_a \frac{d}{dt}J_{\boldsymbol{\Psi}}^a + \vartheta_a \frac{d}{dt}\eta_\chi^a - \frac{d}{dt}\mathcal{D}_{\text{Phy}}^a\right].\end{aligned} \tag{58}$$

Here, we have incorporated suitable conjugate fields (41) into the first line of (58). Subsequently, we substitute the linear momentum equation (54a), the geometric conservation equation for both spatial and material deformation gradient tensors (54b) and (54c), the mass conservation equation (54d), the first law of thermodynamics (54e) and the evolution equation for the inverse of the inelastic right Cauchy-Green tensor (55a) into the second line of (58). Following some algebraic manipulation, we arrive at

$$\sum_a \Omega_\chi^a \frac{d}{dt}\mathcal{B}_\chi^a - \dot{\Pi}_{\text{ext}} - \mathcal{Q}_{\text{ext}} = \underbrace{-\sum_a \sum_{b\in\Lambda_a} \frac{\vartheta_a}{\Theta_a}\left(\frac{\boldsymbol{Q}_\chi^a + \boldsymbol{Q}_\chi^b}{2}\right)\cdot \boldsymbol{C}_\chi^{ab}}_{\sum_a \sum_{b\in\Lambda_a} \Omega_\chi^a \frac{\theta_R}{\Theta_a\Theta_b}\boldsymbol{Q}_\chi^a \cdot \boldsymbol{\nabla}_\chi \theta(\chi_a,t) \leq 0} - \sum_a \underbrace{J_{\boldsymbol{\Psi}}^a \Omega_\chi^a \frac{\theta_R}{\Theta_a}\dot{\mathcal{D}}_{\text{Phy}}^a}_{\geq 0} - \underbrace{\sum_a \sum_{b\in\Lambda_a}\left(-\boldsymbol{v}_a \cdot \boldsymbol{\mathcal{D}}_{\boldsymbol{p}_\chi}^{ab}\right)}_{\mathcal{D}_{\text{total}}}. \tag{59}$$

Here, $\dot{\Pi}_{\text{ext}}$ and $\mathcal{Q}_{\text{ext}}$ represent the semi-discrete versions of power contribution and total heat contribution, expressed as

$$\dot{\Pi}_{\text{ext}} = \sum_a \Omega_\chi^a \boldsymbol{v}_a \cdot \boldsymbol{f}_\chi^a + \sum_a \sum_{\gamma\in\Lambda_a^B} \boldsymbol{v}_a^B \cdot \boldsymbol{t}_a^B \|\boldsymbol{C}_\chi^\gamma\|; \qquad \mathcal{Q}_{\text{ext}} = \sum_a \Omega_\chi^a \frac{\vartheta_a}{\Theta_a} J_{\boldsymbol{\Psi}}^a s_R^a - \sum_a \sum_{\gamma\in\Lambda_a^B} \frac{\vartheta_a^B}{\Theta_a^B} Q_a^B \|\boldsymbol{C}_\chi^\gamma\|. \tag{60}$$

To adhere to the second law of thermodynamics (51) at semi-discrete level, it is important to prove all the three terms on the right-hand side of (59) are non-negative. Regarding the heat conduction term (first term on the right-hand side of (59)), the inequality is naturally satisfied due to the inherent properties of the conductive heat flux. As for the physical model dissipation term (second term on the right-hand side of (59)), its non-positivity arises from the definition of the material time rate of physical plastic dissipation.

Our subsequent objective is to demonstrate the non-negativity of the numerical dissipation term, denoted as $\mathcal{D}_{\text{total}} \geq 0$. This can be achieved by equivalently swapping indices a and b to give

$$\mathcal{D}_{\text{total}} = -\sum_a \sum_{b\in\Lambda_a}\left(\boldsymbol{v}_a \cdot \boldsymbol{\mathcal{D}}_{\boldsymbol{p}_\chi}^{ab}\right) = -\sum_a \sum_{b\in\Lambda_a}\left(\boldsymbol{v}_b \cdot \boldsymbol{\mathcal{D}}_{\boldsymbol{p}_\chi}^{ba}\right). \tag{61}$$

By simply averaging the first term and the second term of the expression above, and noting the anti-symmetric nature of the stabilisation term as $\boldsymbol{\mathcal{D}}_{\boldsymbol{p}_\chi}^{ba} = -\boldsymbol{\mathcal{D}}_{\boldsymbol{p}_\chi}^{ab}$, an alternative expression for $\mathcal{D}_{\text{total}}$ is shown below

$$\mathcal{D}_{\text{total}} = \frac{1}{2}\sum_a \sum_{b\in\Lambda_a^b} \mathcal{D}_{\text{total}}^{ab}; \qquad \mathcal{D}_{\text{total}}^{ab} = \left(\boldsymbol{v}_b - \boldsymbol{v}_a\right)\cdot \boldsymbol{\mathcal{D}}_{\boldsymbol{p}_\chi}^{ab}. \tag{62}$$

Sufficient conditions for $\mathcal{D}_{\text{total}} \geq 0$ are given by

$$\boldsymbol{\mathcal{D}}_{\boldsymbol{p}_\chi}^{ab} = \boldsymbol{S}_{\boldsymbol{p}_\chi}^{ab}\left(\boldsymbol{v}_b - \boldsymbol{v}_a\right), \tag{63}$$

where $\boldsymbol{S}_{\boldsymbol{p}_\chi}^{ab}$ is a positive semi-definite stabilisation matrix. Following previous work of the authors [26], the dissipation term is chosen as

$$\boldsymbol{S}_{\boldsymbol{p}_\chi}^{ab} = \frac{1}{2}\rho_\chi^{\text{Ave}}\|\boldsymbol{C}_\chi^{ab}\|\left[c_p^{\chi,\text{Ave}}\boldsymbol{n}_{\boldsymbol{x}}^{ab}\otimes \boldsymbol{n}_{\boldsymbol{x}}^{ab} + c_s^{\chi,\text{Ave}}\left(\boldsymbol{I} - \boldsymbol{n}_{\boldsymbol{x}}^{ab}\otimes \boldsymbol{n}_{\boldsymbol{x}}^{ab}\right)\right], \tag{64}$$

where $[\bullet]^{\text{Ave}} = \frac{1}{2}\left([\bullet]_a + [\bullet]_b\right)$. It is noteworthy how the dissipation term is related to the jump in velocity between interacting nodes, a characteristic feature of Godunov-type upwinding terms [59,72–74].

Remark 5 Given that, in general, the ALE mesh motion is not known *a priori* but it will be defined via the first order conservative-type equation (54f), the introduction of an appropriate stabilisation term is necessary to stabilise the convective nature inherent to the equation. In this context, and for simplicity, we propose a stabilisation term $\boldsymbol{\mathcal{D}}_{\boldsymbol{p_W}}^{ab}$ with a mathematical structure similar to that of expression (63) as

$$\boldsymbol{\mathcal{D}}_{\boldsymbol{p_W}}^{ab} = \boldsymbol{S}_{\boldsymbol{p_W}}^{ab}\left(\boldsymbol{W}_b - \boldsymbol{W}_a\right). \tag{65}$$

Here, the positive-definite stabilisation tensor is defined as

$$\boldsymbol{S}_{\boldsymbol{p_W}}^{ab} = \frac{1}{2}\rho_{\boldsymbol{W}}^{\text{Ave}}\|\boldsymbol{C}_\chi^{ab}\|\left[c_p^{\boldsymbol{X},\text{Ave}}\boldsymbol{N}_{\boldsymbol{X}}^{ab}\otimes \boldsymbol{N}_{\boldsymbol{X}}^{ab} + c_s^{\boldsymbol{X},\text{Ave}}\left(\boldsymbol{I} - \boldsymbol{N}_{\boldsymbol{X}}^{ab}\otimes \boldsymbol{N}_{\boldsymbol{X}}^{ab}\right)\right]. \tag{66}$$

7.3. Time integrator

Given the size of the resulting set of semi-discrete equations, the use of an explicit type of time integrator becomes appropriate. In this study, a three stage Runge-Kutta explicit time integrator [32] is employed. This is described by the time update equations from time step t^n to t^{n+1} stated below

$$\begin{aligned}
\boldsymbol{\mathcal{U}}^{\star}_{\chi,a} &= \boldsymbol{\mathcal{U}}^{n}_{\chi,a} + \Delta t\,\dot{\boldsymbol{\mathcal{U}}}^{n}_{\chi,a}\left(\boldsymbol{\mathcal{U}}^{n}_{\chi,a}\right),\\
\boldsymbol{\mathcal{U}}^{\star\star}_{\chi,a} &= \frac{3}{4}\boldsymbol{\mathcal{U}}^{n}_{\chi,a} + \frac{1}{4}\left(\boldsymbol{\mathcal{U}}^{\star}_{\chi,a} + \Delta t\,\dot{\boldsymbol{\mathcal{U}}}^{\star}_{\chi,a}\left(\boldsymbol{\mathcal{U}}^{\star}_{\chi,a}\right)\right),\\
\boldsymbol{\mathcal{U}}^{n+1}_{\chi,a} &= \frac{1}{3}\boldsymbol{\mathcal{U}}^{n}_{\chi,a} + \frac{2}{3}\left(\boldsymbol{\mathcal{U}}^{\star\star}_{\chi,a} + \Delta t\,\dot{\boldsymbol{\mathcal{U}}}^{\star\star}_{\chi,a}\left(\boldsymbol{\mathcal{U}}^{\star\star}_{\chi,a}\right)\right).
\end{aligned} \tag{67}$$

Additionally, both material and spatial geometries are also updated using the same time integrator, resulting in a monolithic time update procedure. The unknowns $\boldsymbol{\mathcal{U}}_{\chi} = \left(\boldsymbol{p}_{\chi}, \boldsymbol{F}_{\boldsymbol{\Phi}}, \boldsymbol{F}_{\boldsymbol{\Psi}}, J_{\boldsymbol{\Psi}}, \eta_{\chi}\right)^T$ are updated alongside the material geometry $\boldsymbol{\Psi}$ and the spatial geometry $\boldsymbol{\Phi}$ through equation (67).

Furthermore, the determination of the maximum time step, denoted as $\Delta t = t^{n+1} - t^n$, adheres to the standard Courant–Friedrichs–Lewy (CFL) [75] criterion. This criterion is defined by the following relation

$$\Delta t = \alpha_{CFL} \min\left(\frac{h_{\min}}{c_p^{\chi}}\right). \tag{68}$$

Here, α_{CFL} represents the CFL stability number, c_p^{χ} denotes the pressure wave speed measured in referential domain and $h_{\min}$ stands for the minimum (or characteristic) length within the computational domain. The relationship between the referential pressure wave speed c_p^{χ} and the material pressure wave speed $c_p^{\boldsymbol{X}}$ is presented in expression (18). Unless specified otherwise, a value of $\alpha_{CFL} = 0.9$ has been selected in the subsequent examples to ensure a balance between accuracy and stability.

7.3.1. Plasticity

When addressing the irrecoverable elasto-plastic model presented in this paper, we employ the implicit backward Euler time integrator to advance in time the semi-discrete equations governing the plastic state variables, namely $\boldsymbol{C}_p^{-1}$ and $\bar{\varepsilon}_p$ (refer to (55)). This specific choice of time integration is in accordance with the conventional return mapping algorithm for plasticity models [4,61], ensuring numerical stability. The resulting time-discrete equations are presented below

$$\begin{aligned}
\boldsymbol{C}_p^{-1,n+1} = \boldsymbol{C}_p^{-1,n} &+ \frac{\Delta t}{\Omega_{\chi}^a}\sum_{b\in\Lambda_a}\left[\frac{1}{2}\left(\boldsymbol{C}^{-1,n}_{p,a} + \boldsymbol{C}^{-1,n}_{p,b}\right)\left(\frac{1}{J_{\boldsymbol{\Psi}}^{a,n+1}}\boldsymbol{W}_a^{n+1}\cdot\left(\boldsymbol{H}_{\boldsymbol{\Psi}}^{a,n+1}\boldsymbol{C}_{\chi}^{ab}\right)\right)\right]\\
&- 2\Delta t\dot{\gamma}_a^{n+1}\boldsymbol{F}_a^{-1,n+1}\left.\frac{\partial f}{\partial \boldsymbol{\tau}}\right|_a^{n+1}\boldsymbol{b}_e^{a,n+1}\boldsymbol{F}_a^{-T,n+1};
\end{aligned} \tag{69a}$$

$$\bar{\varepsilon}_p^{n+1} = \bar{\varepsilon}_p^{n} + \frac{\Delta t}{\Omega_{\chi}^a}\sum_{b\in\Lambda_a}\left[\frac{1}{2}\left(\bar{\varepsilon}^n_{p,a} + \bar{\varepsilon}^n_{p,b}\right)\left(\frac{1}{J_{\boldsymbol{\Psi}}^{a,n+1}}\boldsymbol{W}_a^{n+1}\cdot\left(\boldsymbol{H}_{\boldsymbol{\Psi}}^{a,n+1}\boldsymbol{C}_{\chi}^{ab}\right)\right)\right] + \Delta t\dot{\gamma}_a^{n+1}. \tag{69b}$$

To solve equations (69a) and (69b), a predictor-corrector algorithm is used. In the predictor step (Lagrangian phase), the algorithm advances explicitly without considering the ALE convective effect, yielding intermediate variables $\{\boldsymbol{C}_p^{-1,\text{int}}, \bar{\varepsilon}_p^{\text{int}}\}$. In the corrector step (remapping phase), the intermediate variables are then projected to new positions after applying the ALE material motion. Mathematically, the predictor step of the scheme over a time step Δt is defined as

$$\boldsymbol{C}_p^{-1,\text{int}} = \boldsymbol{C}_p^{-1,n} - 2\Delta t\dot{\gamma}_a^{n+1}\boldsymbol{F}_a^{-1,n+1}\left.\frac{\partial f}{\partial \boldsymbol{\tau}}\right|_a^{n+1}\boldsymbol{b}_e^{a,n+1}\boldsymbol{F}_a^{-T,n+1}; \tag{70a}$$

$$\bar{\varepsilon}_p^{\text{int}} = \bar{\varepsilon}_p^{n} + \Delta t\dot{\gamma}_a^{n+1}. \tag{70b}$$

The corrector step becomes

$$\boldsymbol{C}_p^{-1,n+1} = \boldsymbol{C}_p^{-1,\text{int}} + \frac{\Delta t}{\Omega_{\chi}^a}\sum_{b\in\Lambda_a}\left[\frac{1}{2}\left(\boldsymbol{C}^{-1,n}_{p,a} + \boldsymbol{C}^{-1,n}_{p,b}\right)\left(\frac{1}{J_{\boldsymbol{\Psi}}^{a,n+1}}\boldsymbol{W}_a^{n+1}\cdot\left(\boldsymbol{H}_{\boldsymbol{\Psi}}^{a,n+1}\boldsymbol{C}_{\chi}^{ab}\right)\right)\right]; \tag{71a}$$

$$\bar{\varepsilon}_p^{n+1} = \bar{\varepsilon}_p^{\text{int}} + \frac{\Delta t}{\Omega_{\chi}^a}\sum_{b\in\Lambda_a}\left[\frac{1}{2}\left(\bar{\varepsilon}^n_{p,a} + \bar{\varepsilon}^n_{p,b}\right)\left(\frac{1}{J_{\boldsymbol{\Psi}}^{a,n+1}}\boldsymbol{W}_a^{n+1}\cdot\left(\boldsymbol{H}_{\boldsymbol{\Psi}}^{a,n+1}\boldsymbol{C}_{\chi}^{ab}\right)\right)\right]. \tag{71b}$$

In the case of Total Lagrangian framework (that is, by setting $\boldsymbol{W} = \boldsymbol{0}$), the time update of the plasticity model exclusively relies on the predictor step (Lagrangian phase). This update for plastic variables follows the implicit Backward Euler method, a technique well-established in earlier works [4,40,51,55].

8. Algorithmic description

Algorithm 1 provides a summary of the ALE vertex-based finite volume method for nonlinear solid dynamics in irreversible processes. A key advantage of the ALE approach is its capability to effectively manage excessive element distortion through dynamic mesh movement, especially in areas experiencing significant plastic deformation. This benefit is illustrated in the example section, demonstrating its superior efficiency in comparison to traditional Lagrangian approaches.

Algorithm 1: Total ALE vertex-based finite volume algorithm.

```
Input  : initial geometry $\chi_a$ and initial states of $\boldsymbol{p}^a_\chi$, $\boldsymbol{F}^a_{\boldsymbol{\Phi}}$, $\boldsymbol{F}^a_{\boldsymbol{\Psi}}$, $J^a_{\boldsymbol{\Psi}}$, $\eta^a_\chi$, $\boldsymbol{p}^a_{\boldsymbol{W}}$, $\theta_a$ and $\boldsymbol{W}_a$ for all vertices
Output: current material geometry $\boldsymbol{\Psi}_a$, current spatial geometry $\boldsymbol{\Phi}_a$, physical velocity $\boldsymbol{v}_a$, material velocity $\boldsymbol{W}_a$, and current states of $\boldsymbol{F}_a$, $\boldsymbol{P}_a$, $\boldsymbol{C}_p^{-1,a}$, $\bar{\varepsilon}^a_p$ and $\eta^a_{\boldsymbol{X}}$

(1) INITIALISE $\boldsymbol{F}^a_{\boldsymbol{\Psi}} = \boldsymbol{C}_p^{-1,a} = \boldsymbol{I}$, $J^a_{\boldsymbol{\Psi}} = 1$, $\boldsymbol{W}_a = \boldsymbol{0}$ and $\bar{\varepsilon}^a_p = 0$
for Time $t_0$ to Time $t$ do
    (2) EVALUATE pressure and shear wave speeds: $c_p^\chi$, $c_s^\chi$
    (3) COMPUTE time increment: $\Delta t$
    for TVD-RK time integrator $= 1$ to $2$ do
        (4) COMPUTE slope of linear reconstruction procedure
        (5) EVALUATE the right-hand-side of $\frac{d}{dt}\boldsymbol{\mathcal{U}}^a_\chi$, $\frac{d}{dt}\boldsymbol{p}^a_{\boldsymbol{W}}$, $\frac{d}{dt}\boldsymbol{\Psi}_a$ and $\frac{d}{dt}\boldsymbol{\Phi}_a$
        (6) UPDATE $\boldsymbol{p}^a_\chi$, $\boldsymbol{F}^a_{\boldsymbol{\Phi}}$, $\boldsymbol{F}^a_{\boldsymbol{\Psi}}$, $J^a_{\boldsymbol{\Psi}}$, $\eta^a_\chi$, $\boldsymbol{p}^a_{\boldsymbol{W}}$, $\boldsymbol{\Psi}_a$ and $\boldsymbol{\Phi}_a$ via TVD-RK
        (7) COMPUTE intermediate variables: $\boldsymbol{F}_a = \boldsymbol{F}^a_{\boldsymbol{\Phi}}\boldsymbol{F}^{-1,a}_{\boldsymbol{\Psi}}$, $\boldsymbol{v}_a = \frac{\boldsymbol{p}^a_\chi}{J^a_{\boldsymbol{\Psi}}\rho_X}$, $\hat{\boldsymbol{v}}_a = \boldsymbol{v}_a + \boldsymbol{F}_a\boldsymbol{W}_a$, $\eta^a_{\boldsymbol{X}} = \frac{\eta^a_\chi}{J^a_{\boldsymbol{\Psi}}}$ and $\theta_a = \Theta(\boldsymbol{F}_a, \eta^a_{\boldsymbol{X}})$
        (8) ENFORCE strong boundary conditions on velocities $\{\boldsymbol{v}_a, \hat{\boldsymbol{v}}_a\}$ and entropy $\eta^a_{\boldsymbol{X}}$
        (9) EVALUATE first Piola $\boldsymbol{P}_a$ (and $\boldsymbol{C}_p^{-1,a}$ and $\bar{\varepsilon}^a_p$ if plasticity model is used)
    end
    (10) INCORPORATE entropy source related to plastic dissipation $\dot{D}_{\mathrm{Phy}}$
    (11) UPDATE internal plastic state variables $\boldsymbol{C}_p^{-1,a}$ and $\bar{\varepsilon}^a_p$ (if plasticity model is used)
    (12) EXPORT results for this time step
    (13) ADVANCE in time
end
```

In the current ALE approach, we utilise a predictor-corrector strategy, also known as a fractional-step approach [29,56], for updating the plastic variables. Within the Runge-Kutta stages, we iteratively compute the predicted expressions (70a) and (70b) for the first Piola-Kirchoff stress tensor, with the plastic variables held constant throughout the iterative process. The corrector step for expressions (71a) and (71b) is performed only outside the Runge-Kutta stage. This approach has been previously explored in the context of Total Lagrangian descriptions in our previous publications [37]. Furthermore, another possible option is to introduce the variational update of thermo-mechanical constitutive models without employing the predictor-corrector strategy, as detailed in Reference [76]. This will be further explored in our forthcoming publications.

9. Numerical examples

In this section, a number of benchmarked problems are examined in order to illustrate the performance and applicability of the proposed ALE algorithm. The aim of these examples is to demonstrate that the overall ALE algorithm

- ensures the satisfaction of the Geometric Conservation Law (GCL) condition [10,16,63,77,78], even when fictitiously moving the material mesh,
- achieves equal second order convergence for velocities/displacements, stresses/strains and also temperature/entropy (applicable in thermal-mechanical constitutive models),
- guarantees a non-negative rate of production of both numerical (i.e. Godunov-type stabilisation) and physical (e.g. plastic dissipation and irreversible heat conduction process) entropy within an isolated system, and
- displaying advantages in handling large plastic flow compared to traditional Lagrangian approaches, particularly in scenarios involving high-speed impact and fast stretching.

Table 2
Translation with heat: material properties and parameters of material mesh motion.

Young's modulus	E [MPa]	17
Material density	ρ_X [kg/m^3]	1100
Poisson's ratio	ν	0.45
Thermal conductivity	h [W.m^{-1}K^{-1}]	10
Specific heat capacity	C_v [J kg^{-1}K^{-1}]	1
Thermal expansion coefficient	α [K^{-1}]	4.95×10^{-7}
Reference temperature	θ_R [K]	293.15
Period of mesh motion	T [s]	0.5
Magnitude of mesh motion	β [ms^{-1}]	0.02

In the following plasticity examples, we address material mesh motion by solving the conservation-type equation, as expressed in (33). However, in the context of thermo-elastic problems, this approach tends to results in minimal mesh movement. To achieve more substantial mesh movement in these cases, we instead prescribe a sinusoidal-type material mesh motion. This expression, specifically designed for a cuboid, is detailed in Reference [26] and is presented here for completeness

$$\boldsymbol{\Psi}(\chi,t) = \chi + \begin{bmatrix} \beta \sin^2\left(\frac{\pi t}{T}\right) \sin\left(\frac{\widetilde{\chi}_1}{2\pi L}\right)\left[\cos\left(\frac{\widetilde{\chi}_2}{2\pi H}\right) + \sin\left(\frac{\widetilde{\chi}_2}{2\pi H}\right)\right] \\ \beta \frac{H}{L} \sin^2\left(\frac{\pi t}{2T}\right) \sin\left(\frac{\widetilde{\chi}_2}{2\pi H}\right)\left[\cos\left(\frac{\widetilde{\chi}_1}{2\pi L}\right) + \sin\left(\frac{\widetilde{\chi}_1}{2\pi L}\right)\right] \\ 0 \end{bmatrix}, \tag{72}$$

where $\widetilde{\chi}_1 = \chi_1 + \chi_1^C$ and $\widetilde{\chi}_2 = \chi_2 + \chi_2^C$ represent the coordinates shifted with respect to the centroid of the domain χ^C. The parameter β determines the magnitude of the mesh motion and T denotes the period of the sinusoidal functions. Employing this sinusoidal mesh motion approach enables more pronounced and controlled movement in the material mesh. This is particularly beneficial for examining the robustness of the ALE algorithm in thermo-elastic scenarios, as it allows for an assessment of the performance of the algorithm under varying degrees of mesh deformation. Differentiating expression (72) in time gives the material mesh velocity $\boldsymbol{W}$ expressed as

$$\boldsymbol{W}(\chi,t) = \begin{bmatrix} 2\beta \frac{\pi}{T} \sin\left(\frac{\pi t}{T}\right)\cos\left(\frac{\pi t}{T}\right) \sin\left(\frac{\widetilde{\chi}_1}{2\pi L}\right)\left[\cos\left(\frac{\widetilde{\chi}_2}{2\pi H}\right) + \sin\left(\frac{\widetilde{\chi}_2}{2\pi H}\right)\right] \\ \beta \frac{H}{L}\frac{\pi}{T} \sin\left(\frac{\pi t}{2T}\right)\cos\left(\frac{\pi t}{2T}\right) \sin\left(\frac{\widetilde{\chi}_2}{2\pi H}\right)\left[\cos\left(\frac{\widetilde{\chi}_1}{2\pi L}\right) + \sin\left(\frac{\widetilde{\chi}_1}{2\pi L}\right)\right] \\ 0 \end{bmatrix}. \tag{73}$$

Both material mesh motion (72) and material mesh velocity (73) are carefully designed to only allow movement tangentially on the material boundary surface in order to avoid changes in physical volume.

To analyse large thermo-elastic deformations, a Mie-Gruneisen thermo-elastic is employed. The corresponding internal energy density $\mathcal{E}$ as a function of deformation gradient $\boldsymbol{F}$ and entropy density $\eta_{\boldsymbol{X}}$ (per unit of material volume) is given by

$$\mathcal{E}(\boldsymbol{F},\eta_{\boldsymbol{X}}) = \tilde{\mathcal{E}}_{\boldsymbol{X}}(\boldsymbol{F}) + c_v\theta_R\left(e^{\frac{\eta_{\boldsymbol{X}} - \tilde{\eta}_{\boldsymbol{X}}(J)}{c_V} - 1}\right). \tag{74}$$

In this work, the internal energy density at reference temperature is formulated as

$$\tilde{\mathcal{E}}_{\boldsymbol{X}}(\boldsymbol{F}) = \tilde{\mathcal{E}}'_{\boldsymbol{X}}(J^{-1/3}\boldsymbol{F}) + U(J). \tag{75}$$

Both the deviatoric $\tilde{\mathcal{E}}'_{\boldsymbol{X}}(J^{-1/3}\boldsymbol{F})$ and the volumetric $U(J)$ contributions are

$$\tilde{\mathcal{E}}'_{\boldsymbol{X}}(J^{-1/3}\boldsymbol{F}) = \frac{1}{2}\mu\left[J^{-2/3}(\boldsymbol{F}:\boldsymbol{F}) - 3\right]; \qquad U(J) = \frac{1}{2}\kappa(J-1)^2 + c_v\Gamma_0\theta_R(J-1), \tag{76}$$

where μ and κ are the shear modulus and bulk modulus and Γ_0 is a positive material constant. In addition, we also incorporate a simple volumetric-based Mie-Grüneisen model [43,57] described by [43]

$$\tilde{\eta}_{\boldsymbol{X}}(J) = c_v\Gamma_0\left(\frac{J^q - 1}{q}\right), \tag{77}$$

where q is a dimensionless parameter varying from zero (i.e. a perfect gas) to one (i.e. solid materials). Previous work [30] has demonstrated the polyconvexity (and thus, rank-one convexity) of this coupled model.

9.1. Satisfaction of geometric conservation laws: patch test

This example involves a patch test that illustrates the performance of the proposed ALE algorithm in rigid body motion, an example similar to that described in [26]. A column of unit 1 m squared cross section and of length $H = 6$ m is initially prescribed by

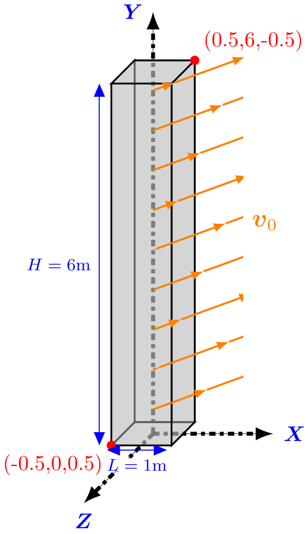

Fig. 3. Problem setup for the translation test case: geometry and its dimension.

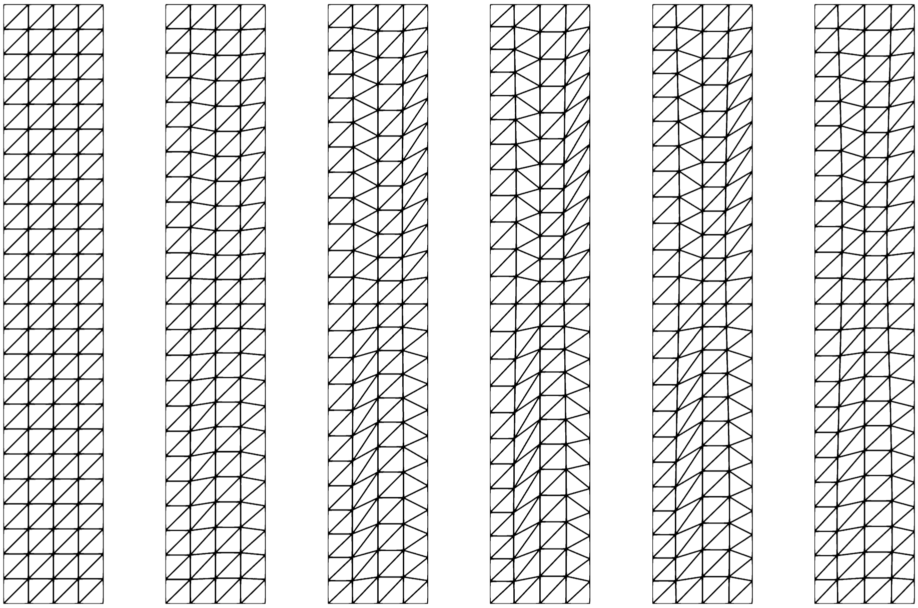

Fig. 4. Translation: Time evolution of the prescribed mesh motion at times $t = \{0, 40, 80, 120, 160, 200\}$ ms (from left to right).

a uniform velocity field $\boldsymbol{v}_0 = [3, 1, 0]^T$ ms^{-1} across the entire domain. All the boundaries of the structure are left free. See Fig. 3 for the problem setup. The primary objective of this example is to assess the capability of the algorithm in reliably capturing rigid body translation behaviour by arbitrarily moving the mesh, while still adhering to the so-called discrete Geometric Conservation Law (GCL) conditions. Additionally, a Mie-Grüneisen model is incorporated to account for the effects of thermal variations. The corresponding material properties and the mesh motion parameters are presented in Table 2. It is interesting to show graphically how the mesh moves in time according to the expression described in (73). This is displayed in Fig. 4.

Given that the column undergoes rigid body translation, it is expected to move through space in the direction of the initial velocity, maintaining both a constant speed and uniform temperature distribution. For qualitative evaluation, Fig. 5 illustrates the temporal evolution of global errors. These errors include the deviation of the current temperature θ from the reference temperature θ_R, and the differences between the current and initial velocity components. As expected, when employing the complete ALE algorithm as presented in (54), these errors fluctuate around machine precision levels. Conversely, a simplified model that excludes the solution for $J_{\boldsymbol{\Psi}}$ results in significantly larger errors, failing to meet the discrete GCL conditions associated with the volumetric strain. This discrepancy is visually evident in Fig. 6. For instance, the reduced model exhibits non-smooth contour profile, whereas smooth

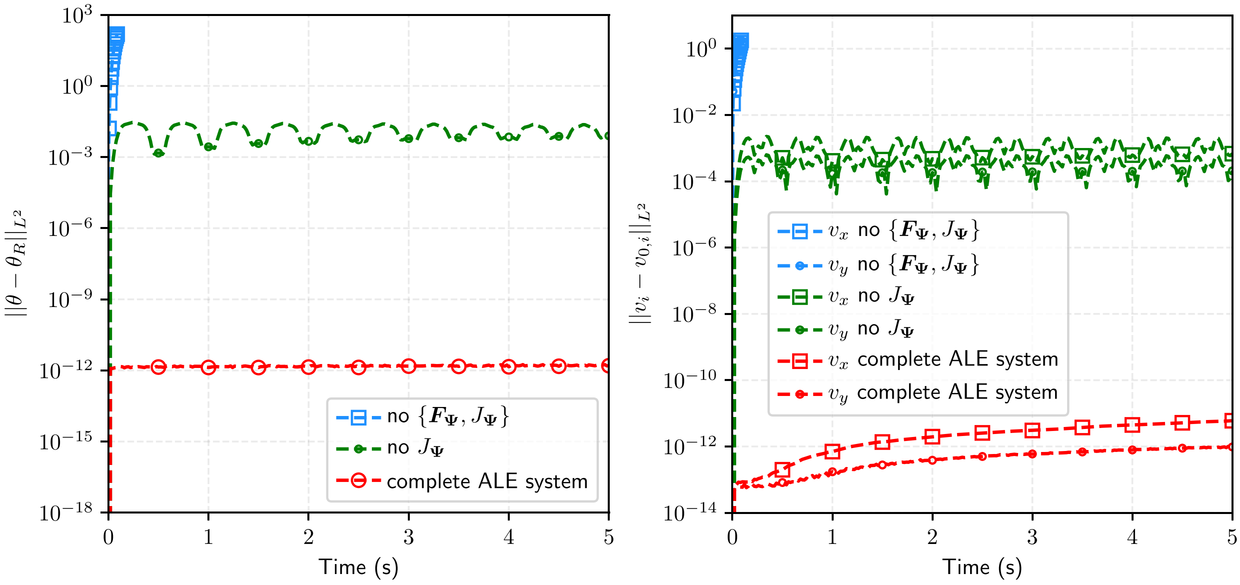

(a)   (b)

Fig. 5. Translation: time evolution of the L^2 global errors in (a) $||\theta-\theta_R||_{L^2}$ and (b) $||v_i-v_{0,i}||_{L^2}$ (with $i=x,y$) when using (red) the complete ALE system, (green) the system without solving $J_{\boldsymbol{\Phi}}$ and (blue) the further reduced system without solving $\{\boldsymbol{F}_{\boldsymbol{\Phi}}, J_{\boldsymbol{\Psi}}\}$. A discretisation of $4\times 24\times 4$ linear tetrahedral elements. A Mie-Grüneisen equation of state is used with parameters listed in Table 2. (For interpretation of the colours in the figure(s), the reader is referred to the web version of this article.)

Table 3
Swinging cube: material properties and parameters of material mesh motion.

Young's modulus	E [MPa]	17
Material density	ρ_X [kg/m^3]	1100
Poisson's ratio	ν	0.45
Thermal conductivity	h [W/m^{-1}K^{-1}]	10
Specific heat capacity	C_v [J kg^{-1}K^{-1}]	1
Thermal expansion coefficient	α [K^{-1}]	4.95×10^{-7}
Reference temperature	θ_R [K]	293.15
Magnitude	U_0 [m]	5×10^{-4}
Lame first parameter	λ [MPa]	9.8077
Lame shear modulus	μ [MPa]	6.5385
Mie-Grüneisen coefficient		8.5889
Period of mesh motion	T [s]	1×10^{-3}
Magnitude of mesh motion	β [ms^{-1}]	1×10^{-4}

contours are obtained with the complete ALE system. Furthermore, an even more simplified model that disregard both $\boldsymbol{F}_{\boldsymbol{\Psi}}$ and $J_{\boldsymbol{\Psi}}$ solutions unreliably tracks the deformation trajectory and eventually leads to the breakdown of the numerical algorithm.

9.2. Mesh convergence: low dispersion swinging cube

As previously investigated in References [30,37], a cubic domain with unit length sides is used for analysis. The objective of this example is to examine the order of convergence of the proposed ALE framework. The physical mapping and the temperature fields are specifically chosen as

$$\varphi^{\text{ex}}(\boldsymbol{X},t)=\boldsymbol{X}+U_0\cos\left(\frac{\sqrt{3}}{2}c_d t\right)\begin{bmatrix} A\sin(\frac{\pi X_1}{2})\cos(\frac{\pi X_2}{2})\cos(\frac{\pi X_3}{2})\\ B\cos(\frac{\pi X_1}{2})\sin(\frac{\pi X_2}{2})\cos(\frac{\pi X_3}{2})\\ C\cos(\frac{\pi X_1}{2})\cos(\frac{\pi X_2}{2})\sin(\frac{\pi X_3}{2})\end{bmatrix};\; c_d=\sqrt{\frac{2\mu+\lambda}{\rho_X}+\frac{\theta_R\Gamma_0^2 c_v}{\rho_X}}, \tag{78}$$

where the parameters $A=B=C=1$. When the value of U_0 is below 0.0001 m, the solution is considered linear. Consequently, the exact velocity field $\boldsymbol{v}$, deformation gradient tensor $\boldsymbol{F}$ and temperature field θ can be computed as

$$\boldsymbol{v}^{\text{ex}}(\boldsymbol{X},t)=\frac{\partial\varphi^{\text{ex}}(\boldsymbol{X},t)}{\partial t};\qquad \boldsymbol{F}^{\text{ex}}(\boldsymbol{X},t)=\boldsymbol{I}+\frac{\partial\varphi^{\text{ex}}(\boldsymbol{X},t)}{\partial\boldsymbol{X}} \tag{79}$$

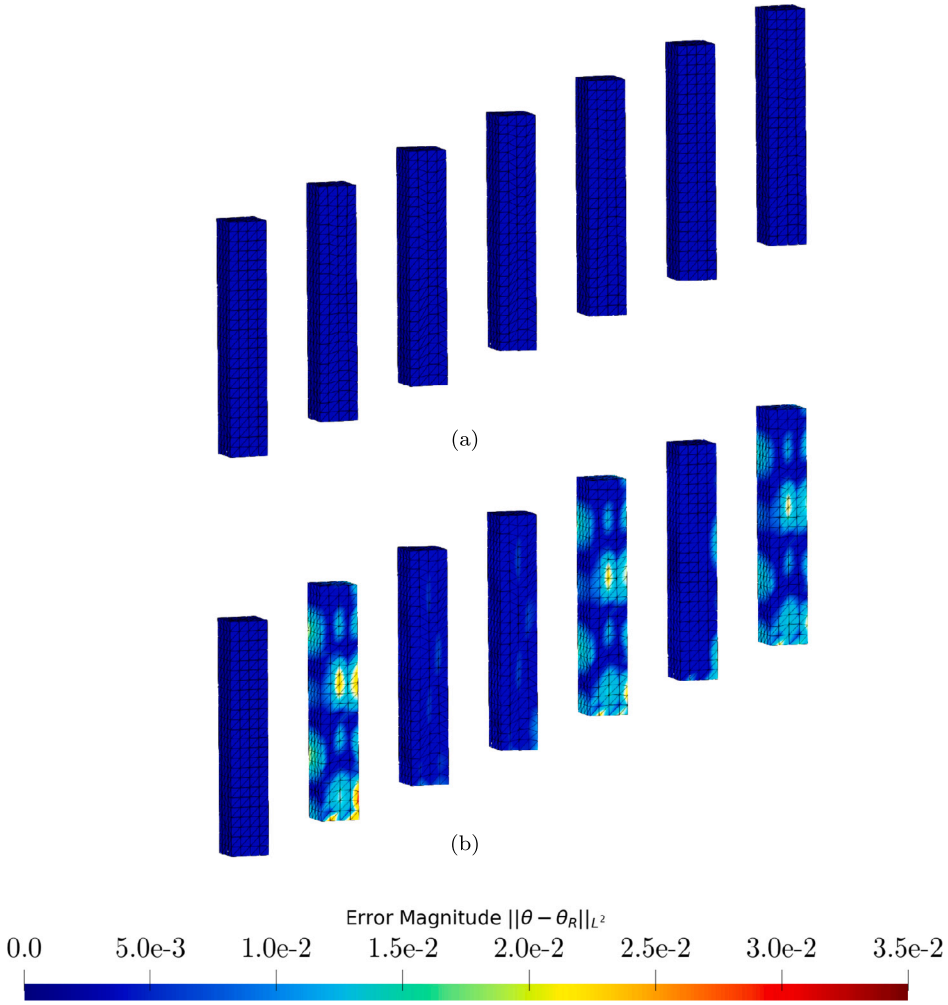

Fig. 6. Translation: a sequence of deformed states at times $t = \{0, 0.8, \ldots, 4.8\}$ s (from left to right for each row) when using (a) the complete ALE system and (b) the reduced system without solving $J_{\boldsymbol{\Psi}}$. Colour contour indicates the error in $||\theta - \theta_R||_{L^2}$. A discretisation of $4 \times 24 \times 4$ liner tetrahedral elements. A Mie-Grüneisen equation of state is used with parameters listed in Table 2.

Table 4
Swinging cube: numerical values for the L^1 norm error of the velocity components v_x, v_y, v_z, the temperature θ and the diagonal components of the first Piola Kirchhoff stress P_{xX}, P_{yY}, P_{zZ}. Convergence rates are calculated using the results of the two finest meshes. A Mie-Grüneisen model is used with parameters summarised in Table 3.

L^1 error	v_x	v_y	v_z	θ
1/6	3.184×10^{-2}	3.171×10^{-2}	3.053×10^{-2}	8.211×10^{-5}
1/12	7.692×10^{-3}	7.851×10^{-3}	7.550×10^{-3}	2.134×10^{-5}
1/24	1.886×10^{-3}	1.916×10^{-3}	1.863×10^{-3}	5.276×10^{-6}
1/48	4.492×10^{-4}	4.491×10^{-4}	4.487×10^{-4}	1.197×10^{-6}
conv. rate	2.070	2.093	2.054	2.141

L^1 error	P_{xX}	P_{yY}	P_{zZ}
1/6	1.861×10^{-2}	1.861×10^{-2}	1.860×10^{-2}
1/12	4.847×10^{-3}	4.847×10^{-3}	4.845×10^{-3}
1/24	1.206×10^{-3}	1.207×10^{-3}	1.206×10^{-3}
1/48	2.817×10^{-4}	2.817×10^{-4}	2.816×10^{-4}
conv. rate	2.098	2.098	2.098

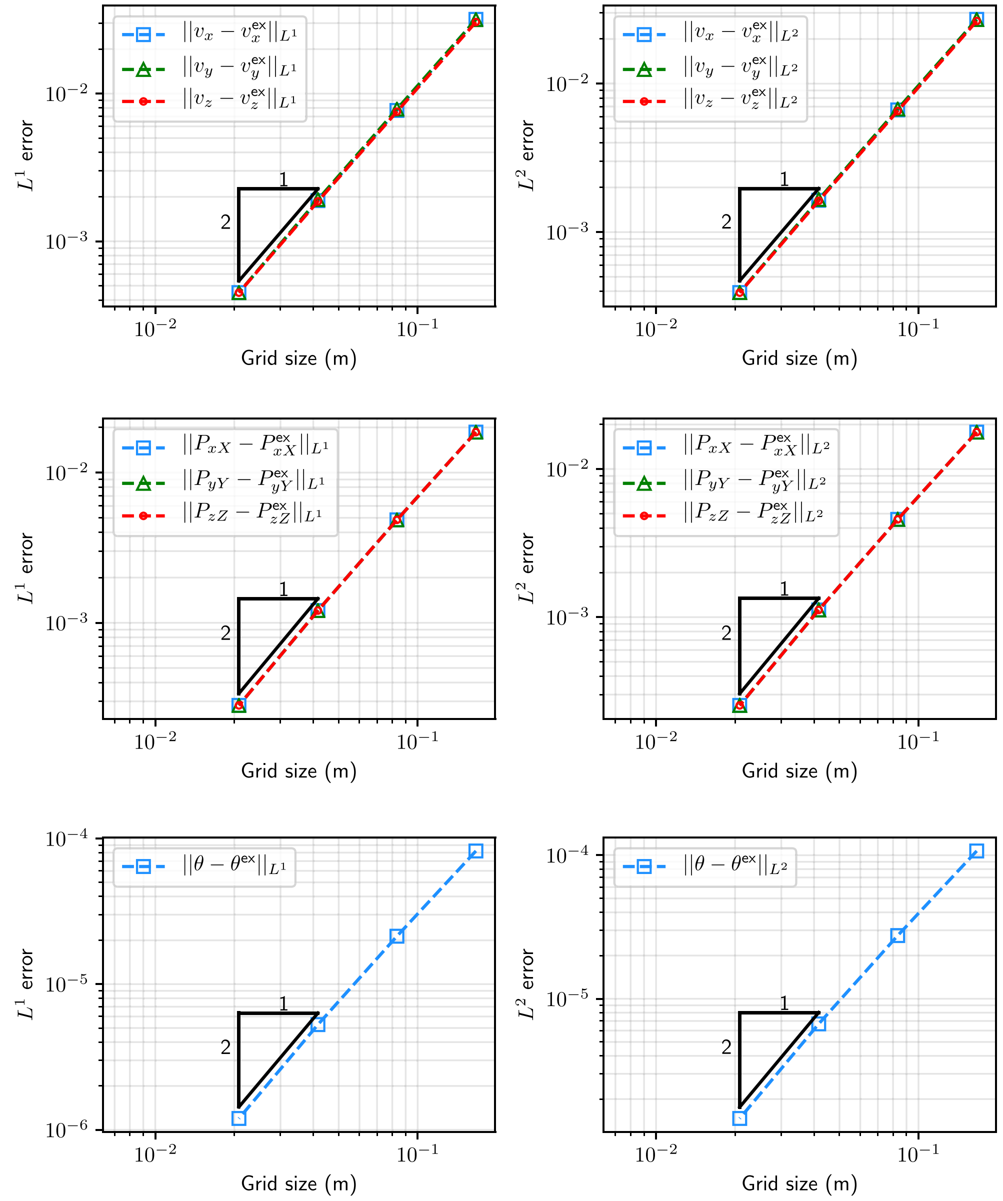

Fig. 7. Swinging cube: L^1 and L^2 global convergence analysis at time $t = 1 \times 10^{-3}$ s for (first row) the components of velocity, (second row) the components of the first Piola Kirchhoff stress tensor and (third row) the temperature field. Results obtained using a Mie-Grüneisen model and the material properties used are summarised in Table 3.

and

$$\theta^{\text{ex}} = \theta_R \left(1 - \frac{3\pi}{2} U_0 \cos(c_d \pi t) \cos\left(\frac{\pi X_1}{2}\right) \cos\left(\frac{\pi X_2}{2}\right) \cos\left(\frac{\pi X_3}{2}\right)\right). \tag{80}$$

Dirichlet boundary conditions compatible with equation (78) are applied on the boundary of the domain. In particular, the cube features symmetry boundary conditions on the faces $X_1 = 0, X_2 = 0$ and $X_3 = 0$ and skew-symmetric boundary conditions on the faces $X_1 = 1, X_2 = 1$ and $X_3 = 1$. The parameters used in this simulation are summarised in Table 3.

Fig. 7 illustrate the L^1 and L^2 norm convergence analysis conducted at time $t = 1 \times 10^{-3}$ s. These analyses comprise the velocity components $\boldsymbol{v}$, the components of the first Piola Kirchhoff stress tensor $\boldsymbol{P}$ and the temperature field θ. Consistent with expectations, the proposed algorithm demonstrates second-order convergence in space and time for all the solved variables. This equal convergence rate for all variables, especially in the accurate representation of stresses/strains and temperature/entropy, marks a substantial

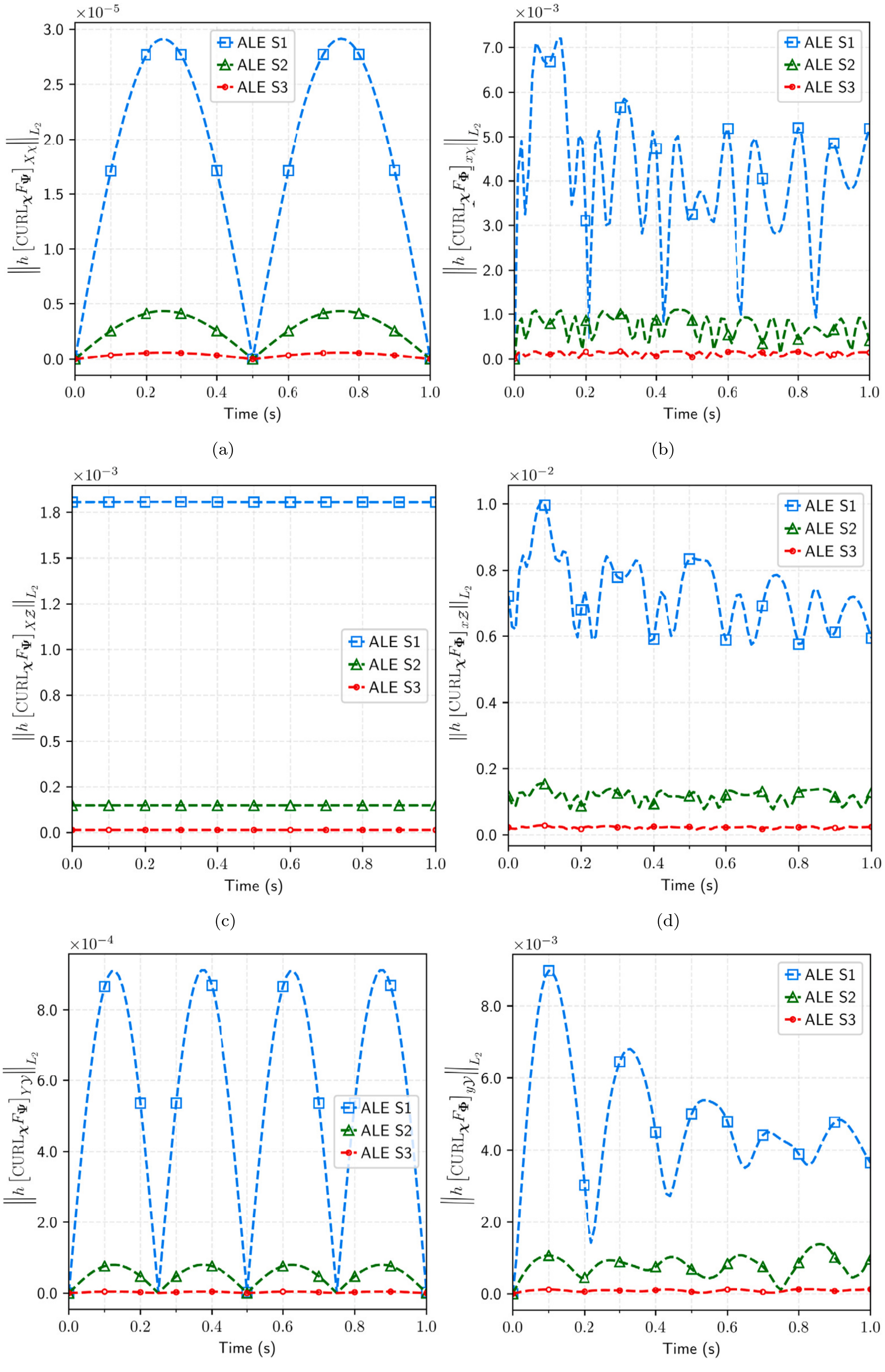

Fig. 8. Twisting column: time evolution of the components of the L_2 norm of curl-free errors: (a) $\|h\,[\mathrm{CURL}_\chi \boldsymbol{F}_{\boldsymbol{\Psi}}]_{X\chi}\|_{L_2}$, (b) $\|h\,[\mathrm{CURL}_\chi \boldsymbol{F}_{\boldsymbol{\Phi}}]_{x\chi}\|_{L_2}$, (c) $\|h\,[\mathrm{CURL}_\chi \boldsymbol{F}_{\boldsymbol{\Psi}}]_{X\mathcal{Z}}\|_{L_2}$, (d) $\|h\,[\mathrm{CURL}_\chi \boldsymbol{F}_{\boldsymbol{\Phi}}]_{x\mathcal{Z}}\|_{L_2}$, (e) $\|h\,[\mathrm{CURL}_\chi \boldsymbol{F}_{\boldsymbol{\Psi}}]_{Y\mathcal{Y}}\|_{L_2}$, and (f) $\|h\,[\mathrm{CURL}_\chi \boldsymbol{F}_{\boldsymbol{\Phi}}]_{y\mathcal{Y}}\|_{L_2}$. Notice that h represents the characteristic length of each control volume. ALE results are obtained using three different meshes. An isothermal neo-Hookean model is used. Parameters related to material properties and the mesh motion are summarised in Table 6.

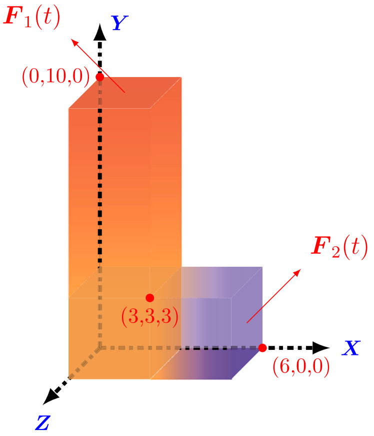

Fig. 9. Problem setup for L-shaped block: geometry and its dimension.

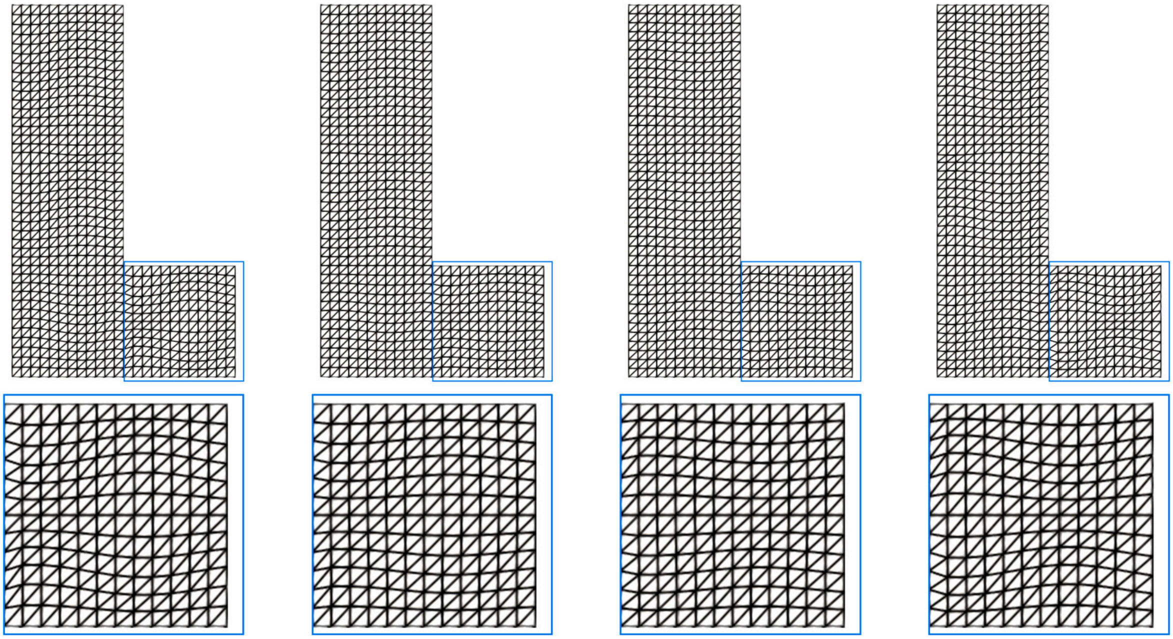

Fig. 10. L-shaped block: for visualisation purposes, we display the two-dimensional view of a series of material mesh deformation described in (73) at time $t = 0.1$ s, … 0.4 s (from left to right).

enhancement over the classical ALE framework [21].[1] In the interest of completeness, results for both norm errors are detailed in Tables 4 and 5.

9.3. Assessment of curl-free involution modes

This example was previously investigated in Reference [26]. The column, with a unit square cross-section and a length of $L = 6$ m, is twisted with an initial sinusoidal velocity field relative to the origin, given by

$$\boldsymbol{v}_0 = \begin{bmatrix} 0 \\ \Omega_0 \sin\left(\frac{\pi Y}{2L}\right) \\ 0 \end{bmatrix} \text{m/s}, \tag{81}$$

where $\Omega_0 = 105$ rad s^{-1} represents the magnitude of initial angular velocity. The isothermal neo-Hookean hyperelastic model is used. Material properties and mesh motion parameters are presented in Table 6. The main objective of this example is to illustrate the

---

[1] Typically, a reduced order of convergence is observed for the derived variables, such as stresses and strains.

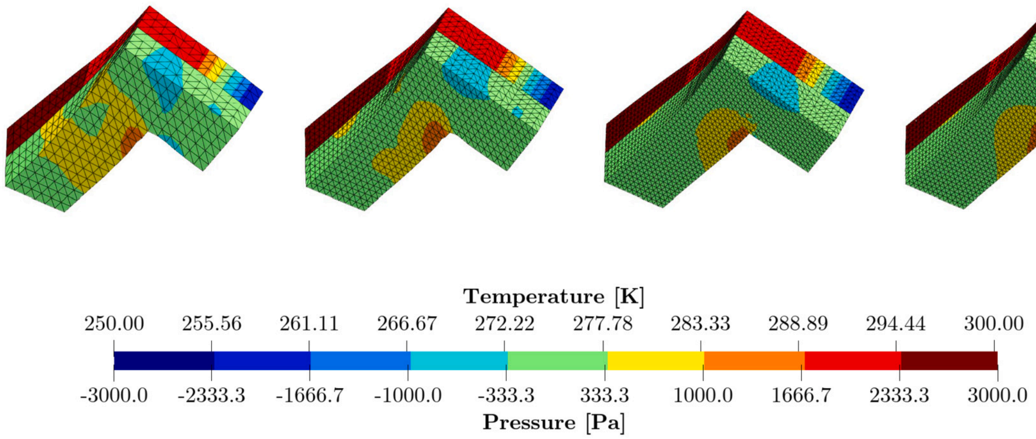

Fig. 11. L-shaped block: comparison of deformed shapes at time $t = 23$ s. The first three columns (left to right) show the mesh refinement of a structure simulated using the proposed ALE algorithm, whereas the last column (on the right) shows results via an alternative in-house Total Lagrangian vertex-based finite volume algorithm [41]. Colour indicates the pressure and temperature profiles. The Mie-Grüneisen model is used. The parameters related to material properties and mesh motion are summarised in Table 7.

Table 5
Swinging cube: numerical values for the L^2 norm error of the velocity components v_x, v_y, v_z, the temperature θ and the diagonal components of the first Piola Kirchhoff stress P_{xX}, P_{yY}, P_{zZ}. Convergence rates are calculated using the results of the two finest meshes. A Mie-Grüneisen model is used with parameters summarised in Table 3.

L^2 error	v_x	v_y	v_z	θ
1/6	2.711×10^{-2}	2.704×10^{-2}	2.640×10^{-2}	1.071×10^{-4}
1/12	6.654×10^{-3}	6.746×10^{-3}	6.544×10^{-3}	2.755×10^{-5}
1/24	1.638×10^{-3}	1.660×10^{-3}	1.625×10^{-3}	6.683×10^{-6}
1/48	3.917×10^{-4}	3.916×10^{-4}	3.909×10^{-4}	1.465×10^{-6}
conv. rate	2.064	2.084	2.056	2.189

L^2 error	P_{xX}	P_{yY}	P_{zZ}
1/6	1.777×10^{-2}	1.777×10^{-2}	1.776×10^{-2}
1/12	4.574×10^{-3}	4.574×10^{-3}	4.574×10^{-3}
1/24	1.119×10^{-3}	1.119×10^{-3}	1.119×10^{-3}
1/48	2.536×10^{-4}	2.536×10^{-4}	2.536×10^{-4}
conv. rate	2.141	2.141	2.141

Table 6
Twisting column: material properties and parameters of the mesh motion.

Young's modulus	E [MPa]	17
density	ρ_R [kg/m^3]	1100
Poisson's ratio	ν	0.45
Thermal conductivity	h [W/m^{-1}K^{-1}]	0
Specific heat capacity	C_v [J kg^{-1}K^{-1}]	1
Thermal expansion coefficient	α [K^{-1}]	0
Reference temperature	θ_R [K]	293.15
Period of mesh motion	T [s]	1
Magnitude of mesh motion	β [m/s]	1×10^{-2}

performance of the proposed algorithm in controlling the accumulation of curl-free errors, thereby preventing the breakdown of the numerical algorithm over long-term response. Since the central difference approximation is used to approximate both the material and spatial velocity gradient fields, it is expected that the tangential jump of both deformation gradient tensors across the interface are continuous. Fig. 8 demonstrates the time evolution of the components of the L_2 norm of curl-free errors. It is observed that the involution errors are bounded throughout the entire simulation and, more importantly, the time-accumulated errors are reduced through mesh refinement.

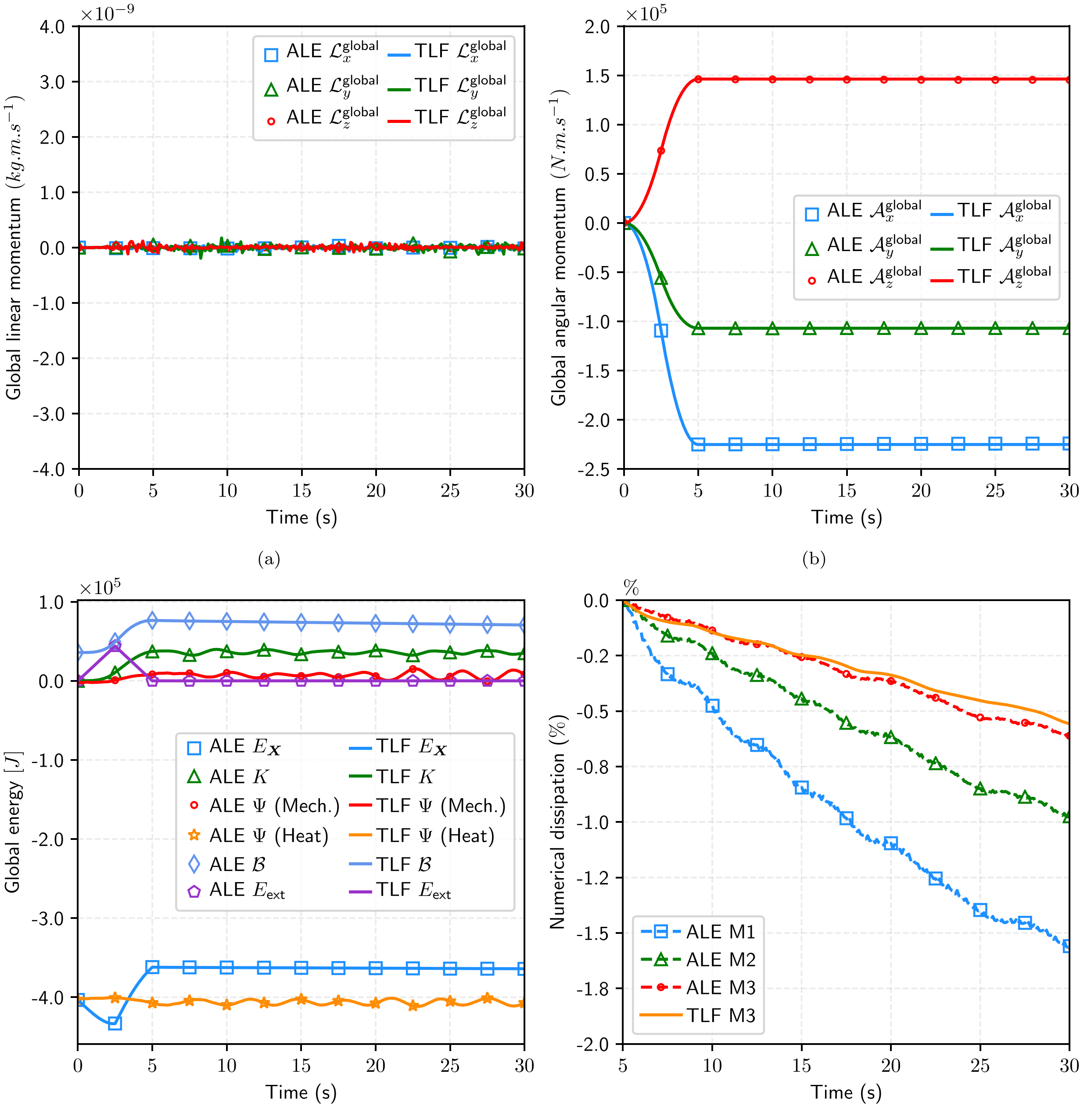

(a)　(b)　(c)　(d)

Fig. 12. L-shaped block: time evolution of (a) global linear momentum, (b) global angular momentum, (c) different energy measures and (d) total numerical dissipation (%) introduced in the algorithm. A Mie-Grüneisen model is used. Parameters related to the material properties and the mesh motion are tabulated in Table 7.

9.4. *Conservation properties and the discrete satisfaction of second law: L-shaped block*

In this thermo-elastic example, an L-shaped block is subjected to a pair of time-varying boundary forces applied to two of its boundary faces, as depicted in Fig. 9. The boundary forces are described by the expression given below

$$\boldsymbol{F}_1(t) = -\boldsymbol{F}_2(t) = \begin{bmatrix} 150 \\ 300 \\ 450 \end{bmatrix} f(t), \qquad f(t) = \begin{cases} t & \text{if } 0 \le t < 2.5 \\ t-5 & \text{if } 2.5 \le t < t \\ 0 & \text{else} \end{cases}. \tag{82}$$

The initial temperature distribution is defined by the following expression

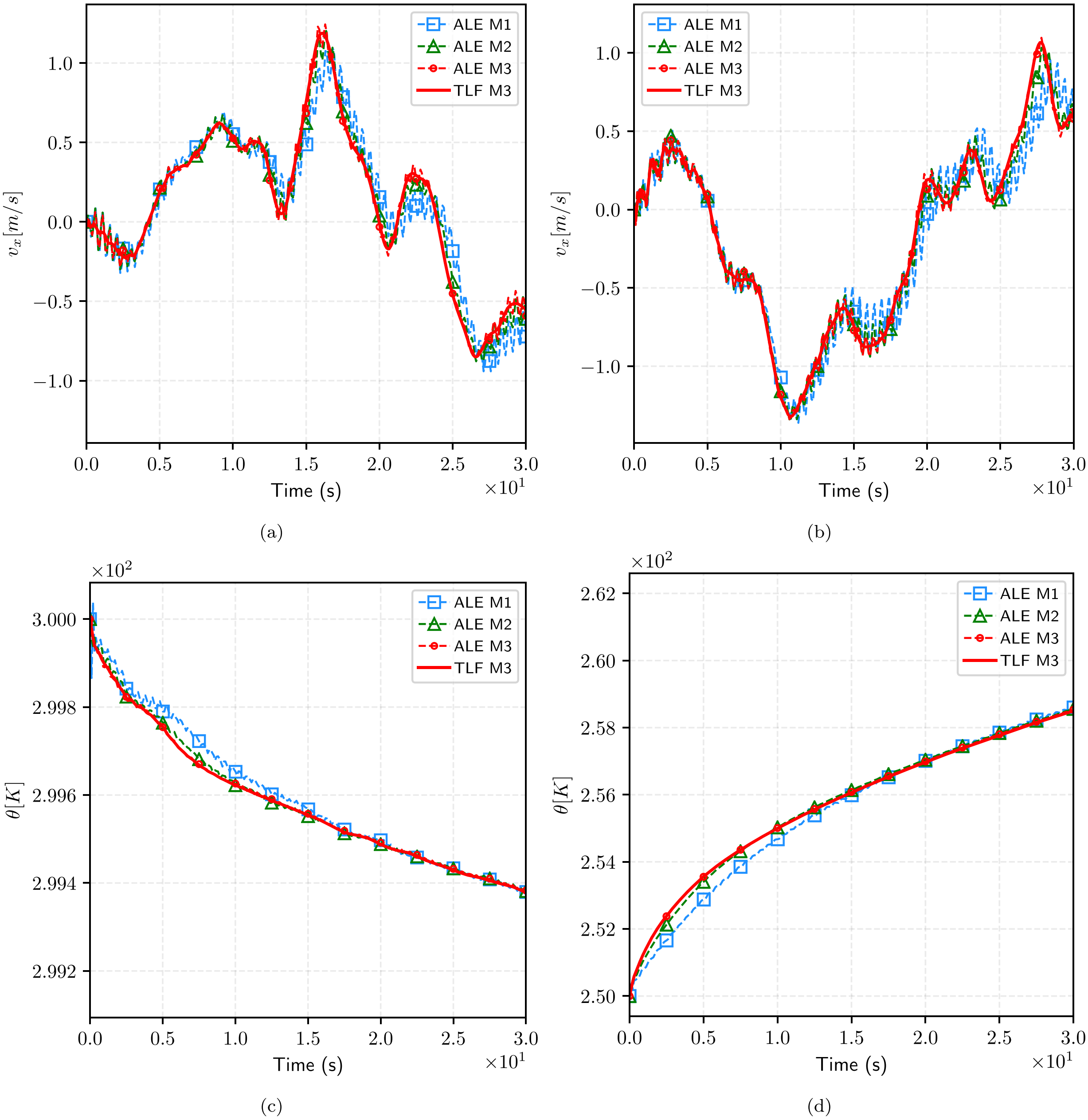

Fig. 13. L-shaped block: time evolution of the velocity components at (a) position $\boldsymbol{X} = (0, 10, 0)^T$ and (b) at position $\boldsymbol{X} = (6, 0, 0)^T$, and temperature at (c) position $\boldsymbol{X} = (0, 10, 0)^T$ and (d) at position $\boldsymbol{X} = (6, 0, 0)^T$. ALE results are obtained using three different meshes (namely **M1**, **M2** and **M3**), comparing against alternative Total Lagrangian vertex-based finite volume algorithm [41]. A Mie-Grüneisen model is used. Parameters related to material properties and the mesh motion are summarised in Table 7.

$$\theta(\boldsymbol{X}, t = 0) = \begin{cases} -(43.15/3)X + 336.3 & \text{if } 3 < X \leq 6 \\ (6.85/7)Y + 290.21 & \text{if } 3 < Y \leq 10. \end{cases} \tag{83}$$

The primary aim of this study is to assess the capability of the ALE algorithm in (1) preserving both linear and angular momenta and (2) ensuring adherence with the second law of thermodynamics by monitoring the total numerical dissipation introduced by the Godunov-type algorithm. A similar numerical example, but in an isothermal context, was previously reported in [26]. Simulation parameters employed in this example are detailed in Table 7. To analyse mesh convergence, three different levels of mesh refinement are employed. For instance, $\{\mathbf{M1}, \mathbf{M2}, \mathbf{M3}\}$ comprise $\{5616, 18954, 44928\}$ linear tetrahedral elements, respectively. To facilitate varying degrees of mesh movement, we prescribe the mapping function described in expression (73). A series of mesh movement snapshots are shown graphically in Fig. 10.

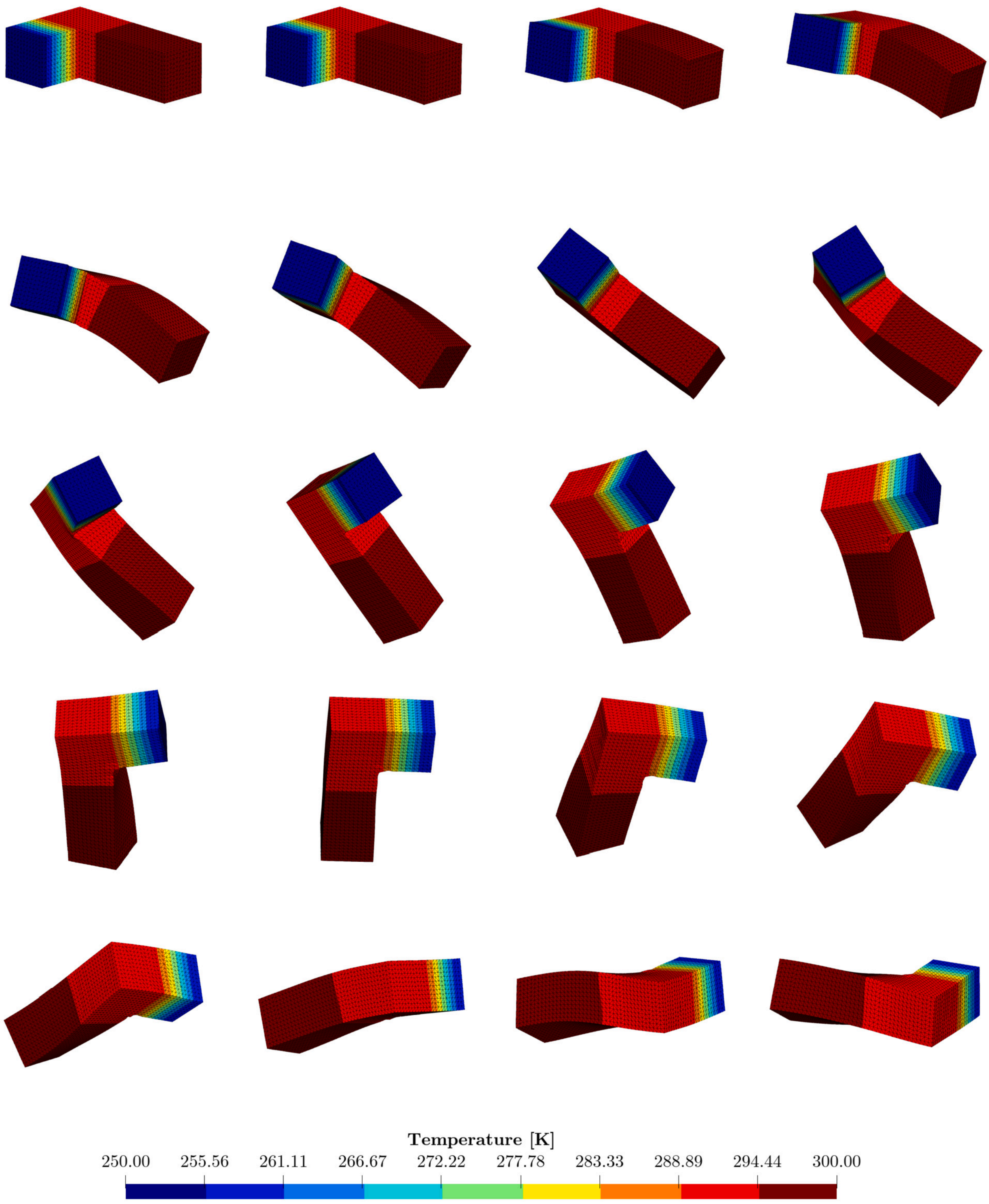

Fig. 14. L-shaped block: a sequence of deformed structures with temperature distribution at times $t = 0, 1, 2, ..., 19$ s (from left to right and top to bottom), respectively. Results obtained using a Mie-Grüneisen model with **M3** mesh. Parameters related to material properties and the mesh motion are summarised in Table 7.

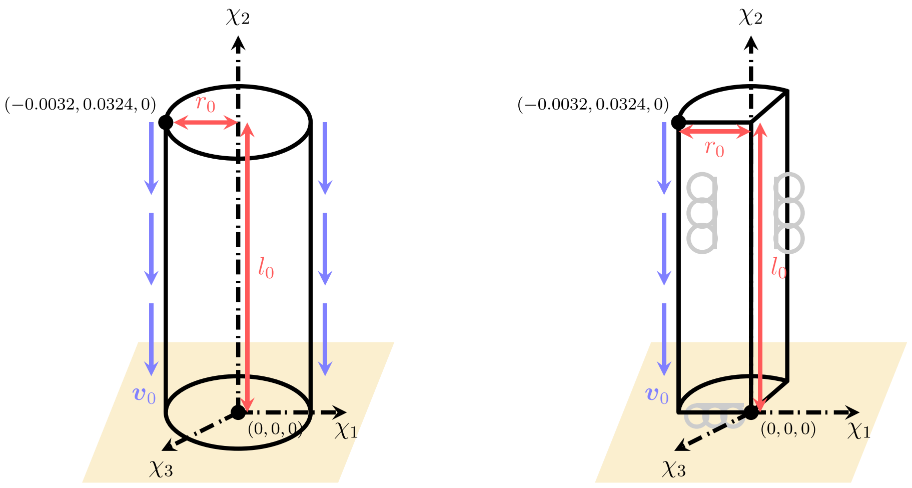

(a) Setup of the problem. (b) Quarter of the domain.

Fig. 15. Problem setup for Taylor impact bar: geometry and its dimension.

Table 7
L-shaped block: material properties and parameters of material mesh motion.

Young's modulus	E [kPa]	50.05
Material density	ρ_X [kg/m^3]	1000
Poisson's ratio	ν	0.3
Thermal conductivity	h [W/m^{-1}K^{-1}]	10
Specific heat capacity	C_v [J kg^{-1}K^{-1}]	1
Thermal expansion coefficient	α [K^{-1}]	2.223×10^{-4}
Reference temperature	θ_R [K]	293.15
Period of mesh motion	T [s]	1
Magnitude of mesh motion	β [ms^{-1}]	2×10^{-2}

First, a mesh refinement study is carried out, as illustrated in the first three columns (from left to right) of Fig. 11. The deformation pattern, as well as the pressure and temperature profiles, simulated using a relatively coarse mesh (**M1**) shows good agreement with those results obtained using finer meshes (**M2** and **M3** models). For benchmarking purposes, results from an in-house Total Lagrangian vertex centred Godunov-type finite volume algorithm [41], using the **M3** discretisation, are also included for comparison. The proposed ALE algorithm demonstrates near-identical results to those of the Total Lagrangian counterpart, as evidenced in Fig. 11.

Second, the capability of the proposed algorithm to ensure the conservation of global linear and angular momenta is depicted in Figs. 12a and 12b. The global linear momentum, $\boldsymbol{\mathcal{L}} = \int_{\Omega_\chi} \boldsymbol{p}_\chi \, d\Omega_\chi$, is expected to oscillate around zero value (within machine error) at all times. The global angular momentum, $\boldsymbol{\mathcal{A}} = \int_{\Omega_\chi} \boldsymbol{x} \times \boldsymbol{p}_\chi \, d\Omega_\chi$, is not exactly preserved, but it experiences a very minimal reduction after the loading phase $t > 5$ s. Additionally, Fig. 12c presents the evolution of various energy measures, including kinetic energy $\mathcal{K} = \int_{\Omega_\chi} \frac{1}{2\rho_\chi} \boldsymbol{p}_\chi \cdot \boldsymbol{p}_\chi \, d\Omega_\chi$, internal energy associated with mechanical contribution $\mathcal{E}_{\text{mech}} = \int_{\Omega_\chi} J_{\boldsymbol{\Psi}} \tilde{\mathcal{E}}_{\boldsymbol{X}} \, d\Omega_\chi$, internal energy associated with thermal effects $\mathcal{E}_{\text{ther}} = \int_{\Omega_\chi} J_{\boldsymbol{\Psi}} c_v \theta_R \left(e^{\frac{\eta - \tilde{\eta}_{\boldsymbol{X}}}{c_v}} - 1 \right) d\Omega_\chi$, and external power $\dot{\Pi}_{\text{ext}} = \int_{\partial\Omega_\chi} \boldsymbol{t}_B \cdot \boldsymbol{v}_B \, dA_\chi$. These facilitate the computation of the total energy $E = \mathcal{K} + \mathcal{E}_{\text{mech}} + \mathcal{E}_{\text{ther}} - \Pi_{\text{ext}}$, leading to an alternative measure known as *Ballistic* energy, that is $\mathcal{B} = E - \theta_R \eta$ (with $\eta = \int_{\Omega_\chi} \eta_\chi d\Omega_\chi$). A slight decrease in total and *Ballistic* energies after the loading phase is noted, which must be attributed to the incorporation of Godunov-type numerical dissipation and irreversible heat dissipation in the system.

Third, Fig. 13 monitors the time evolution of the velocity component v_x and the temperature at two positions, namely $\boldsymbol{X} = (0, 10, 0)^T$ and $\boldsymbol{X} = (6, 0, 0)^T$. The solution demonstrates convergence with successive levels of refinement. Finally, Fig. 14 depicts a sequence of deformed states, with the colour contour indicating temperature profile. Stable solutions are observed, highlighting the robustness of the algorithm for long-term responses.

9.5. *Robustness in high-speed impact problem*

This example presents a benchmark problem in which a copper bar, initially measuring $L = 0.0324$ m in length and $r = 0.0032$ m in radius, impacts against a rigid wall with a velocity of 227 m/s. The geometry of the problem is depicted in Fig. 15. In this context, a Hencky-based von Mises material with rate-independent linear hardening law is first employed. The parameters of this material model used in the simulation are included in Table 8. For computational efficiency, the simulation of the bar impact considers only a quarter of the domain by applying appropriate symmetry boundary condition, such as roller support. Its main goal is to demonstrate

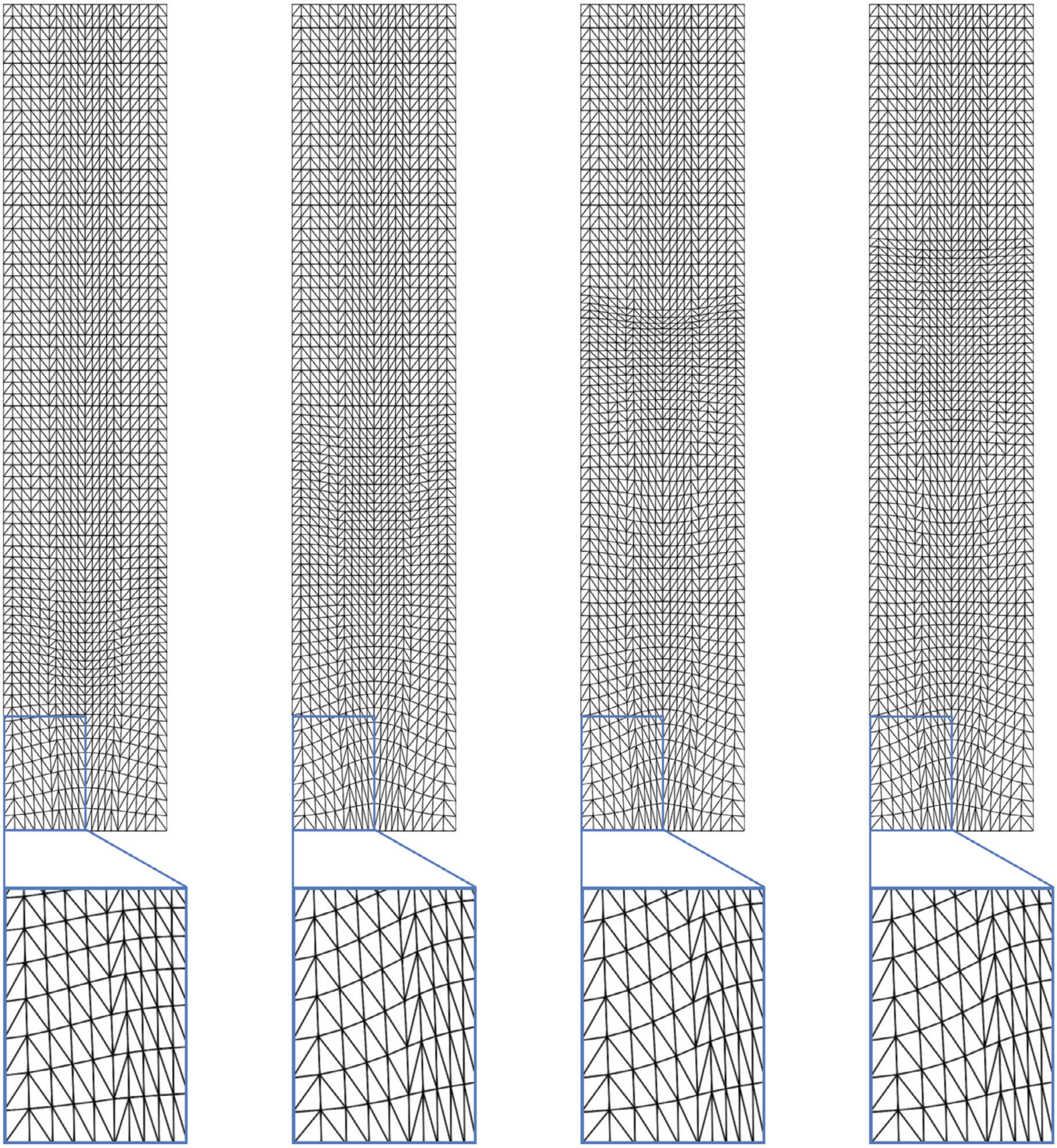

(a) 20 μs (b) 40 μs (c) 60 μs (d) 80 μs

Fig. 16. Taylor bar impact: two-dimensional view of a series of material mesh deformation at time $\{t = 20, 40, 60, 80\}$ µs (from left to right).

Table 8
Simulation parameters for isothermal Taylor bar impact.

Young's modulus	E [MPa]	117
Material density	ρ_X [kg/m^3]	8930
Poisson's ratio	ν	0.35
Initial Yield Stress	$\bar{\tau}_y^0$ [GPa]	0.4
Hardening Modulus	H [GPa]	0.1
ALE parameter 1	α_{ALE}	1
ALE parameter 2	μALE	0.02μ

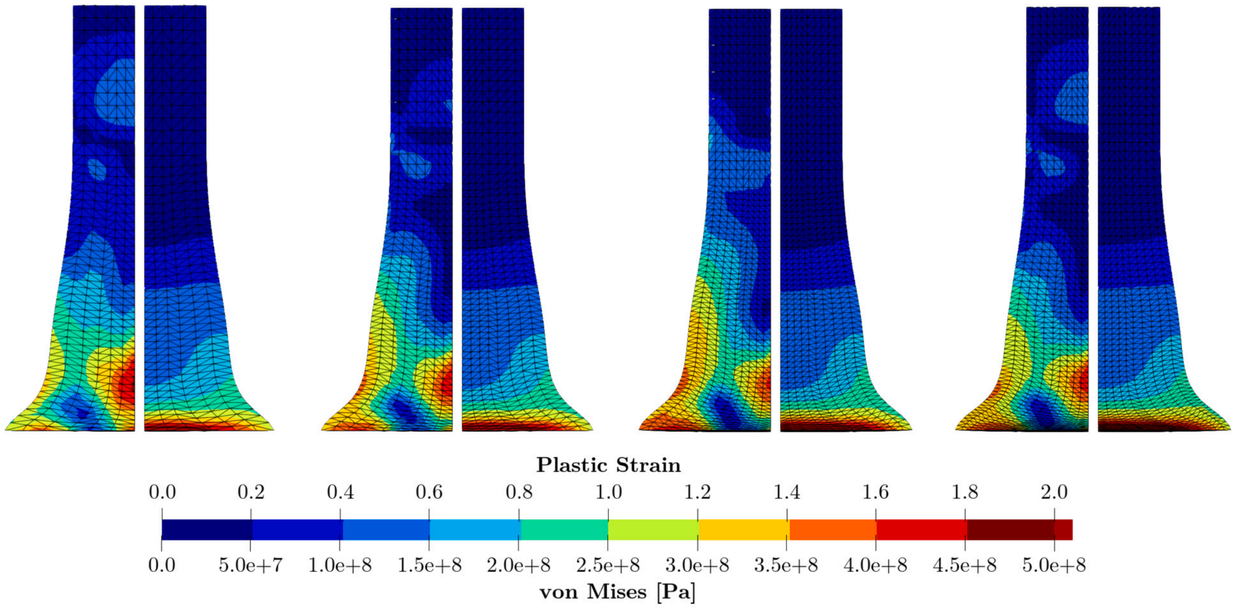

Fig. 17. Taylor bar impact: comparison of the deformed shapes at time $t = 80$ μs. The first three columns (left to right) show the mesh refinement of a structure simulated using the proposed ALE algorithm, whereas the last column (at the rightmost position) shows a deformed structure via an alternative in-house Total Lagrangian vertex-based finite volume algorithm [41]. Colour indicates both von Mises (left portion of the subfigure) and equivalent plastic strain (right portion of the subfigure) profiles. A von Mises plasticity model using isotropic linear hardening rule is used. The parameters related to material properties are summarised in Table 8.

Table 9
Simulation parameters for Taylor bar impact with thermal coupling.

Young's modulus	E [MPa]	124
Material density	ρ_X [kg/m^3]	8960
Poisson's ratio	ν	0.34
Yield stress	A [MPa]	90
Hardening modulus	B [MPa]	292
Hardening exponent	q	0.31
Melting temperature	θ_{melt} [K]	1356
Transition temperature	$\theta_{\text{transition}}$ [K]	298.15
Strain rate coefficient	C	0.025
Initial strain rate	$\dot{\varepsilon}_0$ [s^{-1}]	1
Temperature exponent	m	1.09
Reference temperature	θ_{ref} [K]	298.15
Thermal conductivity	h [W m^{-1}K^{-1}]	286
Specific heat capacity	C_v [J kg^{-1} K^{-1}]	383
Thermal expansion rate	α [K^{-1}]	5×10^{-5}

the advantages of the proposed ALE algorithm compared to traditional Lagrangian methods in scenarios involving large plastic flow near the contact region. When using classical Lagrangian approaches, severe distortions in elements are often encountered. To mitigate the significant compression of elements around the contact area, it would be beneficial to consider ALE mesh motion. This ALE smoothing procedure would stretch the meshes in those regions vertically upwards, thereby maintaining a high quality of the spatial mesh. This indeed can be achieved by solving the conservation-type law, as described in (33). The function $\bar{\boldsymbol{F}}$ is specifically selected to be

$$\bar{\boldsymbol{F}} = \begin{bmatrix} 1 & 0 & 0 \\ 0 & F_{22} & 0 \\ 0 & 0 & 1 \end{bmatrix}. \tag{84}$$

A sequence of snapshots illustrating the evolving material mesh motion is shown in Fig. 16.

To validate the consistency of our ALE algorithm, we discretise a quarter section of the bar using three different levels of mesh refinement, namely (**M1**) 1887, (**M2**) 3721 and (**M3**) 17280 number of linear tetrahedral elements. The deformation patterns of the structures at time $t = 80$ μs are shown in Fig. 17. Remarkably, these patterns and plastic strain distributions exhibit excellent agreement across all the levels of mesh refinement. Additionally, in Fig. 18, we compare the results obtained using the ALE algorithm (based on **M3**) with those simulated using the Total Lagrangian Godunov-type finite volume algorithm [41]. The top row of this figure presents

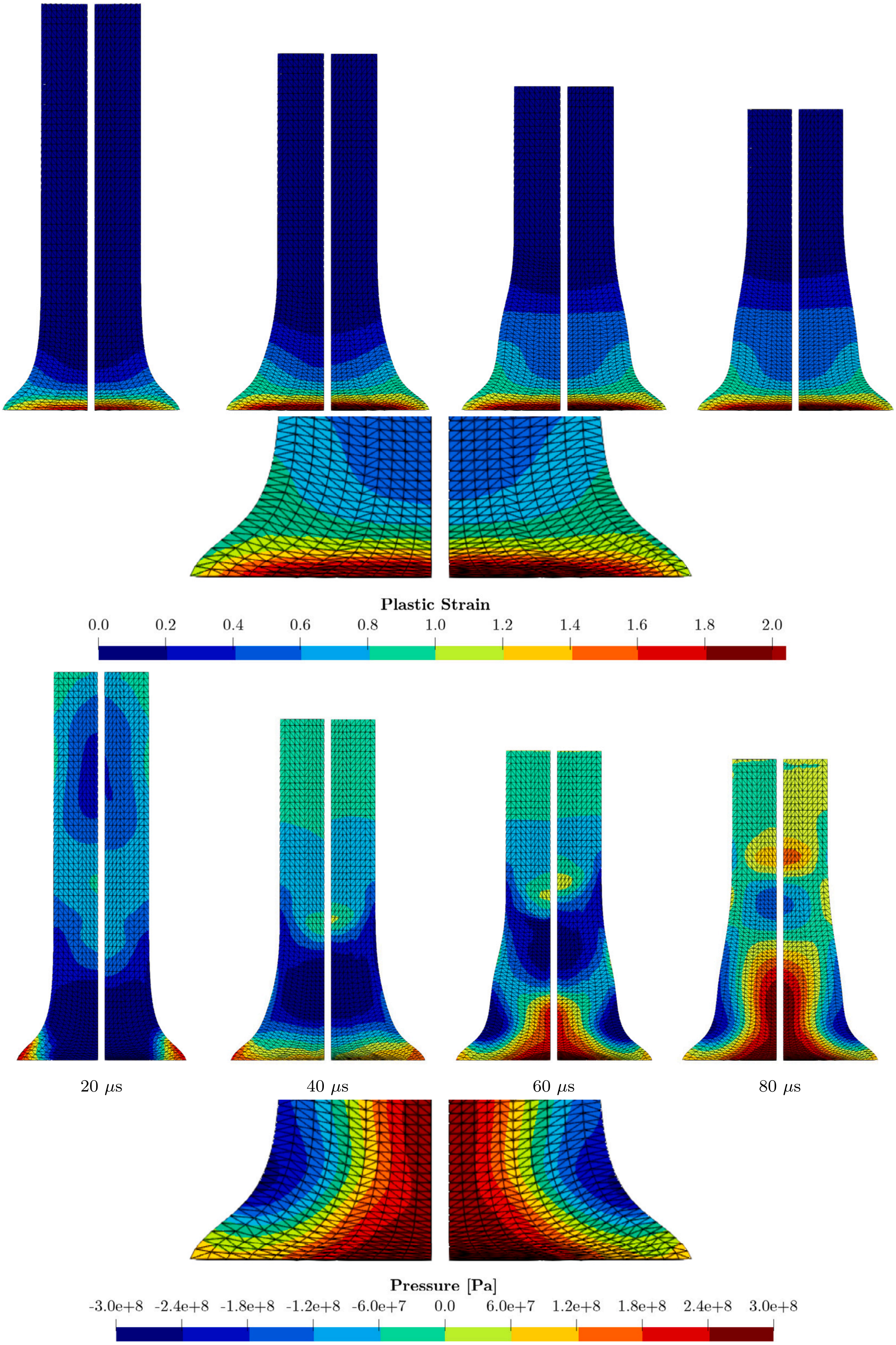

Fig. 18. Taylor bar impact: a series of snapshots at times $t = \{20, 40, 60, 80\}$ μs (from left to right). Colour indicates (first row) the equivalent plastic strain and (second row) the pressure distribution, along with their zoomed-in plots. Each subfigure is divided into two parts: the left side represents the results of ALE, and the right side illustrates those of the Total Lagrangian approach [41]. Results obtained using a von-Mises plasticity model and the corresponding material parameters are summarised in Table 8.

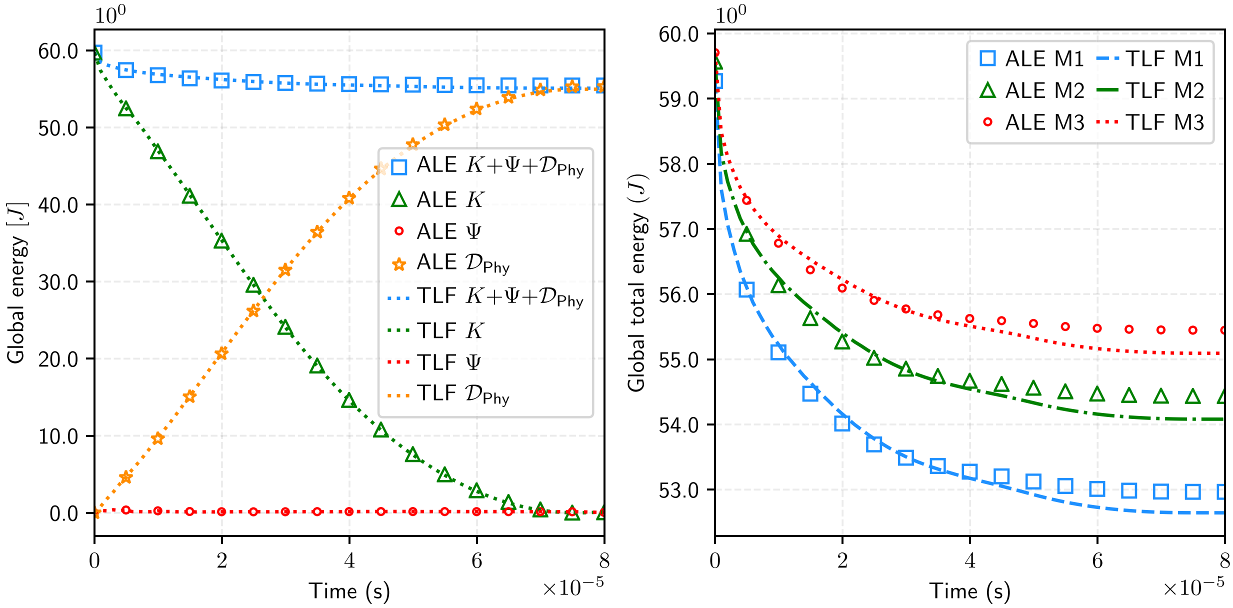

(a) (b)

Fig. 19. Taylor bar impact: time evolution of (a) different energy measures and (b) total energy. Results obtained using a von-Mises plasticity model with isotropic linear hardening rule. Parameters related to the material properties are tabulated in Table 8.

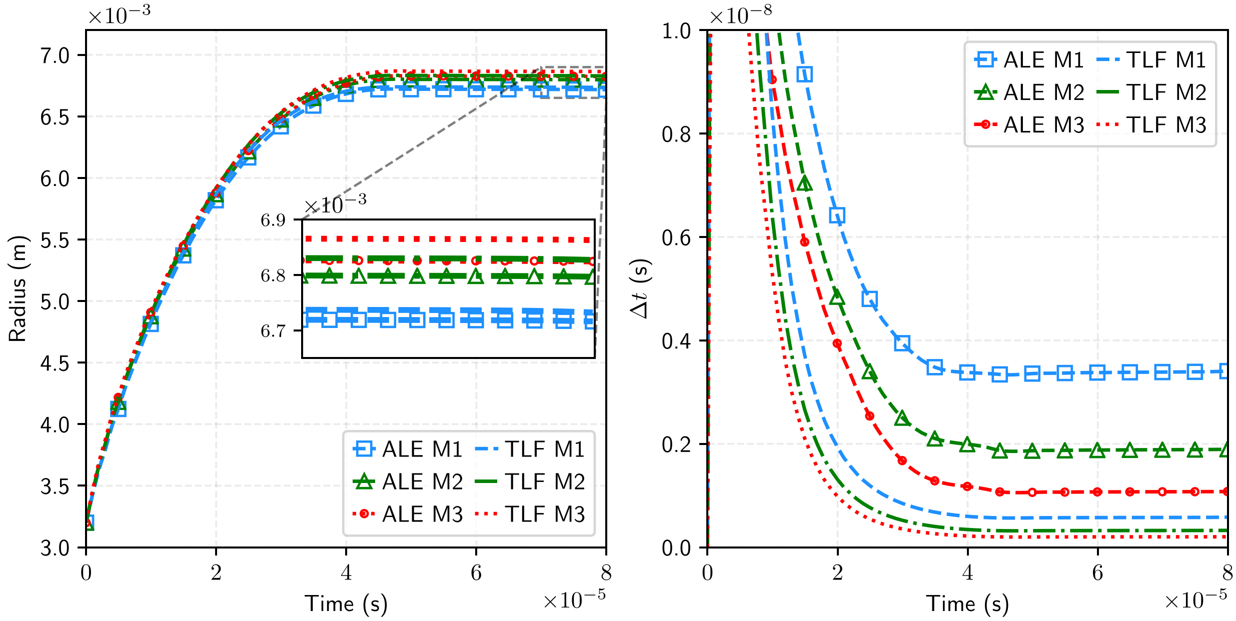

(a) (b)

Fig. 20. Taylor bar impact: time evolution of (a) radius at $\boldsymbol{X} = [0.0032, 0, 0.0324]^T$ and (b) time increment Δt. Results obtained using a von-Mises plasticity model with isotropic linear hardening rule. Parameters related to the material properties and the mesh motion are summarised in Table 8.

a series of snapshots illustrating the equivalent plastic strain distribution, while the bottom row focuses on the pressure profile. Each subfigure is divided into two parts: the left side represents the results of ALE, and the right side illustrates those of the Total Lagrangian approach. It is evident that both approaches yield similar results. However, the ALE algorithm demonstrates a notable advantage in maintaining more regular elements around the contact area. This improvement is particularly evident in the zoomed-in plots presented in Fig. 18, highlighting the capability of ALE algorithm in handling of element distortions in high-impact scenarios.

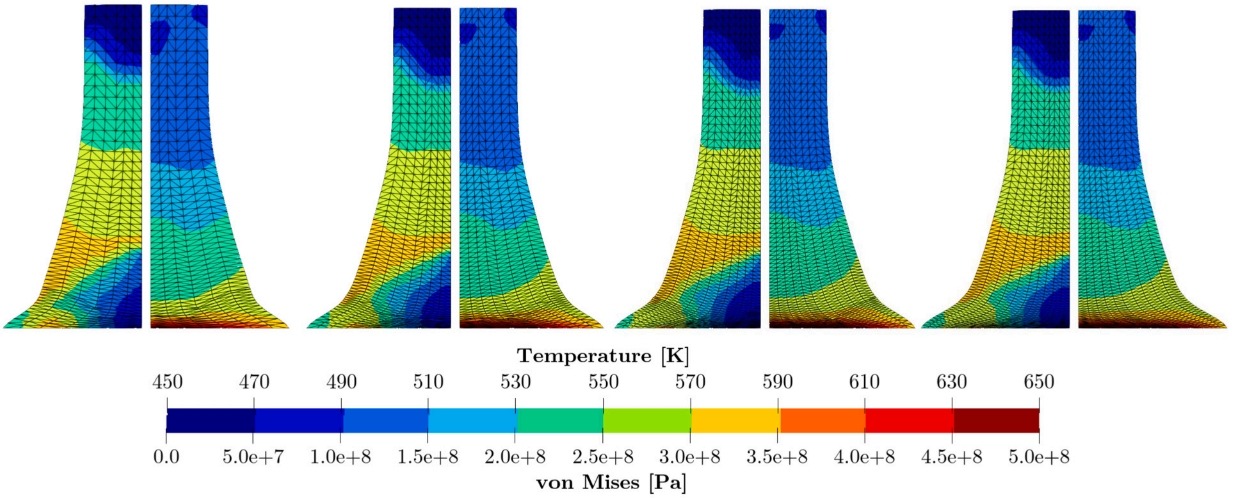

Fig. 21. Taylor bar impact with thermal coupling: comparison of the deformed shapes at time $t = 80$ µs. The first three columns (left to right) show the mesh refinement of a structure simulated using the proposed ALE algorithm, whereas the last column (at the rightmost position) shows a deformed structure via an alternative in-house Total Lagrangian vertex-based finite volume algorithm [41]. Colour indicates both von Mises and temperature profiles. A von Mises plasticity model using nonlinear Johnson-Cook hardening rule is used. The parameters related to material properties are summarised in Table 9.

In Fig. 19a, we present the time evolution of various energy measures during impact simulation. As the impact occurs, a significant portion of the kinetic energy is transformed into physical plastic dissipation, while a small fraction is converted into elastic strain energy. This shows the dynamic energy transfer that occurs during the impact process. Fig. 19b illustrates how the total energy of the system decreases with mesh refinement. Notably, the global total energy consistently decreases over time throughout the simulation. This trend indicates the long-term stability of the system and aligns with the second law of thermodynamics, ensuring the physical credibility of the simulation. We also monitor the radius evolution at position $\boldsymbol{X} = [0.0032, 0, 0.0324]^T$. This is seen in Fig. 20a. Our results show excellent agreement with those obtained using the Total Lagrangian approach, as referenced in [41]. An important advantage of the ALE method is its ability to alleviate element distortion, which is a significant benefit in simulations involving high-speed impact. Due to this advantage, the ALE method typically allows for larger time increments compared to the Total Lagrangian counterpart, as depicted in Fig. 20b. This aspect enhances computational efficiency and contributes to the robustness of the algorithm under challenging conditions.

To further demonstrate the robustness of the algorithm in coupled physics, we incorporate temperature effects into our simulation. Initially, we set a uniform temperature profile across the bar, defined as $\theta(\chi, t = 0) = 573.15$ K. This high initial temperature introduces a thermal softening behaviour, noticeable at the contact plane where temperature accumulates rapidly during impact. To assess the efficiency of this approach, we performed a comparative analysis between the results obtained using the ALE algorithm and those obtained from the Total Lagrangian method. The comparison revealed excellent agreement between the two, with the ALE algorithm maintaining more regular mesh shapes in the vicinity of the contact region. These results are shown in Figs. 21 and 22. Moreover, Fig. 23 denotes the evolution of various energy measures through the simulation. Again, as anticipated, the global energy of the system decreases over time, strictly adherence to the second law of thermodynamics. For a more visual representation of the impact process, Fig. 24 showcases a series of snapshots displaying the temperature profile of the bar.

9.6. Accuracy in the necking plastic region

Based on the problem setup previously discussed in the Taylor bar problem, we now modify the scenario by reversing the initial velocity field of the bar, causing it to stretch on both sides. The primary focus of this fast stretching problem is to demonstrate the effectiveness of the proposed ALE methodology, particularly in its ability to accurately and reliably capture the plastic flow around the necking region. Classical Lagrangian approaches may struggle in accurately resolving plastic deformation because the elements around the necking region become highly stretched [37]. A possible solution to address this issue is to perform non-uniform refinement by placing more elements in the necking region to better capture its deformation behaviour.

In this simulation, we employ a Hencky-based von-Mises plasticity model coupled with a nonlinear Johnson-Cook hardening law. The material properties used are identical to those in the previously explored Taylor bar example (with thermal coupling) and are detailed in Table 9. To consider the influence of thermal effects, the initial temperature profile of the bar is set at $\theta(\chi, t = 0) = 573.15$ K. The mesh motion in this scenario is driven by solving expression (33), using the same function $\bar{\boldsymbol{F}}$ as in the Taylor bar. Fig. 25 displays a sequence of material mesh motions, focusing particularly around the necking region. Due to the extensive stretching involved in this problem, the material mesh motion tends to compress, thereby ensuring that the spatial mesh elements remain regular and of high quality, which is crucial for capturing the behaviour of the material under such extreme conditions.

First, we carried out a mesh refinement analysis using the proposed ALE formulation, as shown in Fig. 26. Three levels of mesh refinements are used, namely (**M1**) 1887, (**M2**) 3721 and (**M3**) 17280 linear tetrahedral elements. Both von-Mises stress and tem-

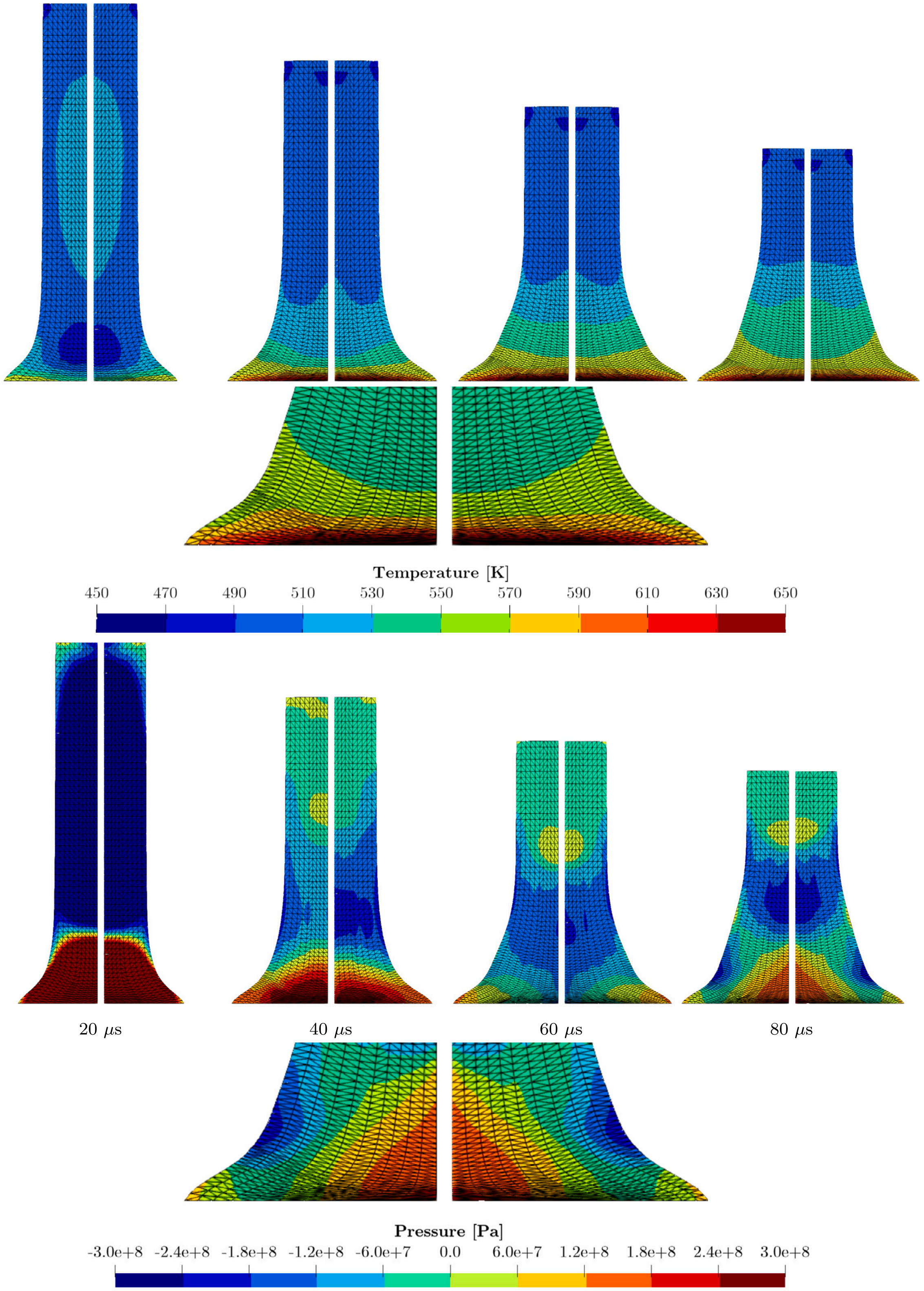

Fig. 22. Taylor bar impact with thermal coupling: a series of snapshots at times $t = \{20, 40, 60, 80\}$ µs (from left to right). Colour indicates (first row) the temperature and (second row) the pressure distribution, along with their zoomed-in plots. Each subfigure is divided into two parts: the left side represents the results of ALE, and the right side illustrates those of the Total Lagrangian approach [41]. Results obtained using a von-Mises plasticity model coupled with nonlinear Johnson-Cook hardening rule. The corresponding material parameters are summarised in Table 9.

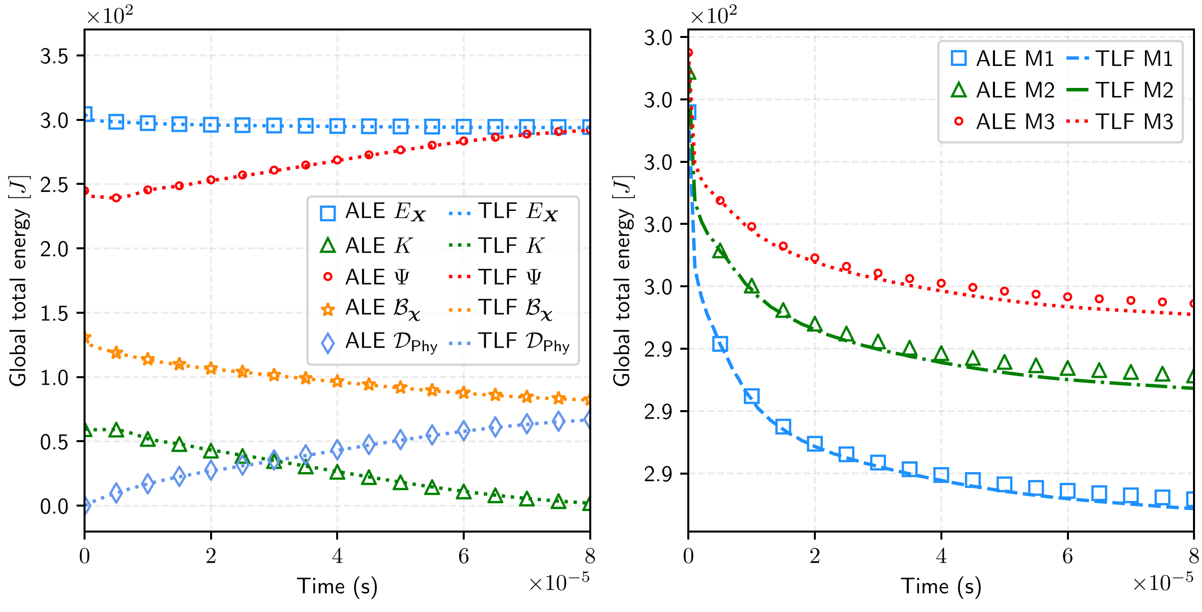

(a)

(b)

Fig. 23. Taylor bar impact with thermal coupling: time evolution of (a) different energy measures and (b) total energy. Results obtained using a von-Mises plasticity model with nonlinear Johnson-Cook hardening rule. Parameters related to the material properties and the mesh motion are tabulated in Table 9.

perature results display convergence with increased mesh refinement. In comparison with the Total Lagrangian approach, a notable advantage of using the ALE approach is the improved resolution in temperature. This improvement is attributed to a relatively larger number of elements concentrated around the necking region. In the Total Lagrangian approach, the elements in this area tend to become distorted, which negatively impacts the accuracy of the simulation.

Fig. 27 presents the deformation of the bar at different times $t = \{15, 20, 25, 30\}$ ms. In this figure, we compare the contours of von Mises stress and equivalent plastic strain for both the ALE formulation (on the left side) and the Total Lagrangian formulation (on the right side). As anticipated, the ALE approach demonstrates an improved resolution in capturing plastic strain in the areas proximal to necking. Furthermore, the evolution of various energy components, including *Ballistic* energy, shows excellent agreement between the two formulations. As seen in Fig. 28, the reduction in total energy throughout the simulation confirms adherence to the second law of thermodynamics, ensuring long-term stability of the simulation results. For additional comparative analysis, Fig. 29a monitors the evolution of the necking radius. The ALE approach yields a larger radius value due to a more accurate representation of temperature effects. The evolution of the time increment is monitored in Fig. 29b for completeness. To enhance visual understanding, Fig. 30 includes a series of snapshots, showcasing the contours of plastic strain together with temperature distribution. Stable solutions are observed.

10. Conclusions

This paper presents a first-order hyperbolic Arbitrary Lagrangian Eulerian (ALE) conservation system tailored for simulating solid dynamics in irreversible processes, such as thermal effects and/or inelastic constitutive models. The system integrates essential physical conservation laws, including the mass continuity equation, linear momentum conservation equation and the first law of thermodynamics expressed in terms of the entropy density. Furthermore, the simulation accuracy is enhanced by solving two auxiliary geometric conservation laws for the multiplicative computation of the physical deformation gradient tensor. To handle plasticity models, our approach includes additional ALE evolution equations for the precise tracking of internal state variables. Taking inspiration from the principles of conservation laws, our formulation adopts a conservation-based strategy for the update of the mesh motion. This approach is particularly advantageous for overcoming plasticity-related challenges that are prevalent in classical Lagrangian approaches, such as those encountered during high-speed impact and rapid stretching (necking) scenarios. By enforcing suitable conditions on kinematics, the proposed ALE framework can be degenerated into alternative mixed-based systems for irreversible solid dynamics, including Total Lagrangian, Updated Reference Lagrangian, and Eulerian formulations.

From a discretisation perspective, we employ an entropy-stable vertex-centred Finite Volume algorithm. This approach ensures non-negative numerical entropy production over time through the careful approximation of both internal and boundary interface fluxes using an acoustic Riemann solver. The effectiveness of this methodology is validated by monitoring the discrete variation of the Ballistic energy of the system across several numerical examples. A three-stage Runge-Kutta explicit time integrator is used to integrate the system of discrete equations in time. Through a series of numerical examples presented in this paper, we demonstrate the capability of the algorithm in ensuring (1) geometric conservation condition for a rigid translation test, (2) proper order of convergence

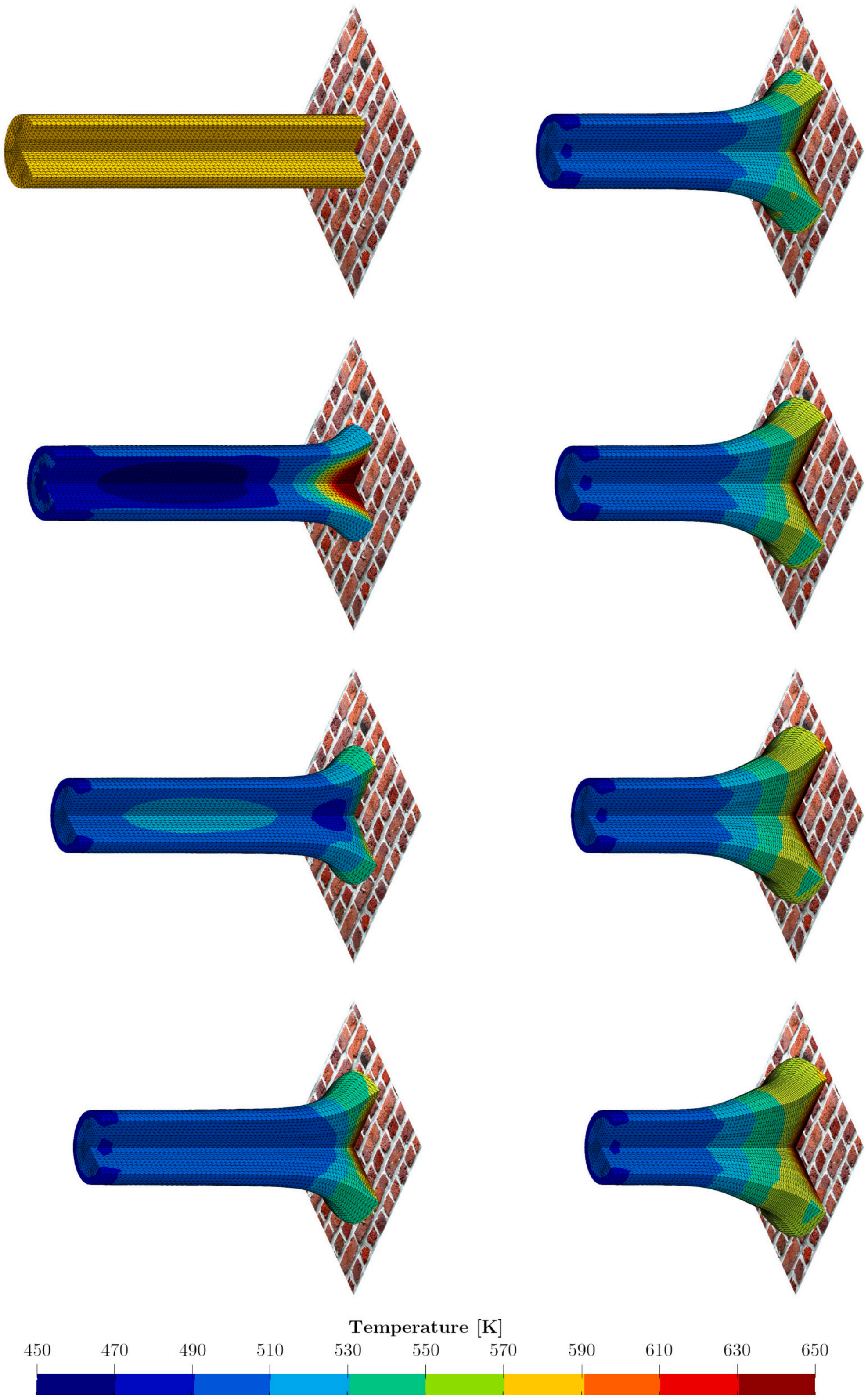

Fig. 24. Taylor bar impact with thermal coupling: a sequence of deformed structures with temperature distribution at times (left column, top to bottom) $t = \{0, 10, 20, 30\}$ µs and (right column, from top to bottom) $t = \{40, 50, 60, 70\}$ µs, respectively. Results obtained using a von Mises based Johnson-Cook plasticity model with **M3** mesh. Parameters related to material properties and the mesh motion are summarised in Table 9.

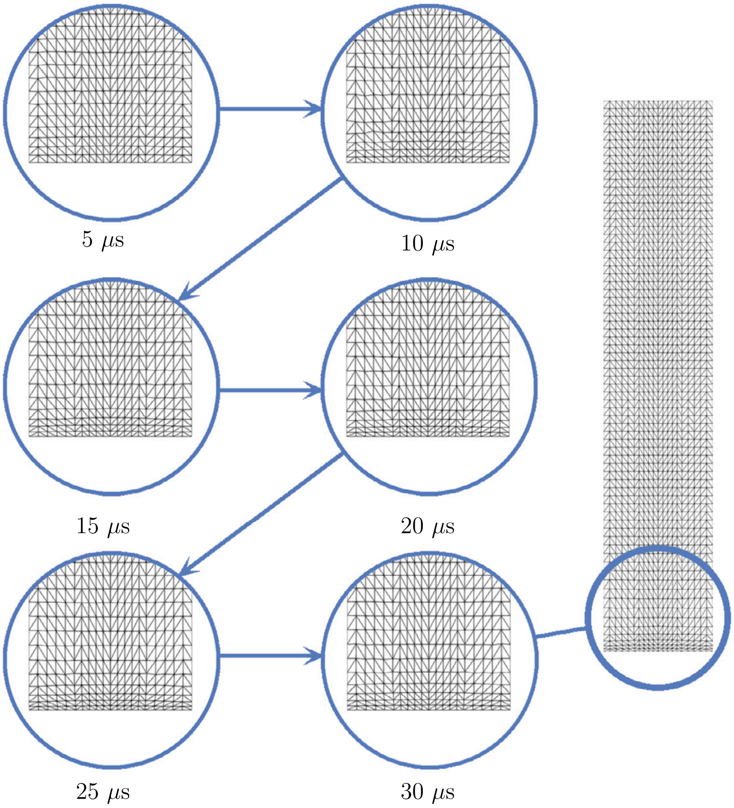

Fig. 25. Necking bar with thermal coupling: zoomed-in view of a series of material mesh deformation at time $t = \{5, 10, 15, 20, 25, 30\}$ μs (from left to right and top to bottom).

of the overall algorithm and (3) global production of both physical (such as, plastic dissipation and irrecoverable thermal effects) and numerical entropy (due to the involvement of numerical stabilisation) throughout the entire simulation. Additionally, the benefits of using an ALE approach are illustrated in plasticity scenarios, such as preventing element distortions near impact zones in high-speed Taylor impact situations and improving resolution accuracy during the process of plastic necking by dynamically adjusting meshes to better capture significant deformations. Future work will aim to refine and extend the framework to efficiently tackle challenges associated with single and multiple evolving interfaces.

CRediT authorship contribution statement

Thomas B.J. Di Giusto: Writing – original draft, Visualization, Software, Methodology, Investigation, Formal analysis, Data curation, Conceptualization. **Chun Hean Lee:** Writing – original draft, Validation, Supervision, Software, Project administration, Methodology, Investigation, Funding acquisition, Formal analysis, Conceptualization. **Antonio J. Gil:** Writing – review & editing, Supervision, Project administration, Methodology, Investigation, Funding acquisition, Formal analysis, Conceptualization. **Javier Bonet:** Writing – review & editing, Supervision, Methodology, Funding acquisition, Formal analysis, Conceptualization. **Clare Wood:** Writing – review & editing, Methodology, Investigation, Conceptualization. **Matteo Giacomini:** Writing – review & editing, Supervision, Funding acquisition.

Declaration of competing interest

The authors declare that they have no known competing financial interests or personal relationships that could have appeared to influence the work reported in this paper.

Data availability

Data will be made available on request.

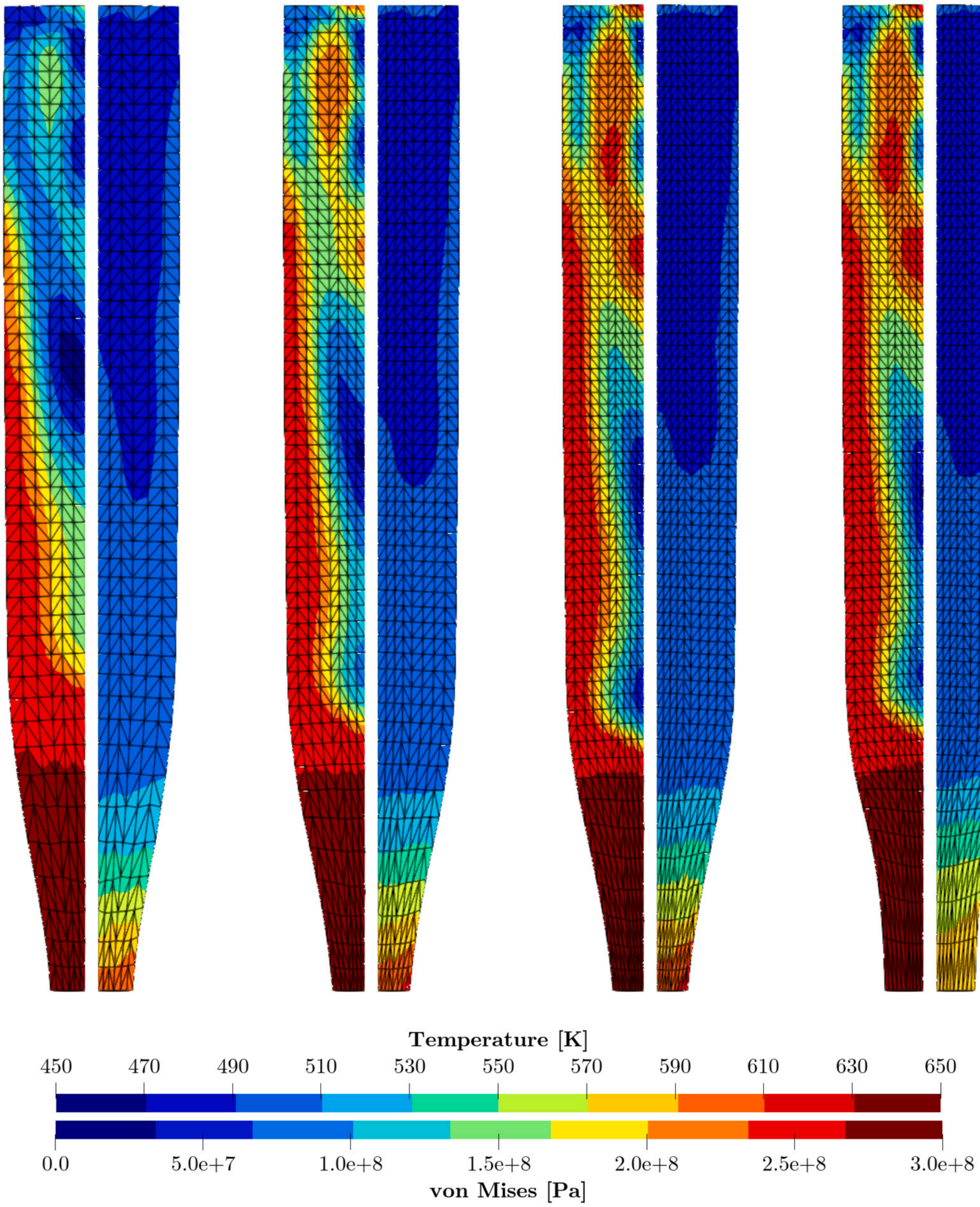

Fig. 26. Necking bar with thermal coupling: comparison of the deformed shapes at time $t = 30$ µs. The first three columns (left to right) show the mesh refinement of a structure simulated using the proposed ALE algorithm, whereas the last column (at the rightmost position) shows a deformed structure via an alternative in-house Total Lagrangian vertex-based finite volume algorithm [41]. Colour indicates both von Mises (left of each subfigure) and temperature (right of each subfigure) profiles. A von Mises plasticity model using nonlinear Johnson-Cook hardening rule is used. The parameters related to material properties are summarised in Table 9.

Acknowledgements

The first, second and third authors would like to acknowledge the financial support received through the project Marie Skłodowska-Curie ITN-EJD ProTechTion, funded by the European Union Horizon 2020 research and innovation program with grant number 764636. CHL acknowledges the support provided by FIFTY2 Technology GmbH via project reference 322835. AJG acknowledges the support provided by UK AWE via project PO 40062030. JB acknowledges the financial support received via project POTENTIAL (PID2022-141957OB-C21) funded by MICIU/AEI/10.13039/501100011033/FEDER, UE. MG acknowledges the Spanish Ministry of Science, Innovation and Universities and Spanish State Research Agency MICIU/AEI/10.13039/501100011033 (Grants No. PID2020-113463RB-C33 and CEX2018-000797-S) and the Generalitat de Catalunya (Grant No. 2021-SGR-01049). MG is Fellow of the Serra Húnter Programme of the Generalitat de Catalunya.

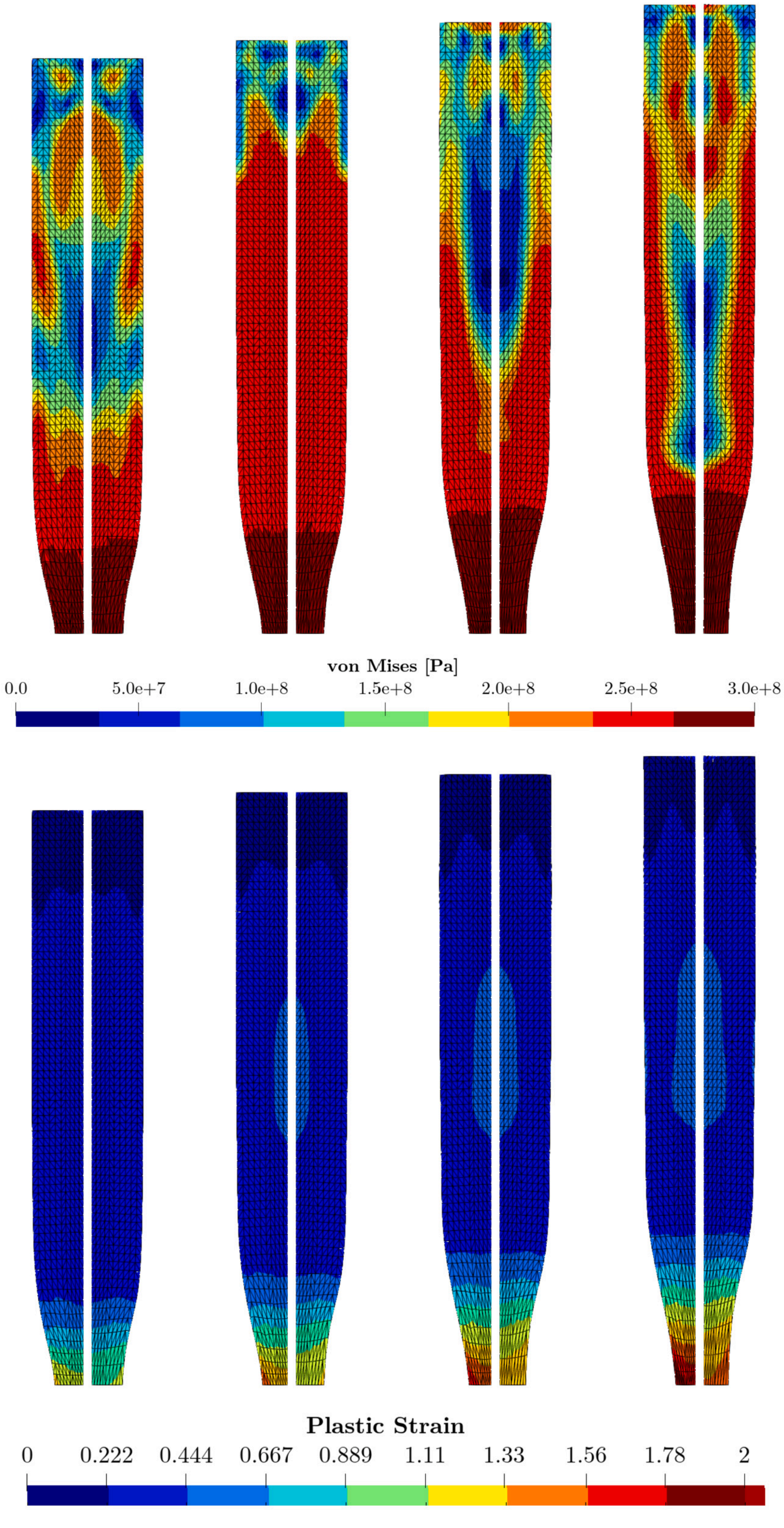

Fig. 27. Necking with thermal coupling: a series of snapshots at times $t = \{15, 20, 25, 30\}$ μs (from left to right). Colour indicates (first row) the von Mises stress and (second row) the plastic strain distribution. Each subfigure is divided into two parts: the left side represents the results of ALE, and the right side illustrates those of the Total Lagrangian approach [41]. Results obtained using a von-Mises plasticity model coupled with nonlinear Johnson-Cook hardening rule. The corresponding material parameters are summarised in Table 9.

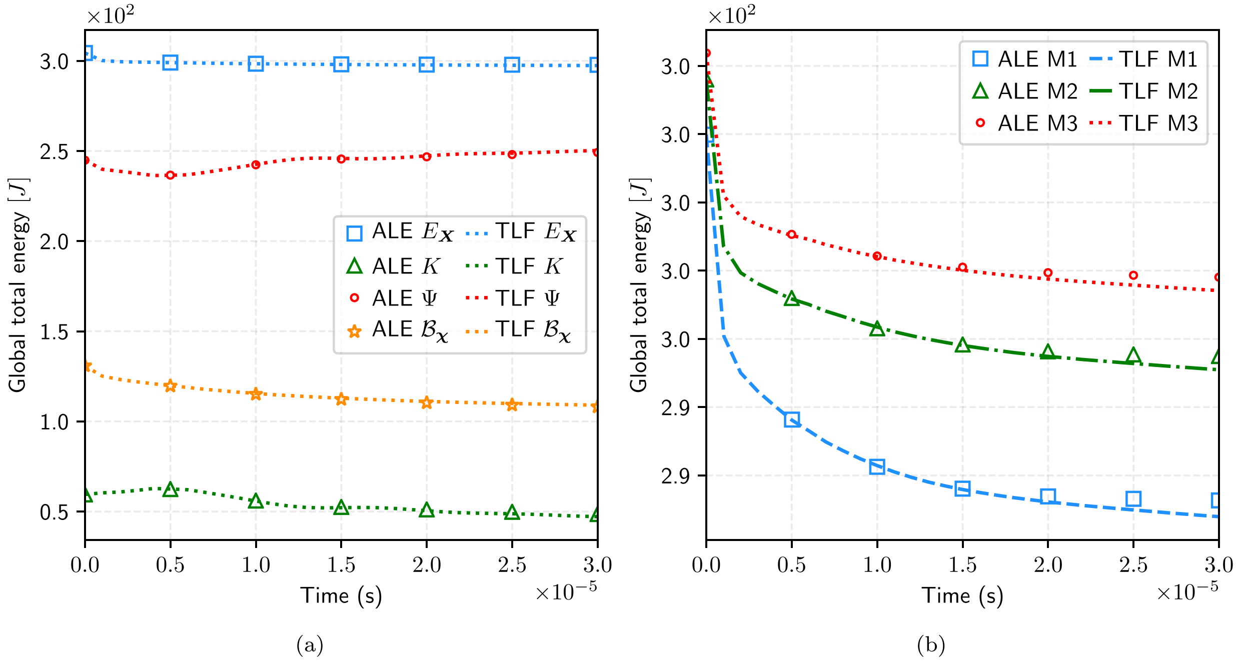

Fig. 28. Necking bar with thermal coupling: time evolution of (a) different energy measures and (b) total energy. Results obtained using a von Mises plasticity model coupled with nonlinear Johnson-Cook hardening rule. Parameters related to the material properties are tabulated in Table 9.

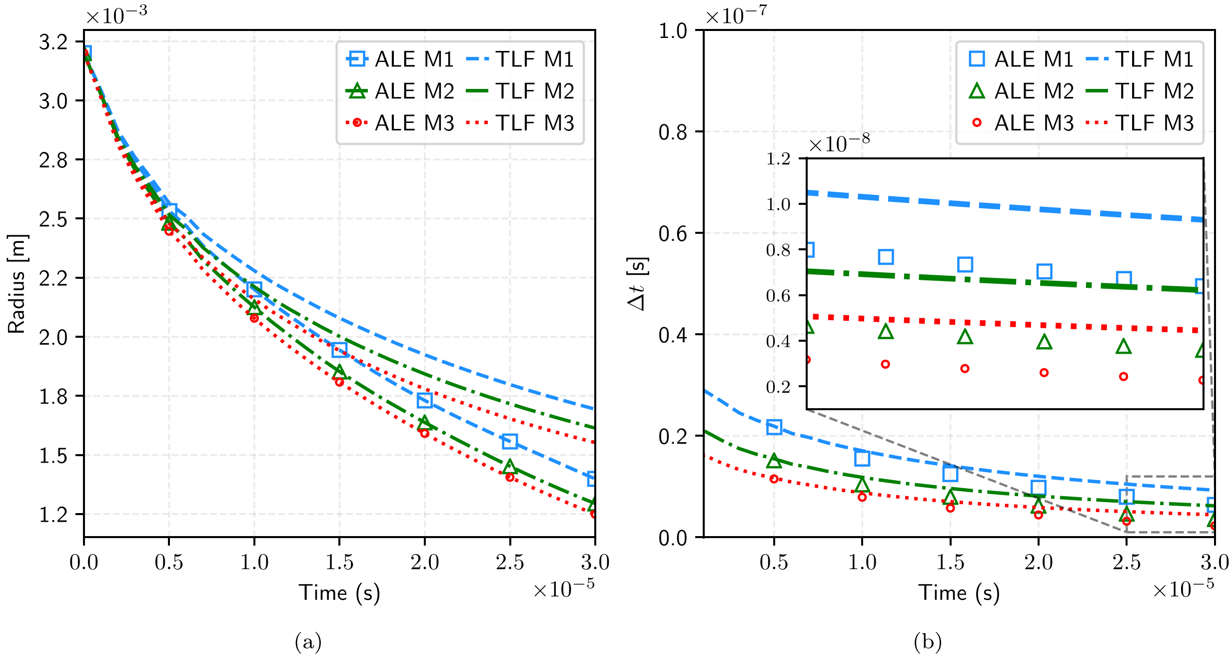

Fig. 29. Necking bar with thermal coupling: time evolution of (a) radius at $\boldsymbol{X} = [0.0032, 0, 0.0324]^T$ and (b) time increment Δt. Results obtained using a von Mises plasticity model coupled with nonlinear Johnson-Cook hardening rule. Parameters related to the material properties are summarised in Table 9.

Appendix A. The ALE transformation

To derive the ALE conservation form from the Total Lagrangian conservation laws, we first relate the Total Lagrangian laws, typically defined in the material domain, to their ALE counterparts in the fixed referential domain. This involves transforming the global Total Lagrangian conservation law by applying the Jacobian transformation (on the volume integral), Nanson's rule (on the surface integral), and the Reynolds transport theorem to the material time derivative, which eventually results in [26]

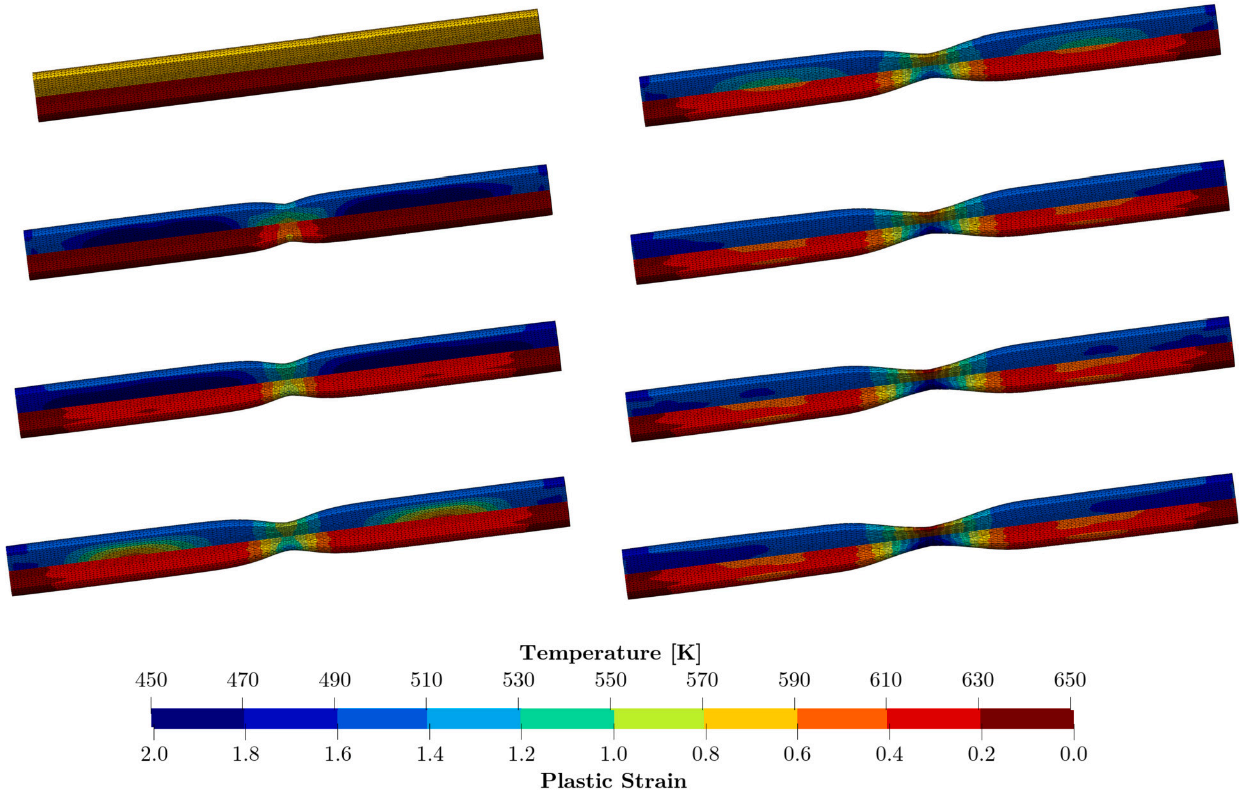

Fig. 30. Necking bar with thermal coupling: a sequence of deformed structures at times (left column, top to bottom) $t = \{0, 5, 10, 15\}$ ms and (right column, from top to bottom) $t = \{20, 25, 28, 30\}$ ms, respectively. Colour contour indicates temperature (top of each subfigure) and plastic strain (bottom of each subfigure) distributions. Results obtained using a von Mises based Johnson-Cook plasticity model with **M3** mesh. Parameters related to material properties are summarised in Table 9.

$$\frac{d}{dt}\int_{\Omega_\chi} \boldsymbol{\mathcal{U}}_\chi \, d\Omega_\chi + \int_{\partial\Omega_\chi} \boldsymbol{\mathcal{F}}_\chi \, d\boldsymbol{A}_\chi = \int_{\Omega_\chi} \boldsymbol{\mathcal{S}}_\chi \, d\Omega_\chi. \tag{A.1}$$

Equivalently, the associated ALE local differential equation and its jump condition are

$$\left.\frac{\partial}{\partial t}\right|_\chi \boldsymbol{\mathcal{U}}_\chi + \mathrm{DIV}_\chi \boldsymbol{\mathcal{F}}_\chi = \boldsymbol{\mathcal{S}}_\chi, \qquad U_\chi [\![\boldsymbol{\mathcal{U}}_\chi]\!] = [\![\boldsymbol{\mathcal{F}}_\chi]\!] \boldsymbol{N}_\chi. \tag{A.2}$$

The transformed conservation variables, fluxes and source terms are given by

$$\boldsymbol{\mathcal{U}}_\chi = J_{\boldsymbol{\Psi}} \boldsymbol{\mathcal{U}}_X; \qquad \boldsymbol{\mathcal{S}}_\chi = J_{\boldsymbol{\Psi}} \boldsymbol{\mathcal{S}}_X; \qquad \boldsymbol{\mathcal{F}}_\chi = \left(\boldsymbol{\mathcal{F}}_X - \boldsymbol{\mathcal{U}}_X \otimes \boldsymbol{W}\right) \boldsymbol{H}_{\boldsymbol{\Psi}}, \tag{A.3}$$

where $\{\boldsymbol{\mathcal{U}}_X, \boldsymbol{\mathcal{F}}_X, \boldsymbol{\mathcal{S}}_X\}$ are defined as the conservation variables, fluxes and source term in the material domain, respectively.

Moreover, noticing $\left.\frac{\partial}{\partial t}\right|_\chi J_{\boldsymbol{\Psi}} = \mathrm{DIV}_\chi \left(\boldsymbol{H}_{\boldsymbol{\Psi}}^T \boldsymbol{W}\right)$ (8d), a non-conservative local conservation equation emerges as

$$J_{\boldsymbol{\Psi}} \left.\frac{\partial}{\partial t}\right|_\chi \boldsymbol{\mathcal{U}}_X - \left(\boldsymbol{\nabla}_\chi \boldsymbol{\mathcal{U}}_X\right)\left(\boldsymbol{H}_{\boldsymbol{\Psi}}^T \boldsymbol{W}\right) + \mathrm{DIV}_\chi \left(\boldsymbol{\mathcal{F}}_X \boldsymbol{H}_{\boldsymbol{\Psi}}\right) = J_{\boldsymbol{\Psi}} \boldsymbol{\mathcal{S}}_X. \tag{A.4}$$

References

[1] J. Bonet, A.J. Burton, A simple average nodal pressure tetrahedral element for incompressible and nearly incompressible dynamic explicit applications, Commun. Numer. Methods Eng. 14 (1998) 437–449.
[2] D.P. Flanagan, T. Belytschko, A uniform strain hexahedron and quadrilateral with orthogonal hourglass control, Int. J. Numer. Methods Eng. 17 (1981) 679–706.
[3] S.K. Lahiri, J. Bonet, J. Peraire, L. Casals, A variationally consistent fractional time-step integration method for incompressible and nearly incompressible Lagrangian dynamics, Int. J. Numer. Methods Eng. 63 (2005) 1371–1395.
[4] J. Bonet, A.J. Gil, R.D. Wood, Nonlinear Solid Mechanics for Finite Element Analysis: Statics, Cambridge University Press, 2016.
[5] M.W. Gee, C.R. Dohrmann, S.W. Key, W.A. Wall, A uniform nodal strain tetrahedron with isochoric stabilization, Int. J. Numer. Methods Eng. 78 (2009) 429–443.
[6] I.-H. Son, Y.-T. Im, Localized remeshing techniques for three-dimensional metal forming simulations with linear tetrahedral elements, Int. J. Numer. Methods Eng. 67 (2006) 672–696.
[7] W.E. Pracht, Calculating three-dimensional fluid flows at all speeds with an Eulerian-Lagrangian computing mesh, J. Comput. Phys. 17 (1975) 132–159.
[8] T.J. Hughes, W.K. Liu, T.K. Zimmermann, Lagrangian-Eulerian finite element formulation for incompressible viscous flows, Comput. Methods Appl. Mech. Eng. 29 (1981) 329–349.

[9] G. Scovazzi, T.J.R. Hughes, Lecture notes on continuum mechanics on arbitrary moving domains, Sandia National Laboratories, 2007.

[10] J. Donea, A. Huerta, Finite Element Methods for Flow Problems, Wiley and Sons, 2004.

[11] A. Huerta, F. Casadei, New ALE applications in non-linear fast-transient solid dynamics, Eng. Comput. 11 (1994) 317–345.

[12] A.J. Barlow, P.-H. Maire, W.J. Rider, R.N. Rieben, M.J. Shashkov, Arbitrary Lagrangian–Eulerian methods for modeling high-speed compressible multimaterial flows, J. Comput. Phys. 322 (2016) 603–665.

[13] J. Breil, S. Galera, P.-H. Maire, Multi-material ALE computation in inertial confinement fusion code chic, Comput. Fluids 46 (2011) 161–167, 10th ICFD Conference Series on Numerical Methods for Fluid Dynamics (ICFD 2010).

[14] A.J. Barlow, A compatible finite element multi-material ALE hydrodynamics algorithm, Int. J. Numer. Methods Fluids 56 (2008) 953–964.

[15] X. Zeng, K. Li, G. Scovazzi, An ALE/embedded boundary method for two-material flow simulations, Comput. Math. Appl. 78 (2019) 335–361, Proceedings of the Eight International Conference on Numerical Methods for Multi-Material Fluid Flows (MULTIMAT 2017).

[16] J. Donea, A. Huerta, J.-P. Ponthot, A. Rodriguez-Ferran, Arbitrary Lagrangian–Eulerian Methods, John Wiley and Sons, 2004.

[17] E. Kuhl, H. Askes, P. Steinmann, An ALE formulation based on spatial and material settings of continuum mechanics. Part 1: Generic hyperelastic formulation, Comput. Methods Appl. Mech. Eng. 193 (2004) 4207–4222, The Arbitrary Lagrangian-Eulerian Formulation.

[18] H. Askes, E. Kuhl, P. Steinmann, An ALE formulation based on spatial and material settings of continuum mechanics. Part 2: Classification and applications, Comput. Methods Appl. Mech. Eng. 193 (2004) 4223–4245, The Arbitrary Lagrangian-Eulerian Formulation.

[19] A. Rodríguez-Ferran, F. Casadei, A. Huerta, ALE stress update for transient and quasistatic processes, Int. J. Numer. Methods Eng. 43 (1998) 241–262.

[20] A. Rodríguez-Ferran, A. Pérez-Foguet, A. Huerta, Arbitrary Lagrangian–Eulerian (ale) formulation for hyperelastoplasticity, Int. J. Numer. Methods Eng. 53 (2002) 1831–1851.

[21] F. Armero, E. Love, An Arbitrary Lagrangian–Eulerian finite element method for finite strain plasticity, Int. J. Numer. Methods Eng. 57 (2003) 471–508.

[22] T. Yamada, F. Kikuchi, An Arbitrary Lagrangian-Eulerian finite element method for incompressible hyperelasticity, Comput. Methods Appl. Mech. Eng. 102 (1993) 149–177.

[23] R. Loubère, P.-H. Maire, M. Shashkov, J. Breil, S. Galera, Reale: a reconnection-based arbitrary-Lagrangian-Eulerian method, J. Comput. Phys. 229 (2010) 4724–4761.

[24] S. Galera, P.-H. Maire, J. Breil, A two-dimensional unstructured cell-centered multi-material ALE scheme using VOF interface reconstruction, J. Comput. Phys. 229 (2010) 5755–5787.

[25] M. Berndt, J. Breil, S. Galera, M. Kucharik, P.-H. Maire, M. Shashkov, Two-step hybrid conservative remapping for multimaterial arbitrary Lagrangian–Eulerian methods, J. Comput. Phys. 230 (2011) 6664–6687.

[26] T.B.J. Di Giusto, C.H. Lee, A.J. Gil, J. Bonet, M. Giacomini, A first-order hyperbolic Arbitrary Lagrangian Eulerian conservation formulation for non-linear solid dynamics, Int. J. Numer. Methods Eng. (2024), https://doi.org/10.1002/nme.7467.

[27] J. Bonet, A.J. Gil, C.H. Lee, M. Aguirre, R. Ortigosa, A first order hyperbolic framework for large strain computational solid dynamics. Part I: Total Lagrangian isothermal elasticity, Comput. Methods Appl. Mech. Eng. 283 (2015) 689–732.

[28] G. Scovazzi, R. Zorrilla, R. Rossi, A kinematically stabilized linear tetrahedral finite element for compressible and nearly incompressible finite elasticity, Comput. Methods Appl. Mech. Eng. 412 (2023) 116076.

[29] A.J. Gil, C.H. Lee, J. Bonet, R. Ortigosa, A first order hyperbolic framework for large strain computational solid dynamics. Part II: Total Lagrangian compressible, nearly incompressible and truly incompressible elasticity, Comput. Methods Appl. Mech. Eng. 300 (2016) 146–181.

[30] J. Bonet, C.H. Lee, A.J. Gil, A. Ghavamian, A first order hyperbolic framework for large strain computational solid dynamics: Part III: Thermo-elasticity, Comput. Methods Appl. Mech. Eng. 373 (2020) 113505.

[31] G.H. Miller, P. Colella, A high-order Eulerian Godunov method for elastic-plastic flow in solids, J. Comput. Phys. 167 (2001) 131–176.

[32] P.R.R. de Campos, A.J. Gil, C.H. Lee, M. Giacomini, J. Bonet, A new updated reference Lagrangian smooth particle hydrodynamics algorithm for isothermal elasticity and elasto-plasticity, Comput. Methods Appl. Mech. Eng. 392 (2022) 114680.

[33] M.M.O. Hamed, A.T. McBride, B.D. Reddy, An ALE approach for large deformation thermoplasticity with application to friction welding, Comput. Mech. 72 (2023) 803–826.

[34] X. Zeng, G. Scovazzi, N. Abboud, O. Colomes, S. Rossi, A dynamic variational multiscale method for viscoelasticity using linear tetrahedral elements, Int. J. Numer. Methods Eng. 112 (2018).

[35] N. Abboud, G. Scovazzi, Elastoplasticity with linear tetrahedral elements: a variational multiscale method, Int. J. Numer. Methods Eng. 115 (2018).

[36] N. Abboud, G. Scovazzi, A variational multiscale method with linear tetrahedral elements for multiplicative viscoelasticity, Mech. Res. Commun. 112 (2021) 103610, Special issue honoring G.I. Taylor Medalist Prof. Arif Masud.

[37] C.H. Lee, P.R.R. de Campos, A.J. Gil, M. Giacomini, J. Bonet, An entropy-stable updated reference Lagrangian smoothed particle hydrodynamics algorithm for thermo-elasticity and thermo-visco-plasticity, Comput. Part. Mech. 10 (2023) 1493–1531.

[38] J. Bonet, A.J. Gil, R. Ortigosa, A computational framework for polyconvex large strain elasticity, Comput. Methods Appl. Mech. Eng. 283 (2015) 1061–1094.

[39] J. Bonet, A.J. Gil, R. Ortigosa, On a tensor cross product based formulation of large strain solid mechanics, Int. J. Solids Struct. 84 (2016) 49–63.

[40] C.H. Lee, A.J. Gil, J. Bonet, Development of a cell centred upwind finite volume algorithm for a new conservation law formulation in structural dynamics, Comput. Struct. 118 (2013) 13–38.

[41] O.I. Hassan, A. Ghavamian, C.H. Lee, A.J. Gil, J. Bonet, F. Auricchio, An upwind vertex centred finite volume algorithm for nearly and truly incompressible explicit fast solid dynamic applications: total and updated Lagrangian formulations, J. Comput. Phys. X 3 (2019) 100025.

[42] C.M. Dafermos, Quasilinear hyperbolic systems with involutions, Arch. Ration. Mech. Anal. 94 (1986) 373–389.

[43] J. Bonet, A.J. Gil, R.D. Wood, Nonlinear Solid Mechanics for Finite Element Analysis: Dynamics, Cambridge University Press, 2020, Under review.

[44] G.A. Holzapfel, Nonlinear Solid Mechanics: A Continuum Approach for Engineering, Wiley and Sons, 2000.

[45] M.E. Gurtin, Thermodynamics and stability, Arch. Ration. Mech. Anal. 59 (1975) 63–96.

[46] M. Šilhavý, The Mechanics and Thermodynamics of Continuous Media, Springer, Berlin, Heidelberg, 1997.

[47] M. Horák, A.J. Gil, R. Ortigosa, M. Kružík, A polyconvex transversely-isotropic invariant-based formulation for electro-mechanics: stability, minimisers and computational implementation, Comput. Methods Appl. Mech. Eng. 403 (2023) 115695.

[48] I.A. Karim, C.H. Lee, A.J. Gil, J. Bonet, A two-step Taylor Galerkin formulation for fast dynamics, Eng. Comput. 31 (2014) 366–387.

[49] C.H. Lee, A.J. Gil, J. Bonet, Development of a cell centred upwind finite volume algorithm for a new conservation law formulation in structural dynamics, Comput. Struct. 118 (2013) 13–38.

[50] C.H. Lee, A.J. Gil, A. Ghavamian, J. Bonet, A Total Lagrangian upwind Smooth Particle Hydrodynamics algorithm for large strain explicit solid dynamics, Comput. Methods Appl. Mech. Eng. 344 (2019) 209–250.

[51] C.H. Lee, A.J. Gil, J. Bonet, Development of a stabilised Petrov-Galerkin formulation for conservation laws in Lagrangian fast solid dynamics, Comput. Methods Appl. Mech. Eng. 268 (2014) 40–64.

[52] C.H. Lee, A.J. Gil, G. Greto, S. Kulasegaram, J. Bonet, A new Jameson-Schmidt-Turkel Smooth Particle Hdrodynamics algorithm for large strain explicit fast dynamics, Comput. Methods Appl. Mech. Eng. 311 (2016) 71–111.

[53] C.H. Lee, A.J. Gil, O.I. Hassan, J. Bonet, S. Kulasegaram, A variationally consistent Streamline Upwind Petrov Galerkin Smooth Particle Hydrodynamics algorithm for large strain solid dynamics, Comput. Methods Appl. Mech. Eng. 318 (2017) 514–536.

[54] J. Haider, C.H. Lee, A.J. Gil, J. Bonet, A first order hyperbolic framework for large strain computational solid dynamics: an upwind cell centred total Lagrangian scheme, Int. J. Numer. Methods Eng. 109 (2017) 407–456.

[55] M. Aguirre, A.J. Gil, J. Bonet, C.H. Lee, An upwind vertex centred finite volume solver for Lagrangian solid dynamics, J. Comput. Phys. 300 (2015) 387–422.
[56] A.J. Gil, C.H. Lee, J. Bonet, M. Aguirre, A stabilised Petrov-Galerkin formulation for linear tetrahedral elements in compressible, nearly incompressible and truly incompressible fast dynamics, Comput. Methods Appl. Mech. Eng. 276 (2014) 659–690.
[57] A. Ghavamian, C.H. Lee, A.J. Gil, J. Bonet, T. Heuzé, L. Stainier, An entropy-stable Smooth Particle Hydrodynamics algorithm for large strain thermo-elasticity, Comput. Methods Appl. Mech. Eng. 379 (2021) 113736.
[58] J. Haider, C.H. Lee, A.J. Gil, A. Huerta, J. Bonet, An upwind cell centred total Lagrangian finite volume algorithm for nearly incompressible explicit fast solid dynamic applications, Comput. Methods Appl. Mech. Eng. 340 (2018) 684–727.
[59] C.J. Runcie, C.H. Lee, J. Haider, A.J. Gil, J. Bonet, An acoustic Riemann solver for large strain computational contact dynamics, Int. J. Numer. Methods Eng. 123 (2022) 5700–5748.
[60] K.W.Q. Low, C.H. Lee, A.J. Gil, J. Haider, J. Bonet, A parameter-free Total Lagrangian Smooth Particle Hydronamics algorithm applied to problems with free surfaces, Comput. Part. Mech. 8 (2021) 859–892.
[61] E.A. de Souza Neto, D. Peri, D.R.J. Owen, Computational Methods for Plasticity, John Wiley and Sons, Ltd, Chichester, UK, 2008, Publication Title: Computational Methods for Plasticity.
[62] M. Aguirre, A.J. Gil, J. Bonet, A.A. Carreño, A vertex centred finite volume Jameson-Schmidt-Turkel (JST) algorithm for a mixed conservation formulation in solid dynamics, J. Comput. Phys. 259 (2014) 672–699.
[63] A.J. Gil, Z. Zhang, O. Hassan, K. Morgan, Parallel multigrid detached eddy simulation algorithm for three-dimensional unsteady incompressible flows on unstructured grids, J. Aerosp. Eng. 19 (2006) 271–280.
[64] T.J.R. Hughes, W.K. Liu, A. Brooks, Review of finite element analysis of incompressible viscous flows by the penalty function formulation, J. Comput. Phys. 30 (1979) 1–60.
[65] T.J.R. Hughes, G. Scovazzi, L.P. Franca, in: E. Stein, R. de Borst, T.J.R. Hughes (Eds.), Encyclopedia of Computational Mechanics, John Wiley and Sons, 2004.
[66] T.J.R. Hughes, G. Scovazzi, T.E. Tezduyar, Stabilized methods for compressible flows, J. Sci. Comput. 43 (2010) 343–368.
[67] G. Scovazzi, B. Carnes, X. Zeng, S. Rossi, A simple, stable, and accurate linear tetrahedral finite element for transient, nearly and fully incompressible solid dynamics: a dynamic variational multiscale approach, Int. J. Numer. Methods Eng. 106 (2016) 799–839.
[68] S. Rossi, N. Abboud, G. Scovazzi, Implicit finite incompressible elastodynamics with linear finite elements: a stabilized method in rate form, Comput. Methods Appl. Mech. Eng. 311 (2016) 208–249.
[69] J. Bonet, H. Marriott, O. Hassan, An averaged nodal deformation gradient linear tetrahedral element for large strain explicit dynamic applications, Commun. Numer. Methods Eng. 17 (2001) 551–561.
[70] J. Bonet, H. Marriott, O. Hassan, Stability and comparison of different linear tetrahedral formulations for nearly incompressible explicit dynamic applications, Int. J. Numer. Methods Eng. 50 (2001) 119–133.
[71] T. Belytschko, W.K. Liu, B. Moran, Nonlinear Finite Elements for Continua and Structures, John Wiley and Sons, 2000.
[72] E.F. Toro, Riemann Solvers and Numerical Methods for Fluid Dynamics: A Practical Introduction, second edition, Springer-Verlag, 2006.
[73] R. Abedi, R.B. Haber, Riemann solutions and spacetime discontinuous Galerkin method for linear elastodynamic contact, Comput. Methods Appl. Mech. Eng. 270 (2014) 150–177.
[74] R.L. Leveque, Finite Volume Methods for Hyperbolic Problems, Cambridge University Press, 2002.
[75] R. Courant, K. Friedrichs, H. Lewy, On the partial difference equations of mathematical physics, Math. Annal. 100 (1928) 32–74.
[76] T. Heuze, L. Stainier, A variational formulation of thermomechanical constitutive update for hyperbolic conservation laws, Comput. Methods Appl. Mech. Eng. 394 (2022) 114893.
[77] P.-O. Persson, J. Bonet, J. Peraire, Discontinuous Galerkin solution of the Navier-Stokes equations on deformable domain, Comput. Methods Appl. Mech. Eng. 198 (2009) 1585–1595.
[78] R. Sevilla, A.J. Gil, M. Weberstadt, A high-order stabilised ALE finite element formulation for the Euler equations on deformable domains, Comput. Methods Appl. Mech. Eng. (2017) 89–102.